



TECHNISCHE  
UNIVERSITÄT  
WIEN  
Vienna University of Technology



**Dissertation**

# **State parameter based modelling of stress-strain curves in aluminium alloys**

carried out for the purpose of obtaining the degree of Doctor technicae (Dr. techn.), submitted at TU Wien, Faculty of Mechanical and Industrial Engineering, by

**Dipl.-Ing. Johannes Franz KREYCA**

Mat.Nr.: 0627834

under the supervision of

Univ.Prof. Dipl.-Ing. Dr. Ernst Kozeschnik

Institute of Material Science and Technology

reviewed by

Univ. Prof. Dr. Prof. E.h. mult. Rudolf  
Kawalla

Technische Universität Bergakademie  
Freiberg

Ass. Prof. Dr. Stefan Pogatscher

Montanuniversität Leoben

# Kurzfassung

In dieser Arbeit wird ein neues Modell zur Simulation von Spannungs-Dehnungs Diagrammen in Abhängigkeit von Temperatur, Dehnrates und Materialzustand in Aluminiumlegierungen beschrieben. Der Materialzustand wird dabei unter Zuhilfenahme der Simulationssoftware MatCalc in Abhängigkeit der thermo-mechanischen Vorgeschichte modelliert. Die Simulation des dehnungsabhängigen Spannungs-Anteils beruht auf einer Entwicklung der durchschnittlichen Versetzungsdichte als Funktion von Temperatur und Dehnrates. Zur Modellierung des dehnungsunabhängigen Spannungs-Anteils wird zuerst die Streckgrenze bei 0K berechnet wobei unterschiedliche Verfestigungsmechanismen wie z.B. Mischkristall-, Ausscheidungs- oder Korngrenzenverfestigung berücksichtigt werden können. Ausgehend von der Streckgrenze bei 0K wird das Materialverhalten bei gegebener Temperatur und Dehnrates mithilfe eines physikalischen Modells zur thermischen Aktivierung beschrieben. Das beschriebene Modell wird mit experimentellen Daten, die zum Teil im Zuge dieser Arbeit entstanden sind verglichen und kalibriert. Im Zuge dieser Arbeit sind auch mehrere Fachartikel in anerkannten wissenschaftlichen Journalen veröffentlicht worden.

I confirm, that going to press of this thesis needs the confirmation of the examination committee.

*Affidavit*

I declare in lieu of oath, that I wrote this thesis and performed the associated research myself, using only literature cited in this volume. If text passages from sources are used literally, they are marked as such.

I confirm that this work is original and has not been submitted elsewhere for any examination, nor is it currently under consideration for a thesis elsewhere.

Vienna, 12, 2017

Signature

# List of Publications

The subsequent list contains references of journal papers, conference proceedings and presentations authored or co-authored by the present author during his time as a PhD student. The work covers investigations on state-parameter based modelling, thermal activation and experimental determination of stress-strain curves and deformation-induced microstructure.

## Journal Papers

Kreyca, J., Kozeschnik, E., 2017a. Temperature-dependent strain hardening, precipitation and deformation-induced microstructure evolution in AA 6061. *Mater. Sci. Eng. A* 708, 411–418.

Kreyca, J., Kozeschnik, E., 2017. Analysis of the Temperature and Strain-Rate Dependences of Strain hardening, *Metall. Mater. Trans. A*, in print.

Kreyca, J., Kozeschnik, E., 2017. State parameter-based constitutive modelling of stress strain curves in Al-Mg solid solutions. *Int. J. Plast.*, submitted.

## Conference Proceedings (presenting author)

### 2015

MEFORM, Freiberg

Kreyca, J., Falahati, A., Kozeschnik, E., 2015. Microstructure and Flow Stress Modelling During Plastic Deformation of an Aluminum Alloy Type A6061, in: *Materials Today: Proceedings*. Elsevier Ltd, pp. S102–S112.

ESAFORM, Graz

Kreyca, J., Falahati, A., Kozeschnik, E., 2015. Modelling Microstructure Evolution in Polycrystalline Aluminium – Comparison between One- and Multi-Parameter Models with Experiment. *Key Eng. Mater.* 651–653, 587–591.

Beyer, U., Neubauer, I., Kreyca, J., Kozeschnik, E., 2015. Virtual Joining Factory - Integration of microstructure evolution in the manufacturing process chain simulation. *Key Eng. Mater.* 1325–1330

Simufact Roundtable, Marburg

Kreyca, J., Kozeschnik, E., 2015. Vorhersage von Fließkurven für Aluminium-Legierungen - Erwartung und Wirklichkeit, in: *Simufact 16. Roundtable*. pp. 1–5.

MPPE, Leoben

Kreyca, J., Falahati, A., Kozeschnik, E., 2016. Experimental characterisation and modelling of deformation-induced microstructure in an A6061 aluminium alloy. *IOP Conf. Ser. Mater. Sci. Eng.* doi:doi:10.1088/1757-899X/119/1/012017

## 2016

THERMEC, Graz

Kreyca, J., Falahati, A., Kozeschnik, E., 2017. Modelling Yield Strength in an A6061 Aluminium Alloy. Mater. Sci. Forum 879, 1014–1018.  
doi:doi:10.4028/www.scientific.net/MSF.879.1014

## 2017

ICTP, Cambridge

Kreyca, J., Kozeschnik, E., 2017. Dissolution of hardening phases during deformation in an A6061 Aluminium alloy. Procedia Eng.

MEFORM, Freiberg

Kreyca, J., Kozeschnik, E., 2017. Flow stress modelling and microstructure development during deformation of metallic materials. Mater. Sci. Forum 892, 44–49.

## Presentations

Plasticity 2015

Kreyca, J., Kozeschnik, E., 2015. Modeling the stress-strain curve of poly-crystalline metals using a state parameter-based approach.

Thermec 2016, Graz

Kozeschnik, E., Kreyca, J., Buken, H., Svoboda, J., Riedel, H., Fischer, F.D., 2016. Temperature and strain rate effects on strengthening of metallic materials.

62. Metallkunde-Kolloquium 2016, Lech am Arlberg

Kreyca, J., Falahati, A., Kozeschnik, E., 2016. Strain hardening of a 6000 series aluminium alloy.

63. Metallkunde-Kolloquium 2017, Lech am Arlberg

Kreyca, J., Falahati, A., Kozeschnik, E., 2017. Thermally activated strain hardening in Al-alloy.

## **Acknowledgement**

I am very grateful to Prof. Ernst Kozeschnik for enabling and supervising the present PhD thesis as well as for numerous interesting discussions while enjoying some beers together. The completion of this work was also encouraged by fruitful discussions with my colleagues and undergraduate students that I was privileged to supervise during my period at the institute.

Special thanks go to my girlfriend Martina and my family and friends for supporting me during my time as a PhD student.

## **Abstract**

A novel and comprehensive model addressing the stress strain response under uniaxial loading over a wide range of temperatures, strain rates and material states is developed and introduced. Temperature and strain rate dependence of the yield stress are derived on the basis of an idealized material concept of a box-shaped and periodical dislocation-obstacle interaction profile. The model for strain hardening is based on an extended Kocks-Mecking evolution equation for the average dislocation density and discussed in terms of the temperature- and strain rate-dependence of the initial strain hardening rate and the saturation stress for stage-III hardening. The model covers both, low temperature deformation due to dynamic recovery and vacancy-assisted climb leading to static recovery at elevated temperatures. The model is finally validated on experimental data for solid solutions and artificially aged aluminium alloys.

# Table of contents

1	Introduction .....	1
2	Objectives.....	3
3	State of the Art.....	4
3.1	Definition of stress and strain .....	4
3.2	Stages of deformation .....	5
3.2.1	Stages I and II.....	5
3.2.2	Stage III .....	6
3.2.3	Stages IV and V .....	8
3.3	Temperature and strain rate dependence of stress strain curves .....	10
3.3.1	Deformation mechanisms .....	10
3.3.2	Low temperature plasticity .....	12
3.3.3	High temperature plasticity .....	13
3.4	Deformation-induced microstructure evolution .....	14
3.4.1	Microstructural observation .....	14
3.4.2	Scaling laws .....	16
3.5	Modelling of stress strain curves.....	17
3.5.1	Constitutive models .....	18
3.5.2	Voce hardening law .....	19
3.5.3	State parameter-based models.....	20
4	Model development.....	23

4.1	Initial yield stress $\sigma_0$ .....	23
4.1.1	Material state and mechanical threshold .....	23
4.1.2	The thermal activation framework .....	25
4.2	Plastic stress $\sigma_p$ .....	30
4.2.1	Saturation stress.....	32
4.2.2	Initial strain hardening rate.....	34
4.2.3	Thermal activation of the ABC model .....	35
4.2.4	Stage IV extension for the ABC model .....	36
5	Experimental.....	37
5.1	Material and sample preparation.....	37
5.2	Thermo-mechanical treatment .....	38
5.3	Data preparation .....	39
6	Simulation .....	41
6.1	AA 6061.....	41
6.1.1	Precipitation sequence.....	41
6.1.2	Thermal stability of $\beta''$ .....	42
6.1.3	Stage IV.....	43
6.2	Solid solutions.....	44
7	Results.....	48
7.1	AA6061.....	48
7.1.1	Experimental data .....	48
7.1.2	Simulation.....	53
7.2	Solid solutions.....	57
8	Discussion.....	63
9	Summary .....	68
10	References .....	69

Appendix.....	77
Key Publications.....	77
Paper 1 .....	78
Paper 2 .....	98
Paper 3 .....	104
Derivation of the dislocation storage and dynamic recovery terms.....	133
Curriculum Vitae .....	135

# 1 Introduction

Aluminium alloys are known for their good specific strength, weldability and corrosion resistance. From the first discovery of precipitation hardening in aluminium alloys in 1906 (Duparc, 2005), the unique combination of mechanical properties and light weight has since led to an ever increasing interest in aluminium alloys especially in fields where the reduction of weight is of importance. The outstanding mechanical properties of Al-X alloys mainly stem from a high potential for solid solution hardening, e.g. +172MPa with Mg (Uesugi and Higashi, 2013), and an even higher potential for precipitation strengthening, e.g., in 2xxx, 6xxx and 7xxx alloys, where a strength of 600-700MPa (Fribourg et al., 2011) can be reached while maintaining reasonable ductility. Unfortunately, forming processes in Al solid solutions are complicated by the effect of dynamic strain ageing (DSA) in certain temperature and strain rate regions, which can lead to negative strain rate sensitivity, serrated flow and decreased ductility. This combination of high industrial relevance and complex underlying physical processes has fostered great scientific interest and has led to numerous publications on this topic. Creep of aluminium alloy, e.g. was investigated by (Li et al., 1997). (Hu et al., 2016) presented a crystal plasticity extended models for the tensile behaviour of aluminium alloys. The variation of strain rate sensitivity of an aluminium alloy in a wide strain rate range was studied by (Yan et al., 2016). Cyclic plasticity and the Bauschinger effect were subject to investigations by (Yoshida and Uemori, 2002). Dislocation density based models on strain hardening were recently introduced by (Csanadi et al., 2014), (Silbermann et al., 2014) and (Bertin et al., 2013). The formability of AA5083 and AA6061 was investigated through experimentation by (Liu et al., 2010). High-velocity impact failure of 6061-T6 aluminum was investigated by (Ahad et al., 2014) and shock wave propagation in Al single and polycrystals by (Lloyd et al., 2014). Damage models were subject to the work of (Mengoni and Ponthot, 2015) and (Tutyshkin et al., 2014). Yield surface evolution in AA6061 and annealed 1100 Al

was presented by (Khan et al., 2009), (Khan et al., 2010a), (Khan et al., 2010b) and (Pandey et al., 2013). The anisotropic behaviour in AA 2090-T3 aluminium alloy was studied by (Safaei et al., 2014).

Some of these applications, e.g., finite element simulations, require material properties in the form of flow curves as input data, where even small variations of the input data can cause significant deviations in the resulting simulation (Umbrello et al., 2007). Traditionally such data is obtained through experimentation, which is expensive and time-consuming. A reduction of experimental cost by combining experiment with the simulation of temperature, strain rate and material state dependent stress-strain curve data is thus highly desirable. With the development of specialized simulation software, e.g., the thermo-kinetic software package MatCalc (Kozeschnik, 2017), it is possible nowadays, to predict the material state, i.e., atoms in solid solution, grain size, precipitation size, distribution, growth and coarsening in multi-component, multi-phase and multi particle systems (Svoboda et al., 2004),(Kozeschnik et al., 2004a), (Kozeschnik et al., 2004b). Using these tools enables the development of physically based models on temperature, strain rate and material state dependent stress strain curves and closes the gap between finite element and thermo-kinetic simulation.

## 2 Objectives

The aim of this work is the development of a model on the temperature, strain rate and material state-dependent flow curve prediction based on results from MatCalc thermo-kinetic simulation on *precipitation state*, *solute content* and *grain size* for either basic studies of physical mechanisms occurring during thermo-mechanical treatment or for using these curves as input for finite element simulation. Consequently, one requirement is the accurate reproduction of experimental stress-strain curves from low to high temperatures in a continuous and steady manner. Additionally, the model should deliver a realistic dislocation density evolution as function of temperature, strain rate and material state, as this is a major input parameter for the modelling of precipitation kinetics (heterogeneous nucleation sites) as well as of recrystallization and recovery.

### 3 State of the Art

This chapter is initiated with a definition of stress and strain, which is followed by a description of the macroscopic shape and general appearance of stress strain curves using the concept of deformation stages. Subsequently, deformation mechanisms are discussed in the light of thermal activation. The evolution of microstructural state parameters during plastic deformation and the most important scaling laws relating microstructural state parameters and stress are described afterwards. Following this, constitutive and state parameter based models for stress-strain curves are reviewed.

#### 3.1 Definition of stress and strain

In the present work, stress,  $\sigma$ , and strain,  $\varepsilon$ , are defined as *true stress* and *true strain* according to

$$\sigma = F/A \text{ and} \tag{1}$$

$$\varepsilon = \ln(h/h_0), \tag{2}$$

where  $F$  is the applied force,  $h_0$  is the initial height/length of the specimen, and  $h$  the height/length measured during deformation.  $A$  is the actual cross-section that is either directly measured or derived from  $h$  and the assumption of constant volume and no barrelling, according to  $A = A_0 h_0 / h$ . In polycrystalline materials the Taylor factor,  $M$ , is commonly used to relate the true stress with the critical resolved shear stress,  $\tau$ , acting on a slip plane according to

$$\sigma = M \cdot \tau. \tag{3}$$

The Taylor factor  $M$  is an average orientation factor, which depends on texture and the crystallographic nature of the material (Mecking et al., 1996). It has a numerical value of 3.06 for fcc (Kocks, 1970) and was first derived by (Taylor, 1938), see also (Canova et al., 1984) and (Hansen and Huang, 1998). The macroscopic strain,  $\varepsilon$ , is related to the resolved strain,  $\gamma$ , acting on a slip plane via  $\varepsilon = \gamma/M$ . Consequently also the strain rate,  $\dot{\varepsilon} = \dot{\gamma}/M$ , is related to

the resolved strain rate,  $\dot{\gamma}$ , through the Taylor factor. A very useful quantity is the strain hardening rate that is defined as

$$\theta = \frac{d\sigma}{d\varepsilon}. \quad (4)$$

The resolved strain hardening rate,  $\Theta$ , is given as  $\theta = \Theta \cdot M^2$ . It should be emphasised here, that the definition of strain,  $\varepsilon$ , according to Eq. (2) requires information about the ‘undeformed’ sample dimensions in the form of the initial height/length  $h_0$ , which cannot be measured a posteriori, when the sample is already deformed. The strain hardening rate,  $\theta$ , on the contrary, can be measured directly at any instant, is characteristic for a specific material state and is thus – together with  $\sigma$  – to be preferred as state parameter over  $\varepsilon$  in physical modelling. This work considers both  $\sigma$  vs.  $\varepsilon$  and  $\theta$  vs.  $\sigma$  relations.

## 3.2 Stages of deformation

According to (Diehl, 1956) and (Diehl et al., 1955) a plot of stress over strain can be divided in five well separated stages. These stages are reviewed in the following subsections.

### 3.2.1 Stages I and II

Stage I occurs in single crystals and is often referred to as ‘easy glide’. It is characterized by a fairly low strain hardening rate of  $\theta_I = 2 \cdot 10^{-4} G$  (Nabarro et al., 1964), where  $G$  is the shear modulus. After a certain amount of strain, the strain hardening rate increases significantly indicating a transition to stage II. The point of transition between stages I and II is not well reproducible and depends on chemical purity, prior handling, surface conditions (Nabarro et al., 1964) and crystallographic orientation. The strain hardening rate in stage II,  $\theta_{II}$ , reaches levels of  $G/20$  (Estrin, 1996), is almost independent of temperature and strain-rate and only slightly dependent on single crystal orientation. However, as pointed out by (Reed, 1972), stage II is observed to be temperature dependent to a certain degree in pure Al. Stage II is the first stage to sometimes occur in polycrystalline material. Fig. 1 (a) shows a schematic representation of Stages I and II, (b) shows some experimental results on pure copper.

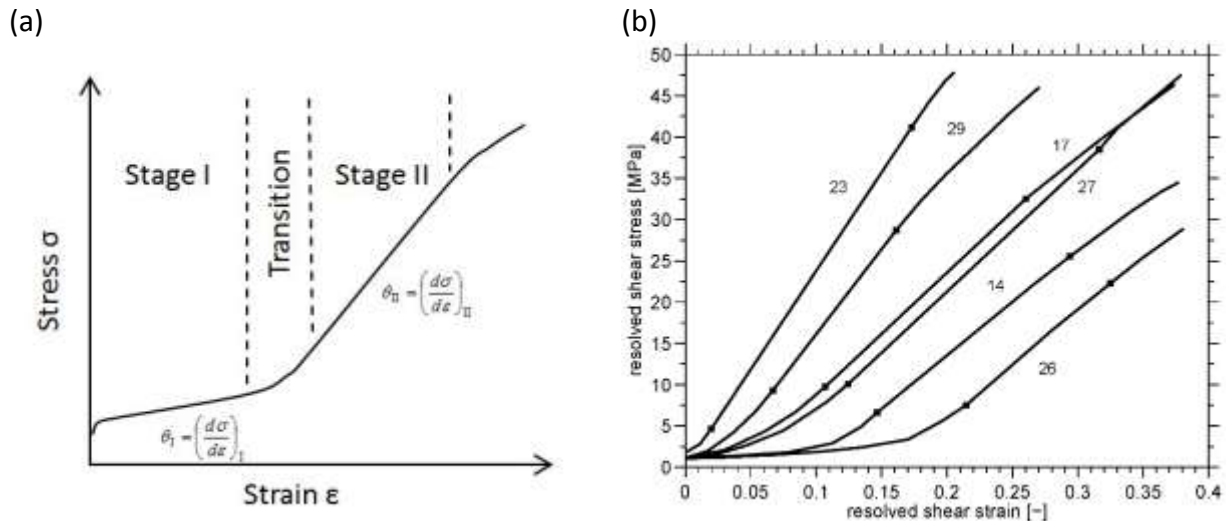
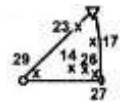


Fig. 1 (a) Schematic representation of stages I and II, adapted from (Diehl, 1956). (b) Shear stress versus shear strain curves for single crystals in 99.98% Cu with varying orientations. The markers show the beginning and end of Stage II adapted from (Kocks and Mecking, 2003) .



### 3.2.2 Stage III

Stage III occurs in succession to stage II. Stage III is the most important deformation stage during tensile testing and most constitutive relations aim at modelling the ‘parabolic nature’ of stage III behaviour. It is characterized by a decreasing strain hardening rate,  $\theta_{III}$ , with increasing stress and a strong dependence on temperature and strain rate. In stage III, the dominant mechanism of dislocation annihilation is dynamic recovery (Kocks, 1976), (Kocks and Mecking, 2003). For the annihilation process to occur, cross-slip of screw dislocations is essential. Constitutive and physical models dealing with stage III hardening are described in section 3.5. Fig. 2 shows stage III hardening for (a) polycrystalline aluminium and (b) copper at various temperatures and strain rates.

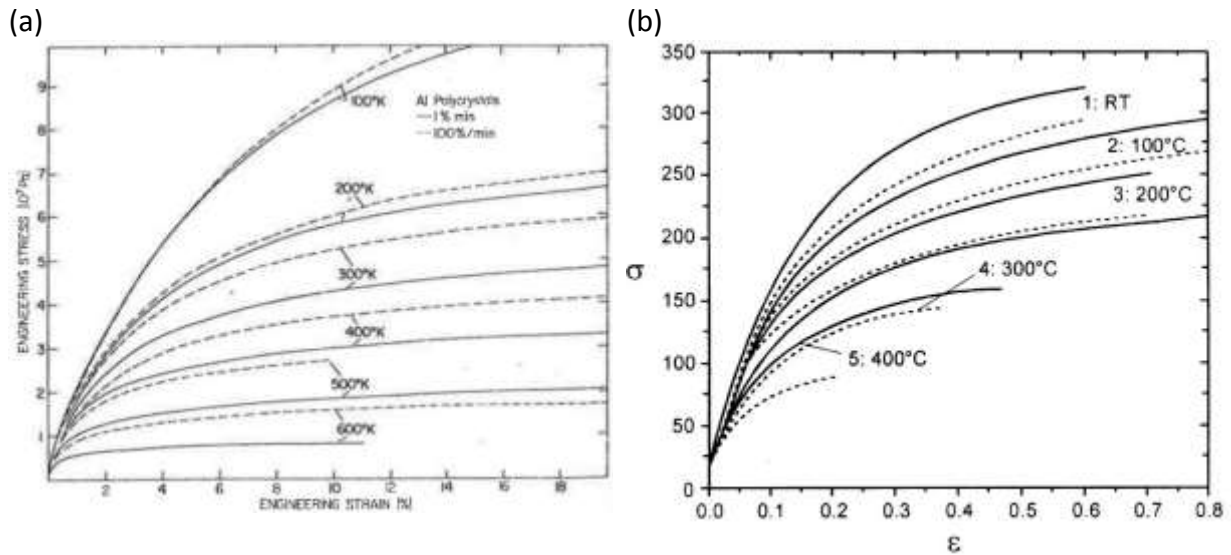


Fig. 2 Stage III hardening in (a) polycrystalline aluminium for different temperatures and strain rates (solid lines  $0.016 \text{ s}^{-1}$  and dashed line  $1.6 \text{ s}^{-1}$ ) adapted from (Kocks, 1976) and (b) polycrystalline copper for different temperatures and strain rates (solid lines  $10^{-4} \text{ s}^{-1}$  and dashed lines  $1 \text{ s}^{-1}$ ) adapted from (Kocks and Mecking, 2003).

For the characterization of stage III, it is often useful to plot the strain hardening rate  $\theta$ , as defined in section 3.1, as a function of stress  $\sigma$ . Fig. 3 shows a plot of  $\theta$  vs.  $\sigma$  (Kocks-plot) for the experimental data in Fig. 2 (b).

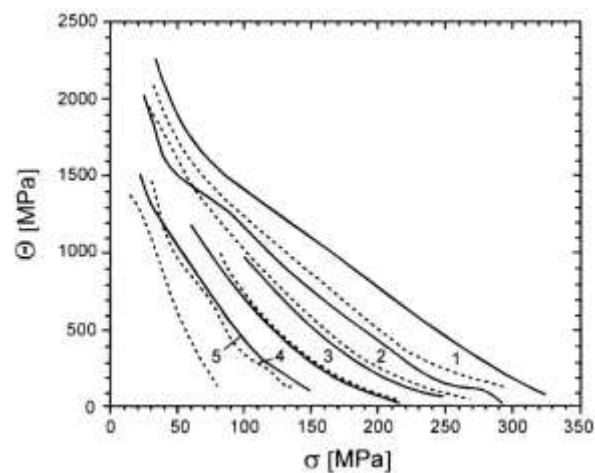


Fig. 3 Strain hardening rate as function of stress for the experimental data on polycrystalline copper in Fig. 2 (b) adapted from (Kocks and Mecking, 2003).

It is observed, that a plot of  $\theta$  vs.  $\sigma$  shows an almost linear relation between initial strain hardening rate and saturation stress in stage III. This relation is observed also in a series of other materials, e.g. for Al and stainless steel (Kocks, 1976), 7xxx series aluminium alloy

(Fribourg et al., 2011), Al-Cu (Deschamps et al., 1996), Al-Mg (Jobba et al., 2015) and is characteristic for stage III.

### 3.2.3 Stages IV and V

Stage III is followed by a stage (IV) of constant strain hardening rate in the order of magnitude of stage I, i.e.,  $\theta_{IV} = 2 \cdot 10^{-4} G$ . A comprehensive review on large strain deformation is given in (Gil Sevillano et al., 1981a) and (Rollet, 1988). Stage IV hardening is often not observed in tensile testing due to prior necking of the specimen and it is thus very often investigated using torsion experiments (Zehetbauer and Seumer, 1993), (Zehetbauer M., 1993), (Les et al., 1997) or compression testing (Asgari et al., 1997). Stage IV was first characterized by (Langford and Cohen, 1969), where large strains were attained by wire drawing and subsequent tensile testing. Most interestingly, this stage is almost insensitive to alloy composition (Kocks, 1985) and (Ryen et al., 2006b). Stage IV is sometimes followed by stress saturation (Zehetbauer and Seumer, 1993), (Zehetbauer M., 1993) that is then referred to as stage V. Several possible causes for the occurrence of stage IV have been discussed in literature (Mecking and Grinberg, 1979) and merged into modelling approaches (Galindo-Nava and Rivera-Díaz-Del-Castillo, 2012), (Pantleon, 2005) and (Prinz and Argon, 1984). Fig. 4 (a) shows experimental stress strain curves depicting stages III, IV and V in polycrystalline copper for different temperatures, (b) shows related Kocks-plots.

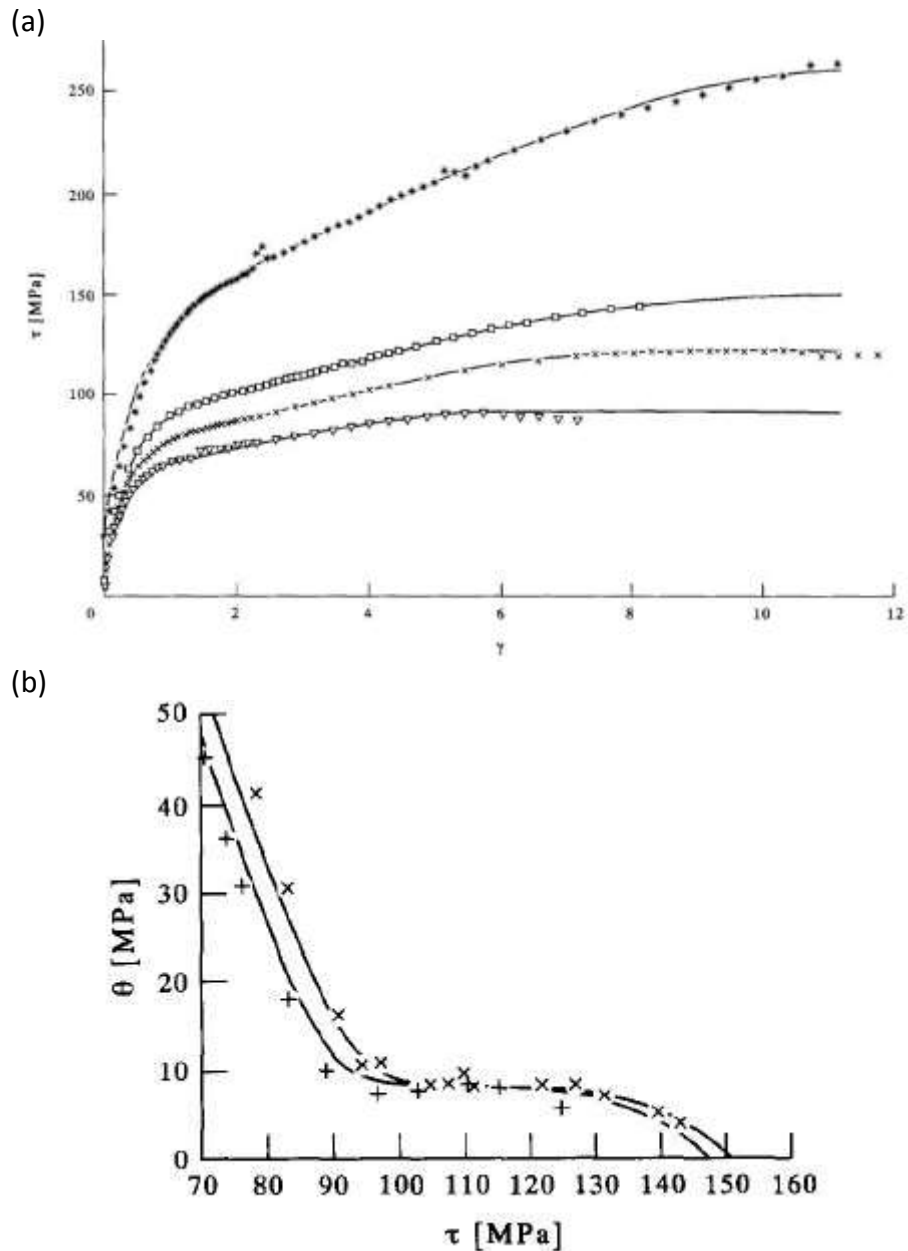


Fig. 4 (a) Shear stress vs. shear strain showing stages III, IV and V in polycrystalline copper for different temperatures (77K, 293K, 373K and 473K) and a strain rate of  $10^{-2} \text{ s}^{-1}$  derived by torsion testing. (b) Strain hardening rate vs. shear stress,  $T = 293\text{K}$ , strain rates  $\times 10^{-2} \text{ s}^{-1}$ ,  $+ 10^{-4} \text{ s}^{-1}$  adapted from (Zehetbauer M., 1993).

Fig. 5 summarizes the stages of deformation in polycrystalline materials in a schematic view, where (a) depicts a plot of stress vs. strain and (b) the corresponding Kocks-plot.

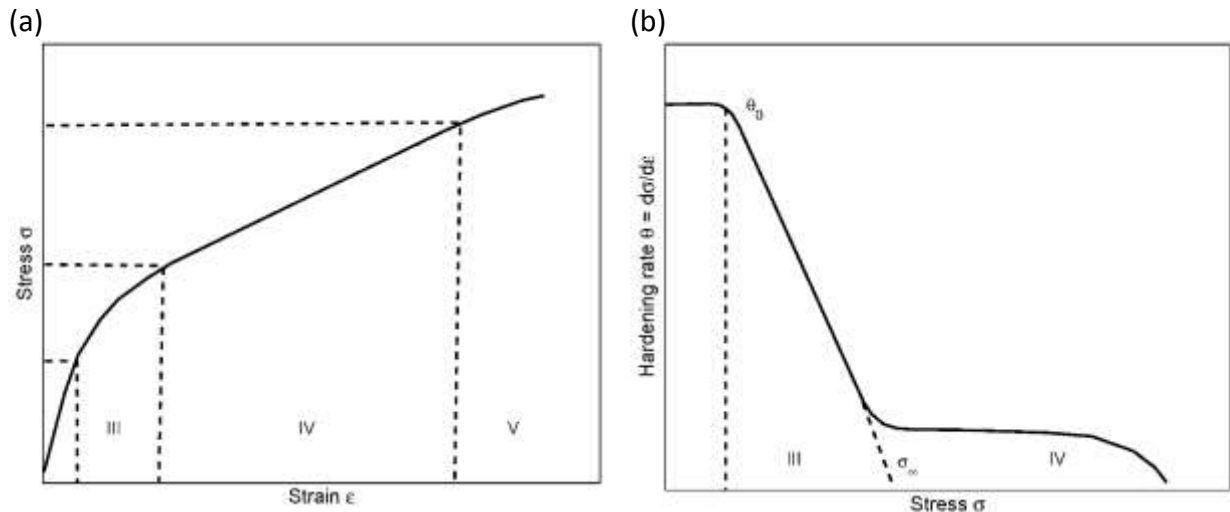


Fig. 5 Schematic representation of deformation stages in (a) a plot of stress vs. strain and (b) of hardening rate vs. stress (Kocks-plot).  $\theta_0$  is the strain hardening rate at stage III start and  $\sigma_\infty$  is the saturation stress.

Fig. 5 (b) also depicts the strain hardening rate at stage III start,  $\theta_0$ , and the theoretical saturation stress,  $\sigma_\infty$ , of stage III if no stage IV occurs. For the sake of simplicity,  $\theta_0$  is simply referred to as initial strain hardening rate and  $\sigma_\infty$  as saturation stress in the following.

### 3.3 Temperature and strain rate dependence of stress strain curves

It is common knowledge that the strength of a material is a function of temperature and strain rate. Intuitively, it is clear that materials are 'soft' at higher temperatures and are stronger when the rate of deformation is increased. In metallic materials this correlation has two major causes: (i) an increase in dislocation mobility with increasing temperature and (ii) the temperature dependence of the material state, e.g. the stability of a precipitation state. In this section the material state is assumed to be stable and any temperature and/or strain rate dependence of the stress strain curve is a consequence of a change in dislocation mobility or in deformation mechanism.

#### 3.3.1 Deformation mechanisms

Deformation by dislocation slip is the dominant deformation mechanism in face-centred cubic (fcc) metals with elevated stacking fault energy and in body-centred cubic (bcc) metals at intermediate and high temperatures. In hcp metals, mechanical twinning is of major

importance (Bolling and Richman, 1965a), (Bolling and Richman, 1965b), (Christian and Mahajan, 1995). The incremental strain carried by one dislocation and the direction of distortion within the crystal are indicated by the Burgers vector  $b$ . In addition to glide within a slip plane, dislocations can leave their glide plane by cross-slip or – at elevated temperature – by vacancy-assisted climb. Both mechanisms require thermal activation and it is believed that these mechanisms are the main reason for the temperature and strain rate dependence of stress strain curves. Cross-slip is the dominant annihilation mechanism at medium to high temperatures. It is restricted to screw dislocations and leads to dynamic recovery (Mott, 1952), (Schoeck and Seeger, 1955), (Seeger, 1957), (Jackson, 1985) and (Kocks and Mecking, 2003). Existing models for the mechanism of thermally activated cross-slip are analysed and compared in (Püschl, 2002). Dislocation climb requires diffusion of vacancies and is, thus, time-dependent. As a consequence, strain rate sensitivity is generally higher in regions where dislocation climb is dominant (Weertman, 1956), (Weertman, 1957), (McQueen and Ryan, 2002). At temperatures close to melting and low strain rates other diffusion-driven mechanisms (Nabarro, 1948), (Herring, 1950), (Lifshitz, 1963), (Coble, 1963), (Raj and Ashby, 1971), (Hirth, 1972), (Gifkins, 1976), (Shan, 2004) that do not involve dislocations and recrystallization (Luton and Sellars, 1969), (Doherty et al., 1997) become relevant. A good overview of deformation mechanisms as a function of temperature and strain rate are given in the form of deformation mechanism maps as introduced by (Frost and Ashby, 1982) where each deformation mechanism is described with an individual rate equation. Fig. 6 shows an exemplary deformation mechanism map for pure Al with a grain size of  $10\mu\text{m}$ .

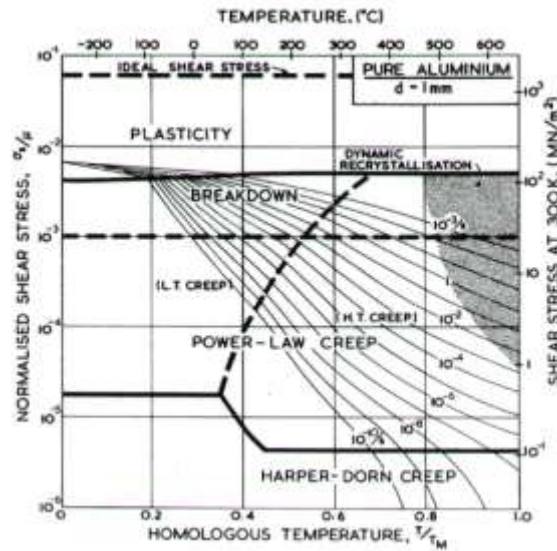


Fig. 6 Deformation mechanism map for pure Al with a grain size of 10µm reproduced from (Frost and Ashby, 1982).

In the following, two rate equations – one for low and intermediate temperatures and one for high temperatures – are discussed in more detail. Diffusional flow, mechanical twinning and recrystallization are out of the scope of this work and are not further investigated in the present work.

### 3.3.2 Low temperature plasticity

The mobility of a dislocation is fundamentally described by the Orowan equation (Orowan, 1940),

$$\dot{\epsilon} = \rho b v , \tag{5}$$

relating the macroscopic strain rate,  $\dot{\epsilon}$ , with the dislocation velocity,  $v$ , the Burgers vector and the average moving dislocation density,  $\rho$ . According to (Eyring, 1936), (Schoeck, 1965), (Argon, 1996) and (Frost and Ashby, 1982), the dislocation velocity for low and intermediate temperatures is expressed through an Arrhenius Ansatz in the form of

$$v = c \cdot \left( \exp\left(-\frac{\Delta G(\sigma)}{kT}\right) \right) \tag{6}$$

where  $\Delta G$  is the Gibbs energy,  $k$  is the Boltzmann constant and  $T$  is the temperature in Kelvin.  $\Delta G(\sigma)$  is often assumed to be

$$\Delta G = \Delta F \left( 1 - \left( \frac{\sigma}{\hat{\sigma}} \right)^q \right)^p, \quad (7)$$

where  $\hat{\sigma}$  is the yield stress at 0K also referred to as mechanical threshold (MTS) (Kocks et al., 1975),  $p$ ,  $q$  are material-dependent exponents and  $\Delta F$  is an activation energy. According to (Frost and Ashby, 1982),  $\Delta F$  can be written as  $\Delta F = aGb^3$ , where  $a$  is a factor between 0.2 and 2. A combination of Eqs. (5), (6) and (7) gives an expression for the temperature and strain rate-dependent yield stress, reading

$$\sigma = \hat{\sigma} \left( 1 - \left( \frac{kT}{\Delta F} \ln \left( \frac{\dot{\epsilon}_0}{\dot{\epsilon}} \right) \right)^{1/p} \right)^{1/q}. \quad (8)$$

Eq. (8) has been applied successfully in steel (Burgahn et al., 1996), (Schulze and Vohringer, 2000) and (Dahl and Krabiell, 1979) and in Al-alloys (Leyson and Curtin, 2016), (Leyson et al., 2010) and (Soare and Curtin, 2008). However, at a certain critical temperature,  $T_0$ , the delivered stress becomes zero and Eq. (8) loses its physical meaning.  $T_0$  is consequently an upper limit for the application of Eq. (8) and for  $T > T_0$  other, high temperature models must be applied.

### 3.3.3 High temperature plasticity

At elevated temperatures, the mobility of a dislocation is determined by diffusional processes, such as vacancy-assisted climb. According to (Hirth and Lothe, 1991), the velocity at which an edge dislocation climbs under a local normal stress can be expressed as

$$v = \frac{D_v \Omega}{bkT} \cdot \sigma, \quad (9)$$

where  $D_v$  is the lattice diffusion coefficient and  $\Omega$  the atomic or ionic volume. If, in addition to that, the mobile dislocation density is expressed by the Taylor equation, the rate equation in dependence of stress can be written as

$$\dot{\epsilon} = A_1 \frac{D_v Gb}{kT} \left( \frac{\sigma}{G} \right)^n, \quad (10)$$

where  $\Omega$  is approximated with  $b^3$ ,  $A_1$  is the Dorn-constant and  $n$  is an exponent in the range of 1-7. The case of  $n=3$  is often referred to as 'Natural creep law' as it follows directly from Eqs. (5) and (9). This natural creep law is obeyed by some materials, for example Al-Mg solid solutions (Kocks, 1998). In general, the Dorn constant,  $A_1$ , is heavily material dependent with

its values ranging from 1 to  $10^{15}$ . Equations in the form of Eq. (10) are referred to as power-laws due to their dependence on the exponent  $n$  and have been successfully applied and modified frequently. For further reading see (Sellars and Tegart, 1966), (Jonas, 1969), (Nix et al., 1985), (Li et al., 1997), (Nes, 1995), (El-Danaf et al., 2008a), (El-Danaf et al., 2008b), (Spigarelli et al., 2003), (Evans and Wilshire, 1996) and (Tello et al., 2010).

### **3.4 Deformation-induced microstructure evolution**

Besides macroscopic quantities, such as stress, strain, temperature and strain rate, also, microstructural quantities need to be considered for the understanding of plastic deformation. Experimental techniques for the determination of deformation-induced microstructure evolution, the concept of microstructural state parameters and the Taylor equation are described in this section.

#### **3.4.1 Microstructural observation**

A variety of experimental techniques has been developed for the direct or indirect observation of dislocations and deformation-induced microstructures. An early overview on experimental techniques is given in (Nabarro et al., 1964), where measurement of density, stored energy, electrical resistivity, surface effects, slip lines and surface markings, etch pits, magnetic saturation, nuclear magnetic resonance and X-ray diffraction are listed under the section of indirect measurement techniques. For direct observation, TEM (Malin and Hatherly, 1979), (Gil Sevillano et al., 1981a), (Hughes and Nix, 1989) and EBSD (Hurley and Humphreys, 2003) are used intensively nowadays. Fig. 7 (a) shows an exemplary TEM micrograph of a dislocation structure of a Fe-43at%Al single crystal, (b) shows an EBSD micrograph of deformation-induced microstructure in a single phase Al-0.1Mg alloy.

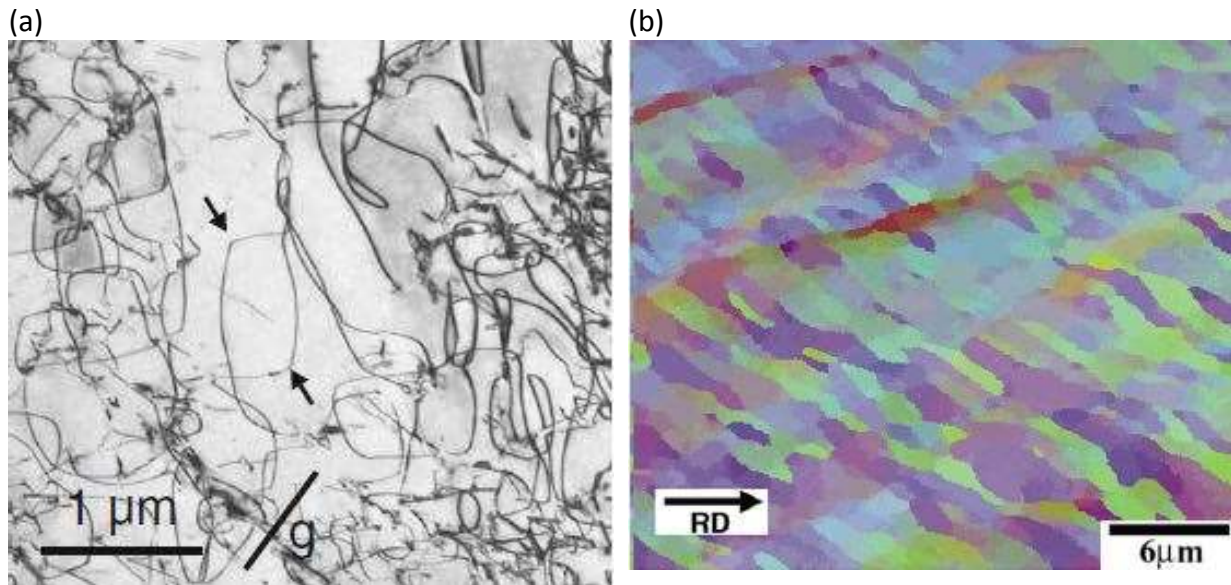


Fig. 7 (a) Dislocation entanglement in an Fe-43at%Al single crystal, adapted from (Messerschmidt et al., 2006) (b) EBSD relative Euler orientation map showing substructure after 50% rolling reduction in a single phase Al-0.1Mg alloy, adapted from (Hurley and Humphreys, 2003).

The deformation-induced microstructure is often observed to take the form of cells or subgrains that are well characterized by a mean subgrain diameter,  $\delta$ , and a mean misorientation angle,  $\varphi$ , between neighbouring subgrains (Furu et al., 1995). The number of immobilized dislocations is quantified with an average dislocation density,  $\rho$ , that has the unit of  $m/m^3$ . Average dislocation density, subgrain size and misorientation angle are referred to as microstructural state-parameters. In general, these state-parameters show specific tendencies as function of stress and strain that can be formulated in the form of 'scaling laws'. Fig. 8 shows a schematic representation of microstructural state parameters and stress as a function of strain.

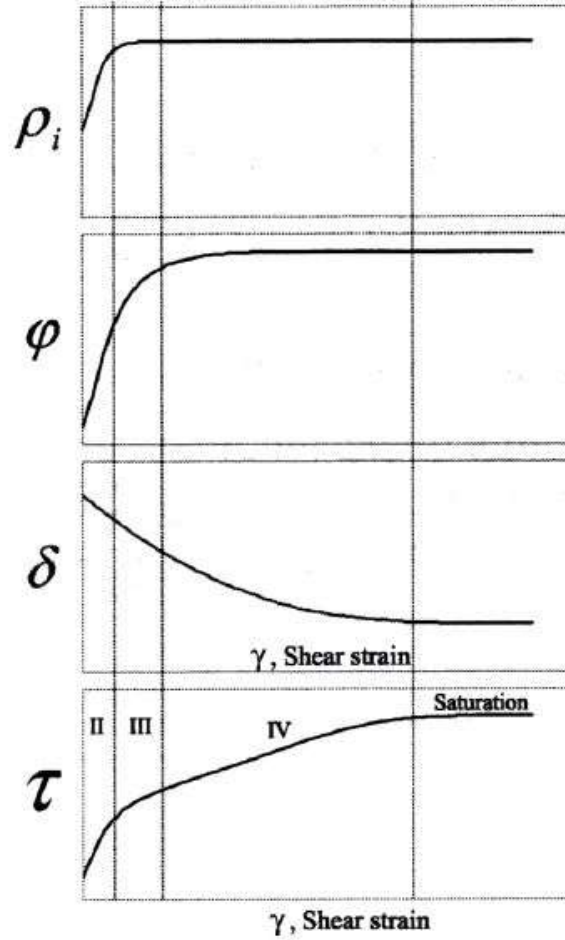


Fig. 8 Schematic representation of state parameters and shear stress evolution as a function of shear strain at room temperature, adapted from (Ryen, 2003).

### 3.4.2 Scaling laws

The microstructural state parameters and the macroscopic yield stress,  $\sigma$ , are related to each other through so called 'scaling laws' (Sauzay and Kubin, 2011). The most important of these scaling laws is the Taylor equation, which was first derived by (Taylor, 1934) and reads

$$\sigma = \alpha M G b \sqrt{\rho} = g_1 \sqrt{\rho} , \quad (11)$$

where  $g_1 = \alpha M G b$  and  $\alpha$  is a strengthening coefficient. The value of  $\alpha$  is determined by the geometrical arrangement of dislocations and is, thus, weakly dependent on strain (Mughrabi, 2016). Theoretical estimates for the strengthening coefficient were performed by (Saada, 1960), (Baird and Gale, 1965) and (Schoeck and Frydman, 1972) with  $\alpha \approx 0.3$  being the most precise estimate according to (Sauzay and Kubin, 2011).

The second scaling law is the principle of similitude (Gil Sevillano et al., 1981a), (Holt, 1970), (Staker and Holt, 1972), (Sauzay and Kubin, 2011) that relates the dislocation density to the subgrain diameter, reading

$$\sigma = KMGb/\delta, \quad (12)$$

where  $K$  is a constant, (Nes, 1994), (Nes, 1995), (Nes and Furu, 1995) and (Furu et al., 1995). Fig. 9 shows a compilation of results on dislocation density vs. resolved shear stress.

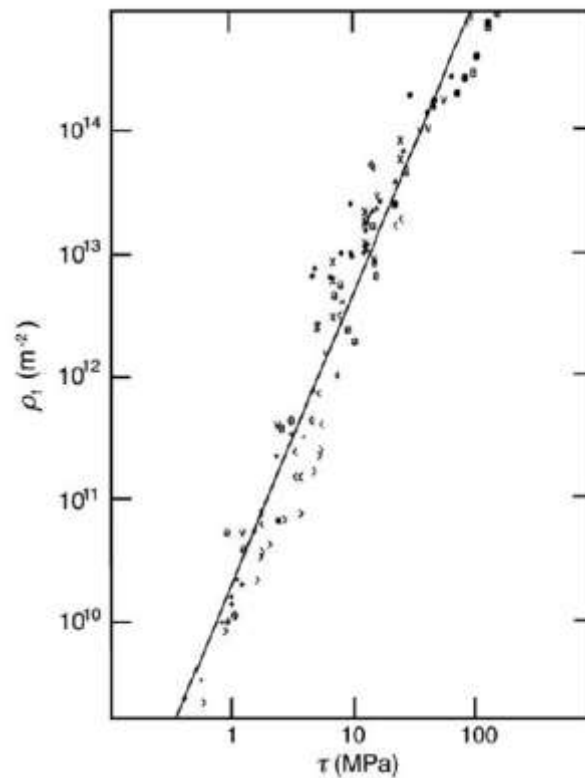


Fig. 9 Forest dislocation density vs. resolved flow stress. Reprinted from (Basinski and Basinski, 1979)

The 'scaling laws' are the basis for many state parameter-based models of stress strain curves as later introduced in section 3.5.3.

### 3.5 Modelling of stress strain curves

Models that have been found to appropriately reproduce experimentally derived stress-strain curves with the help of analytical functions are reported in this section. These models can be divided in two groups: (i) constitutive models, where stress is modelled 'only' as a

function of strain and (ii) state parameter-based models where the stress strain curve is derived from the evolution of one or more microstructural state parameter. An individual subsection is dedicated to the Voce hardening law (Voce, 1955), as this law is – on the one hand – a constitutive model and – on the other – the basis of most physical state parameter-based models.

### 3.5.1 Constitutive models

One of the earliest constitutive relation for the reproduction of stress strain curves was given by (Ludwik, 1909), reading

$$\sigma = \sigma_0 + k\varepsilon^n, \quad (13)$$

where  $n$  is the hardening exponent,  $k$  is a constant and  $\sigma_0 = \sigma_{\varepsilon=0}$  is the initial yield stress. Three parameters,  $\sigma_0$ ,  $k$  and  $n$  are required for parameterization of Eq. (13) that are easily derived from a double logarithmic plot of stress over strain. Applying  $d\sigma/d\varepsilon = \sigma$  as criterion for necking (Gensamer, 1938), it is easily shown that  $\varepsilon_m = n$ , where  $\varepsilon_m$  is the strain at maximum load. It was also shown by (Hollomon, 1945) that the initial yield stress,  $\sigma_0$ , is related to  $n$  in rather simple fashion. In constitutive models, it is common to express the temperature and strain rate-dependence of the stress as

$$\sigma(T, \dot{\varepsilon}, \varepsilon) = f(T, \dot{\varepsilon}) \cdot \sigma_{\text{ref}}(\varepsilon), \quad (14)$$

which comprises the product of a *strain*-dependent master-curve,  $\sigma_{\text{ref}}(\varepsilon)$ , according to Eq. (13) and a *temperature* and *strain rate*-dependent function,  $f(T, \dot{\varepsilon})$ . An example of this ‘product form’ is the Freiburger Ansatz (Schmidtchen and Spittel, 2011), where, for cold deformation,

$$\sigma = A \cdot e^{m_1 T} \cdot \varepsilon^{m_2} \cdot e^{m_4/\varepsilon} \cdot \dot{\varepsilon}^{m_3} \quad (15)$$

is applied and for hot deformation

$$\sigma = A \cdot e^{m_1 T} \cdot \varepsilon^{m_2} \cdot e^{m_4/\varepsilon} \cdot (1 + \varepsilon)^{m_5 T} \cdot e^{m_7 \varepsilon} \cdot \dot{\varepsilon}^{m_8 T} \quad (16)$$

Eqs. (15) and (16) have been parameterized for a large number of materials and are part of the data-base Landolt-Börnstein (Spittel and Spittel, 2009). Table 1 summarizes the functional dependence of a selection of constitutive models and indicates whether they are following the “product form” Eq. (14) or not.

Table 1. Overview of constitutive models

Source	Eqs.	Fitting parameter	Number of fitting parameters	Product form
(Ludwik, 1909), (Hollomon, 1945)	$\sigma = \sigma_0 + k\varepsilon^n$	$\sigma_0, k, n$	3	no
(Schmidtchen and Spittel, 2011)	$\sigma = A \cdot e^{m_1 T} \cdot \varepsilon^{m_2} \cdot e^{m_4/\varepsilon} \cdot \dot{\varepsilon}^{m_3}$	$A, m_1, m_2, m_4, m_3$	5	yes
(Schmidtchen and Spittel, 2011)	$\sigma = A \cdot e^{m_1 T} \cdot \varepsilon^{m_2} \cdot e^{m_4/\varepsilon} \cdot (1 + \varepsilon)^{m_5 T} \cdot e^{m_7 \varepsilon} \cdot \dot{\varepsilon}^{m_6 T}$	$A, m_1, m_2, m_4, m_5, m_7, m_6$	7	yes
(Johnson and Cook, 1983)	$\sigma = \left( (A + B\varepsilon^n) \left( 1 + C \ln(\dot{\varepsilon}/\dot{\varepsilon}_0) \right) \right) \left( 1 - \left[ \frac{T_m - T}{T_m - T_r} \right]^m \right)$	$A, B, n, C, \dot{\varepsilon}_0, T_r, m$	7	yes
(Zerilli and Armstrong, 1987)	$\sigma = c_0 + B_0 e^{-(\beta_0 - \beta_1 \ln \dot{\varepsilon})T} + k\varepsilon^n$	$c_0, B_0, \beta_0, \beta_1, k, n$	6	no
(Khan and Huang, 1992)	$\sigma = \left( \sigma_0 + E_\infty \varepsilon - a e^{-\alpha \varepsilon} \right) \left( 1 - \frac{\ln(\dot{\varepsilon})}{\ln(D_0)} \right)^{-n}$	$\sigma_0, E_\infty, a, \alpha, D_0, n$	6	yes
(Khan and Liang, 1999)	$\sigma = \left[ A + B \varepsilon^{n_0} \left( 1 - \frac{\ln \dot{\varepsilon}}{\ln D_p} \right)^{n_1} \right] \left[ \frac{\dot{\varepsilon}}{\dot{\varepsilon}^*} \right]^C \left[ \frac{T_m - T}{T_m - T_r} \right]^m$	$A, B, n_0, n_1, D_p, \dot{\varepsilon}^*, C, T_r, m$	9	yes

### 3.5.2 Voce hardening law

An alternative constitutive law was introduced by (Voce, 1955), reading

$$\sigma = \sigma_0 + \sigma_\infty \left( 1 - \exp\left(-\frac{\varepsilon}{\varepsilon_c}\right) \right), \quad (17)$$

where  $\varepsilon_c = \theta_0/\sigma_\infty$  is the critical strain,  $\theta_0$  is the initial strain hardening rate,  $\sigma_\infty$  the saturation stress and  $\sigma_0$  the initial yield stress, for a definition see section 3.2.3. This law describes an exponential relation between stress and strain and was originally introduced as a constitutive stress-strain curve model. In differential form, the Voce hardening law reads

$$\theta = \frac{d\sigma}{d\varepsilon} = \theta_0 \left( 1 - \frac{\sigma}{\sigma_\infty} \right) = h_1 - h_2 \sigma, \quad (18)$$

where  $h_1 = \theta_0$  and  $h_2 = \theta_0/\sigma_\infty$ . The Voce hardening law shows several important differences in comparison to power-laws, which are (i) stress saturation is reached at a certain level of

strain, (ii) the initial strain hardening rate,  $\theta_0$ , and the saturation stress,  $\sigma_\infty$ , as defined in section 3.2.3 are direct input parameters of the model and (iii) a linear relation between strain hardening rate,  $\theta$ , and stress,  $\sigma$ , is predicted by the model and is, thus, in good accordance with experimental observations for stage III, see section 3.2.2.

### 3.5.3 State parameter-based models

State parameter-based models (Kocks, 1976), (Estrin and Mecking, 1984), (Kubin and Estrin, 1990), (Estrin, 1996), (Nes, 1997), (Roters et al., 2000), (Marthinsen and Nes, 2001), (Barlat et al., 2002), (Tóth et al., 2002), (Beyerlein and Tome, 2007), (Austin and McDowell, 2011), (Fan and Yang, 2011), (Gao and Zhang, 2012), (Galindo-Nava et al., 2012), (Hansen et al., 2013), (Bertin et al., 2013), (Li et al., 2014), offer more physical insight than constitutive models and give access to the evolution of observable parameters, such as, e.g., the dislocation density. Such models are commonly founded on (i) the Taylor equation Eq. (11) and (ii) a differential equation for the average dislocation density evolution in the form

$$\frac{d\rho}{d\varepsilon} = \frac{d\rho^+}{d\varepsilon} - \frac{d\rho^-}{d\varepsilon}, \quad (19)$$

where the generation of dislocations due to plastic deformation is accounted for in the dislocation storage term,  $d\rho^+/d\varepsilon$ , whereas the annihilation of dislocations due to dynamic recovery is accounted for in the term  $d\rho^-/d\varepsilon = k_2\rho$ . The storage term is commonly related to the mean free path,  $L$ , of mobile dislocations (Barlat et al., 2002) through

$$\frac{d\rho^+}{d\varepsilon} = \frac{M}{bL}. \quad (20)$$

With the assumption that the mean free path is indirectly proportional to the square root of the dislocation density,

$$L = \frac{A}{\sqrt{\rho}}, \quad (21)$$

Eq (19) delivers the well-known Kocks-Mecking equation reading

$$\frac{d\rho}{d\varepsilon} = k_1\sqrt{\rho} - k_2\rho, \quad (22)$$

where  $k_1 = M/bA$  and  $A$  is a proportionality constant. The Kocks-Mecking (KM) model (Essmann and Mughrabi, 1979), (Kocks, 1976), (Mecking and Kocks, 1981), (Gil Sevillano et al., 1981b), (Estrin, 1996), (Kocks and Mecking, 2003) is one representative of a state

parameter-based model on plastic deformation and is the basis of the present model on strain hardening. With the Taylor equation,  $\sigma = g_1 \sqrt{\rho}$ , the KM model is alternatively written as

$$\frac{d\sigma}{d\varepsilon} = \frac{k_1 g_1}{2} - \frac{k_2}{2} \sigma, \quad (23)$$

which is an equivalent form of the Voce hardening law, Eq. (18). Consequently, the shape of the stress-strain curves modelled with the KM-model are – like in the case of the Voce hardening law – characterized by the initial strain hardening rate,  $\theta_0$ , the saturation stress,  $\sigma_\infty$ , and the critical strain,  $\varepsilon_c$ . The fundamental relations between  $k_1$ ,  $k_2$ ,  $h_1$ ,  $h_2$ ,  $\theta_0$  and  $\sigma_\infty$  read

$$\theta_0 = \frac{g_1 k_1}{2} = h_1, \quad (24)$$

$$\sigma_\infty = \frac{g_1 k_1}{k_2} = \frac{h_1}{h_2}. \quad (25)$$

Fig. 10 (a) shows a schematic view of a generic stress-strain curve calculated with Eq. (22) and Eq. (11), (b) shows the corresponding Kocks-plot.

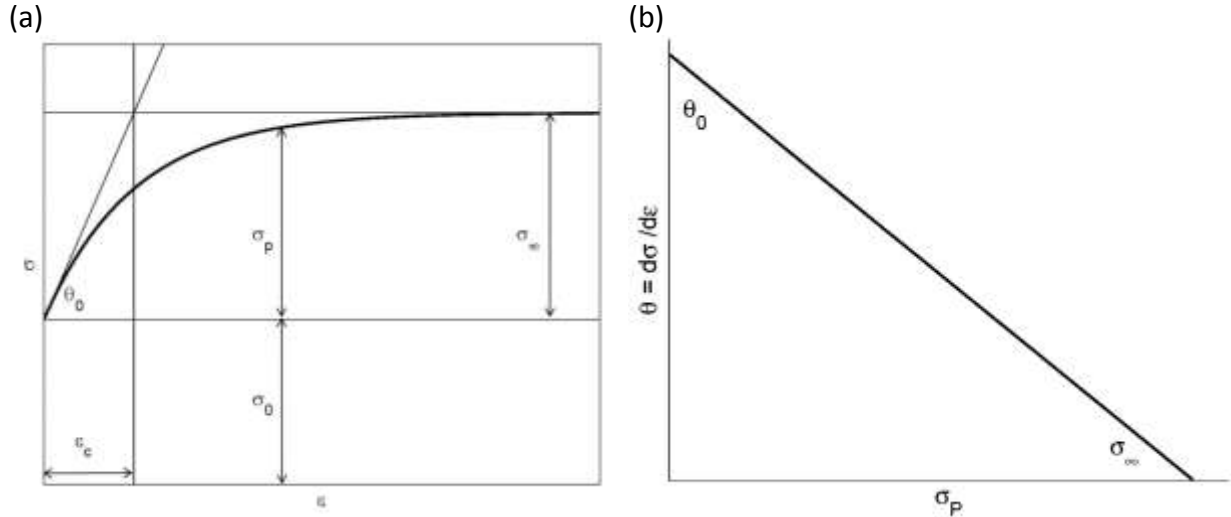


Fig. 10 (a) Schematic representation of a stress-strain curve according to the KM-model, Eq. (22) (b) corresponding Kocks-plot.

Eq. (22) does not contain any explicit temperature or strain rate dependence except if  $k_1$  or  $k_2$  are functions of temperature or strain rate. In most dislocation density-based models (Kocks, 1976), (Kubin and Estrin, 1990), (Estrin, 1996), (Galindo-Nava et al., 2012), (Nes, 1997), (Roters et al., 2000),  $k_1$  is assumed to be temperature-independent (except for the temperature-dependence of the shear modulus), whereas  $k_2$  is treated as a temperature and strain rate-dependent parameter. As a consequence, many state parameter-based models, e.g. (Roters et al., 2000), (Galindo-Nava et al., 2012), (Nes, 1997), (Kocks, 1976) predict an athermal initial strain hardening rate and only the saturation stress is a function of temperature and strain rate, see Eqs. (24) and (25). The analysis of the temperature and strain rate-dependence of strain hardening is then reduced to an analysis of the temperature and strain rate-dependence of the saturation stress and the expression for  $k_2$  is derived from Eq. (28) and the assumption of a constant  $\theta_0$ .

In the next section a modelling framework for temperature and strain rate-dependent stress-strain curve modelling is derived and analysed, where the framework is based on a state-parameter approach for an average dislocation density. It should be emphasized that multi-parameter models, such as the ones from (Barlat et al., 2002), (Kubin and Estrin, 1990), (Tóth et al., 2002), (Roters et al., 2000) and (Nes, 1997) are out of the scope of the present work and are not further investigated here.

## 4 Model development

In this chapter, a model for the temperature, strain rate and material state-dependent flow curve prediction is developed based on the background given in section 3. In the following analysis, the yield stress is represented by the sum of a strain-independent initial yield stress,  $\sigma_0$ , and a strain-dependent stress,  $\sigma_p$ , also referred to as the plastic stress, which can be modelled separately as

$$\sigma = \sigma_0 + \sigma_p. \quad (26)$$

The model for the initial yield stress,  $\sigma_0$ , is introduced first, based on the concepts of the material state-dependent mechanical threshold stress and a thermal activation framework. The thermal activation framework is based on a material concept of an idealized box-shaped and periodical dislocation-obstacle interaction profile. In a subsequent section, a dislocation density-based model for the calculation of the plastic stress,  $\sigma_p$ , is presented and analyzed, based on an extended KM-model. The explicit functional relations given in this section constitute a major result of the present work.

### 4.1 Initial yield stress $\sigma_0$

#### 4.1.1 Material state and mechanical threshold

For a certain alloy composition, the material state, e.g., distribution of precipitates, atoms in solid solution, grain size, etc. follows from the thermo-mechanical history of the material. Fig. 11 shows a typical heat-treatment scheme with three steps of solidification, homogenization and precipitation.

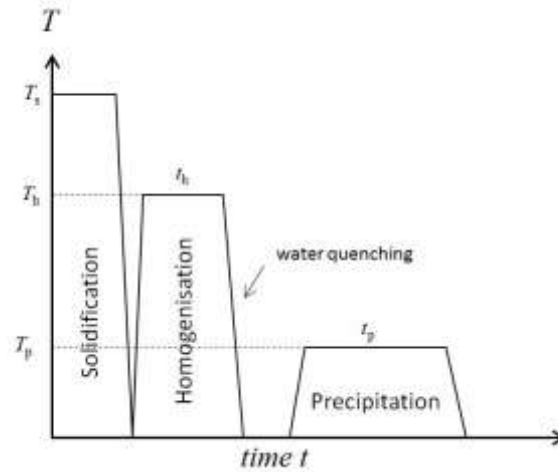


Fig. 11 Schematic three-step heat treatment with solidus temperature  $T_s$ , homogenisation temperature  $T_h$  and  $T_p$  indicating the temperature for precipitation heat treatment.

The state parameter evolution during thermo-mechanical treatment can be calculated, e.g, with the help of the thermo-kinetic software package MatCalc [<http://matcalc.at>]. An example of such a material state calculation is given in the results section where the precipitation state for an AA6061 Al alloy is predicted and its stability is investigated as a function of temperature. The mechanical threshold stress (MTS), as introduced in section 3.4.2, is strongly related to this material state. It is, for example, independent of temperature and strain rate only as long as its defining material state is. Precipitates, for example, are stable only up to a certain temperature. If they are dissolved, also their contribution to the MTS must vanish. As the material state can be closely followed by thermo-kinetic simulation, MatCalc is also the means of choice when predicting the MTS. A number of models predicting the MTS contribution due to certain strengthening mechanism, e.g. precipitation strengthening (Ahmadi et al., 2014), (Ahmadi et al., 2017), are implemented in MatCalc which are summarized in Table 2.

Table 2

Symbol	Name	MatCalc variable names
$\tau_i$	Basic yield stress of precipitation domain, lattice friction	TYSB\$
$\tau_{ss}$	Solid solution yield stress contribution in precipitation domain	TSS\$
$\tau_{cls}$	Co-Cluster yield stress contribution in precipitation domain	TCLS\$
$\tau_{disl}$	Dislocation yield stress contribution in precipitation domain	TDS\$
$\tau_{gb}$	Fine grain yield stress contribution in precipitation domain	TGS\$
$\tau_{sgb}$	Subgrain yield stress contribution in precipitation domain	TSGS\$
$\tau_{prec}$	Total yield stress contribution from precipitates	TSIGMA_PREC\$

In the next section, a thermal activation framework for yield stress calculation at temperatures  $T > 0$  is derived, where the MTS is treated as input parameter. It is important to note that the temperature and strain rate-dependence of the material state must not be confused with the temperature and strain rate-dependence of the model derived in the next section, which is due to an increase in dislocation mobility while the MTS is assumed to be constant.

#### **4.1.2 The thermal activation framework**

In this section, relations between applied stress, mechanical threshold stress, temperature and strain rate are derived on the basis of an idealized box-shaped, periodical obstacle profile. Although the assumption of such an obstacle profile is highly simplified, it will be shown that important phenomena observed in experiment can be explained and sufficiently well reproduced.

##### **4.1.2.1 Periodical box-shaped obstacle profile**

Fig. (12) shows a schematic view of a box-shaped obstacle profile where a dislocation in equilibrium position 1 (circle) is assumed.

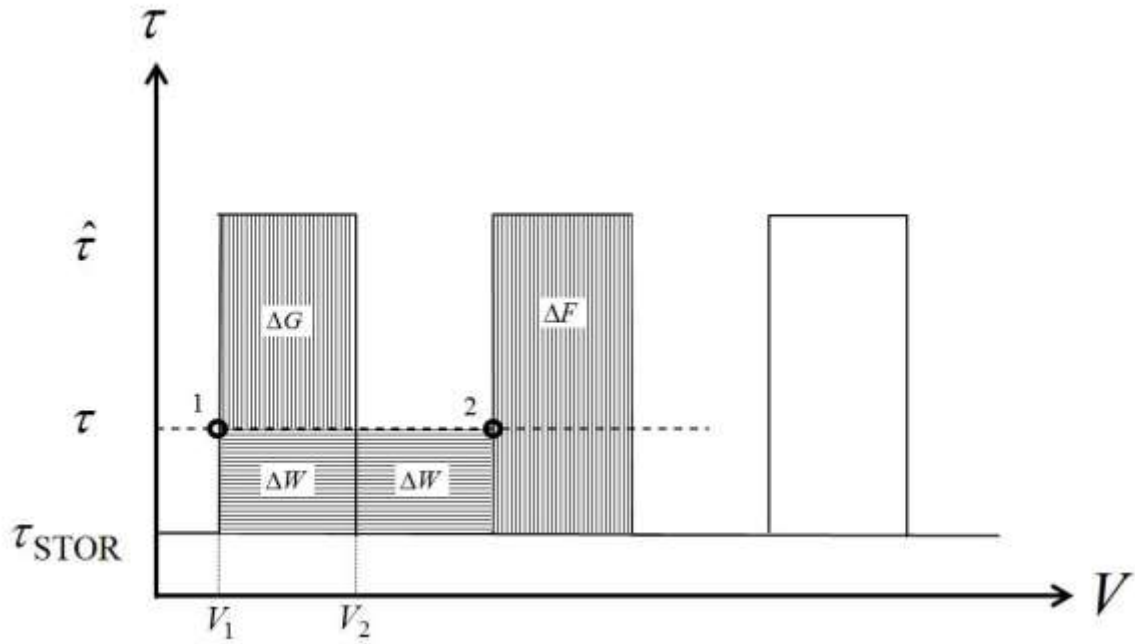


Fig. 12 Schematic view of a periodical, box-shaped obstacle profile in a plot of stress vs. activation volume, with the mechanical threshold,  $\hat{\tau}$ , the critical resolved shear stress,  $\tau$ , and athermal stress,  $\tau_{\text{STOR}}$ . Points 1 and 2 indicate subsequent equilibrium positions.

If a dislocation moves from one equilibrium position (1) to the next (2), a total energy of  $\Delta F$  must be supplied either fully by external work,  $\Delta W$ , (at 0K) or with the help of random thermal fluctuations,  $\Delta G$ . In any case of successful activation

$$\Delta F = \Delta G + \Delta W . \quad (27)$$

For the reverse reaction (2->1), the required energy is

$$\Delta G_b = \Delta G + 2 \cdot \Delta W \quad (28)$$

and must be fully supplied by random thermal fluctuations. As a consequence,  $\Delta G_b > \Delta G$  and the probability for a thermal activation in direction of the applied stress is always higher than that for the reverse reaction. The applied stress 'helps' the dislocation to go from position 1 to 2 and consequently

$$\Delta G = \Delta F - \Delta W . \quad (29)$$

The reverse reaction (2-> 1) is hindered by the applied stress and, with Eqs. (27) and (28), it follows that

$$\Delta G_b = \Delta F + \Delta W . \quad (30)$$

These energies,  $\Delta G$  and  $\Delta G_b$ , are related to the dislocation velocity through an Arrhenius law (Eyring, 1936), (Schoeck, 1965), (Argon, 1996), (Frost and Ashby, 1982) and together with the Orowan equation (Eq. (5)) they give

$$\dot{\varepsilon} = \dot{\varepsilon}_0 \cdot \left[ \exp\left(-\frac{\Delta G(\tau)}{kT}\right) - \exp\left(-\frac{\Delta G_b(\tau)}{kT}\right) \right]. \quad (31)$$

As a consequence of the box shaped obstacle profile and with  $V = (V_2 - V_1)$  and  $\tau \gg \tau_{\text{STOR}}$

$$\Delta W = V\tau, \quad (32)$$

$$\Delta F = V\hat{\tau} \text{ and} \quad (33)$$

$$\Delta W = \Delta F \frac{\tau}{\hat{\tau}}. \quad (34)$$

Together with Eqs. (27)-(30) and with  $\sinh x = 1/2(\exp(x) - \exp(-x))$ , Eq.(31) can be transformed to

$$\dot{\varepsilon} = 2\dot{\varepsilon}_0 \exp\left(-\frac{\Delta F}{kT}\right) \sinh\left(\frac{\Delta W}{kT}\right) = 2\dot{\varepsilon}_0 \exp\left(-\frac{\Delta F}{kT}\right) \sinh\left(\frac{\Delta F}{kT} \frac{\tau}{\hat{\tau}}\right). \quad (35)$$

This is the general rate equation for a box shaped periodical obstacle profile (Kocks et al., 1975). It can be decomposed into a low and a high temperature branch.

#### 4.1.2.2 Low temperature plasticity

At high temperatures or low stresses

$$\Delta G_b \gg \Delta G_f. \quad (36)$$

As a consequence, the second exponential term in Eq. (31) can be neglected leading to

$$\dot{\varepsilon} = \dot{\varepsilon}_0 \cdot \exp\left(-\frac{\Delta G_f(\tau)}{kT}\right). \quad (37)$$

Together with Eqs. (27)-(34), an expression for the temperature and strain rate-dependent yield stress at low and intermediate temperature is given by

$$\tau_{\text{lt}} = \tau_{\text{ath}} + \tau_{\text{th}} = \tau_{\text{ath}} + \hat{\tau} \left( 1 - \left( \frac{kT}{\Delta F} \ln\left(\frac{\dot{\gamma}_0}{\gamma}\right) \right) \right). \quad (38)$$

where  $\tau_{\text{ath}} = \tau_{\text{STOR}}$  is the stress contribution that cannot be overcome with the help of thermal fluctuations (Kocks et al., 1975). It should be emphasized here that Eq. (38) is equivalent to Eq. (8) with  $p=1$  and  $q=1$  and that, with the assumption of an alternative obstacle profile, any other combination of  $p$  and  $q$  can be derived, e.g., see (Schulze and

Vohringer, 2000), (Dahl and Krabiell, 1979) and (Kocks et al., 1975). As indicated earlier, the validity of Eq. (38) is limited at a certain temperature  $T_0$

$$T_0 = \frac{\Delta F}{k \ln\left(\frac{\dot{\gamma}_0}{\dot{\gamma}}\right)} \quad (39)$$

To avoid this problem, an alternative rate equation (Kocks et al., 1975), (Leyson and Curtin, 2016), is used in the present work for the low temperature branch reading

$$\tau = \tau_{\text{ath}} + \hat{\tau} \exp\left(-\frac{kT}{\Delta F} \ln(\dot{\gamma}_0/\dot{\gamma})\right) = \tau_{\text{ath}} + \hat{\tau} \left(\frac{\dot{\gamma}_0}{\dot{\gamma}}\right)^{-\frac{kT}{\Delta F}}. \quad (40)$$

Fig. 13 shows a plot of normalized  $\tau_{\text{th}}/\hat{\tau}$  as a function of homologous temperature according to Eq. (40) in comparison to the same plot but according to Eq. (38).

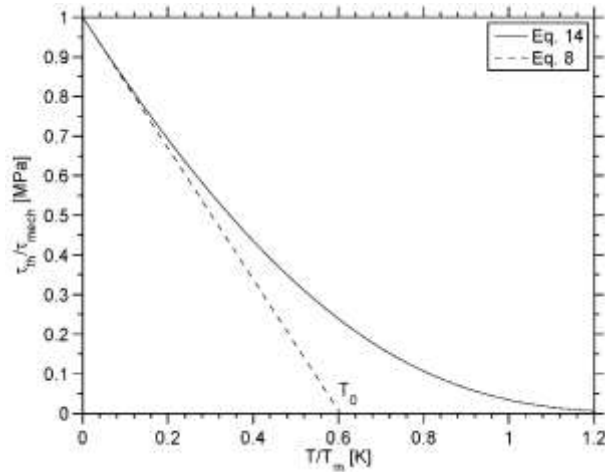


Fig. 13 Schematic comparison between normalized  $\tau_{\text{th}}/\hat{\tau}$  over homologous temperature according to Eq. (58) and Eq. (51)

It is observed that, for low temperatures, both expressions (Eq. (38) and (40)) deliver the same slope  $d\tau/dT$  and that, with an expression according to Eq. (40),  $\tau_{\text{th}} > 0$  for all temperatures.

#### 4.1.2.3 High temperature plasticity

At high temperatures or low stresses  $\Delta W/kT \ll 1$  and consequently with  $\sinh x \approx x$  for  $x < 1$  Eq. (31) can be written as

$$\dot{\epsilon} = 2b\rho c \left(\frac{\tau}{\hat{\tau}}\right) \frac{\Delta F}{kT} \exp\left(-\frac{\Delta F}{kT}\right). \quad (41)$$

Application of the Taylor equation, Eq. (11), on the mobile dislocation density and by rearrangement, an expression for the yield stress at elevated temperatures is derived reading

$$\tau_{ht} = \left( \hat{\tau} \frac{\dot{\epsilon} k T (\alpha b G)^2}{2 b c \Delta F \exp(-\Delta F/kT)} \right)^{1/3}. \quad (42)$$

Comparison of coefficients between Eq. (42) and Eq. (10), with  $n = 3$  and  $\Delta F = Q_v$ , delivers an expression for the Dorn coefficient as function of the mechanical threshold reading

$$A_1 = \frac{2 v_c Q_v}{\alpha^2 b^2 D_{0v} \hat{\tau}}, \quad (43)$$

where  $D_{0v}$  is the pre-exponential factor in the standard Arrhenius-type diffusion coefficient expression.

#### 4.1.2.4 Summation of low and high temperature branch

The present model is based on Eqs. (40), (42) and a summation rule according to

$$\frac{1}{\tau} = \frac{1}{\tau_{lt}} + \frac{1}{\tau_{ht}}. \quad (44)$$

It should be stated here that the summation of Eqs. (40) and (42) according to Eq. (44) is an approximation for the general rate equation for a box-shaped periodical obstacle profile according to Eq. (35). A comparison of  $\tau_{lt}$ ,  $\tau_{ht}$  and  $\tau$  as calculated with Eqs. (40), (42), (44) and (35), is shown in Fig. 14.

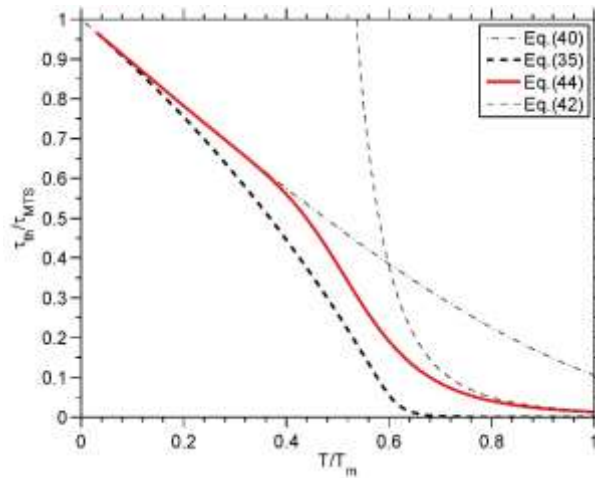


Fig. 14 Comparison of  $\tau_{lt}$ ,  $\tau_{ht}$  and  $\tau$  as calculated with Eqs. (40), (42), (44) and (35).  $\Delta F$  is assumed to be  $0.3Gb^3$ .

Fig. 14 shows that the results from the summation of  $\tau_{lt}$  and  $\tau_{ht}$  according to Eq. (44) (thick solid line) generally appear to be in good accordance with  $\tau$  as calculated from Eq. (35) (dashed thick line) with some discrepancy occurring at intermediate temperatures. However, this discrepancy is mainly due to the generally accepted assumption (Frost and Ashby, 1982) that the mobile dislocation density in Eq. 41 varies with the applied stress according to the Taylor equation and is not due to the summation rule Eq. (44). Fig. 15 shows the same results like Fig. 14 but for varying values of (a)  $\Delta F$  and (b) strain rate from 0.01-1000  $s^{-1}$ . It is observed that the discrepancy is only slightly varying with the activation energy and the strain rate.

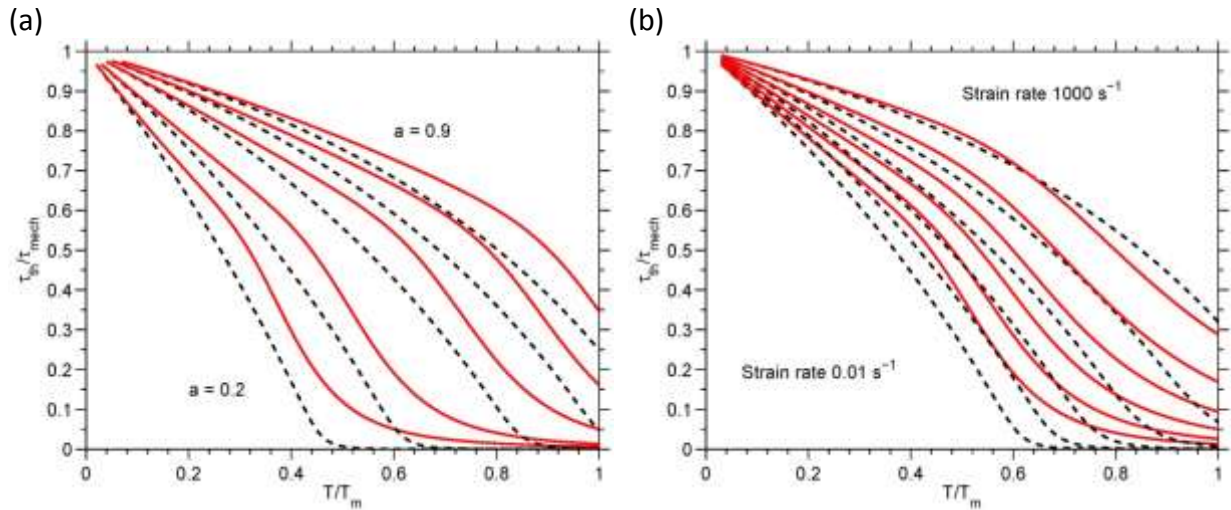


Fig. 15 (a) Variation of  $a$  (0.2, 0.3, 0.5, 0.7 and 0.9) and (b) variation of strain rate (0.01, 0.1, 1, 10, 100 and 1000).

## 4.2 Plastic stress $\sigma_p$

The model for the plastic stress is based on an equivalent form of the KM-model, Eq. (22), reading

$$\frac{\partial \rho}{\partial \varepsilon} = \frac{d\rho^+}{d\varepsilon} + \frac{d\rho_d^-}{d\varepsilon} = \frac{M}{bA} \sqrt{\rho} - 2BM \frac{d_{crit}}{b} \rho, \quad (45)$$

where the first term on the rhs of this equation is further denoted as “A-term”, due to the calibration coefficient  $A$ , the second term likewise as “B-term”. For a detailed derivation and explanation of  $A$  and  $B$ -terms see Appendix A. The subscript “d” emphasizes that the

dislocation annihilation term refers to dynamic recovery.  $d_{\text{crit}}$  is the critical annihilation distance between two dislocations (Brinckmann et al., 2011) given as

$$d_{\text{crit}} = \frac{Gb^4}{2\pi(1-\nu)Q_{\text{vac}}}, \quad (46)$$

where  $Q_{\text{vac}}$  is the vacancy formation energy and  $\nu$  is Poisson's ratio. The coefficient  $A$  is closely related to the number of immobile dislocations that a moving dislocation can surpass before it becomes arrested. The coefficient  $B$  represents the inverse of the probability of a dislocation to become annihilated under the condition of having a second dislocation within the critical distance. At elevated temperature, the evolution of dislocation density becomes additionally impacted by vacancy-assisted dislocation climb. To incorporate this mechanism in a general model of strain hardening based on dislocation generation and annihilation, an additional annihilation term for static recovery might be introduced into Eq. (45) with

$$\frac{d\rho_s^-}{d\varepsilon} = -2CD_d \frac{Gb^3}{\dot{\varepsilon}kT} (\rho^2 - \rho_{\text{eq}}^2), \quad (47)$$

where the rhs of this equation will be further denoted as "C-term", due to the calibration coefficient  $C$ , and the subscript "s" emphasizing that this dislocation annihilation term refers to static recovery.  $\rho_{\text{eq}}$  is the equilibrium dislocation density and  $D_d = D_{d0} \exp(-Q_d/RT)$  is the diffusion coefficient along dislocation pipes. This recovery term has been introduced by (Lagneborg, 1972) for creep and it is used in a similar form, for instance, by (Sommitsch, 1999), (Krumphals et al., 2009) and (Lindgren et al., 2008). With  $\dot{\varepsilon} = d\varepsilon/dt$ , the static recovery term delivers non-zero dislocation annihilation for  $\dot{\varepsilon} = 0$ , capturing the process of annealing (Nix et al., 1985), (Nes, 1994), (Falkinger and Simon, 2017), (Rong et al., 2017), (Hamasaki et al., 2017), (Zheng et al., 2017), (Furu et al., 1995). The combined equation for dislocation density evolution finally reads

$$\frac{d\rho}{d\varepsilon} = \frac{d\rho^+}{d\varepsilon} - \frac{d\rho_d^-}{d\varepsilon} - \frac{d\rho_s^-}{d\varepsilon}. \quad (48)$$

Due to the parameters  $A$ ,  $B$  and  $C$ , this extended version of the KM-model is referred to as ABC-model. The following analysis of the ABC-model is based on the assumption that the C-term,  $d\rho_s^-/d\varepsilon$ , can be neglected at low temperatures and the B-term,  $d\rho_d^-/d\varepsilon$ , can be neglected at elevated temperatures. The validity of this assumption is tested in the following by analysis of the saturation stress.

### 4.2.1 Saturation stress

The saturation stress is related to dislocation density at saturation through the Taylor equation  $\sigma_\infty = g_1 \sqrt{\rho_\infty}$ . The relation between  $\rho_\infty$  and  $A$ ,  $B$  and  $C$  can be derived by setting  $d\rho_\infty/d\varepsilon = 0$ . This is done first for low temperatures, where the C-term is neglected, delivering

$$0 = \frac{M}{bA} \sqrt{\rho_\infty^{\text{lt}}} - \frac{2BMd_{\text{crit}}}{b} \rho_\infty^{\text{lt}} . \quad (49)$$

Rearrangement of Eq. (49) leads to

$$\rho_\infty^{\text{lt}} = \left( \frac{1}{2ABd_{\text{crit}}} \right)^2 \quad (50)$$

and with Eqs.(11) and (46), the low temperature saturation stress,  $\sigma_\infty^{\text{lt}}$ , is written as

$$\sigma_\infty^{\text{lt}} = \frac{g_1}{2ABd_{\text{crit}}} = \frac{\alpha M \pi (1-\nu) Q_{\text{vac}}}{ABb^3} . \quad (51)$$

According to Eq. (51), the low temperature saturation stress,  $\sigma_\infty^{\text{lt}}$ , does not contain any explicit temperature dependence not even through the shear modulus. Consequently, any temperature or strain rate dependence of  $\sigma_\infty^{\text{lt}}$  either stems from the calibration of parameter  $A$  or  $B$ . At elevated temperatures, the B-term is assumed to be negligible and, with  $\rho_\infty^{\text{ht}} \gg \rho_{\text{eq}}$ , this leads to

$$0 = \frac{M}{bA} \sqrt{\rho_\infty^{\text{ht}}} - 2CD_d \frac{Gb^3}{\dot{\varepsilon}kT} \rho_\infty^{\text{ht}^2} . \quad (52)$$

Rearrangement of Eq. (52) delivers

$$\rho_\infty^{\text{ht}} = \left( \frac{M}{bA} \frac{kT}{2CD_d Gb^3} \right)^{2/3} \quad (53)$$

and, with Eq.(11), the saturation stress at elevated temperatures,  $\sigma_\infty^{\text{ht}}$ , is written as

$$\sigma_\infty^{\text{ht}} = g_1 \left( \frac{M}{bA} \frac{\dot{\varepsilon}kT}{2CD_d Gb^3} \right)^{1/3} . \quad (54)$$

Eq. (54) shows that the saturation stress at high temperature is strain rate-dependent by definition even when  $A$  and  $C$  are assumed temperature and strain rate-independent. With constants  $A$  and  $C$ , Eq. (54) describes a power-law according to Eq. (10). Assuming that the saturation stress is properly described by a power-law, it follows that the product of  $A$  and  $C$  must be independent of temperature and strain rate and, consequently,  $C = k_3/A$ , where  $k_3$  is a constant. Fig. 16 shows a comparison of  $\sigma_\infty^{\text{lt}}$  as calculated with Eq. (51),  $\sigma_\infty^{\text{ht}}$  as

calculated with Eq. (54) and  $\sigma_\infty$  as calculated by numerically solving Eq. (48) as function of homologous temperature.

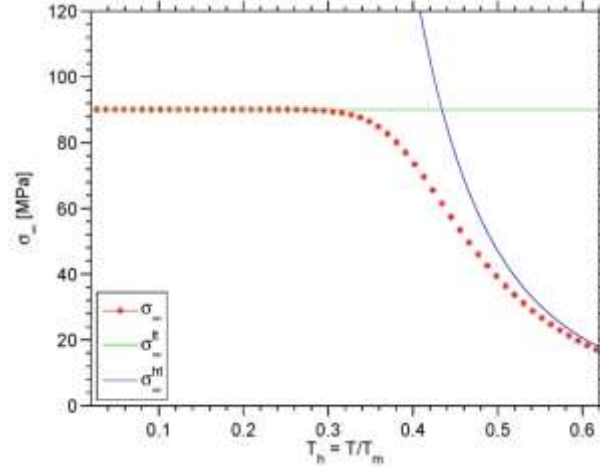


Fig. 16 Comparison of  $\sigma_\infty^{\text{lt}}$  as calculated with Eq. (51),  $\sigma_\infty^{\text{ht}}$  as calculated with Eq. (54) and  $\sigma_\infty$  as calculated by numerical integration of Eq. (48) with constant parameters  $A = 35$ ,  $B = 5$  and  $C = 0.01$ .

Fig. 16 confirms the assumption that, at low temperatures, the C-term can be neglected and, at high temperatures, the B-term can be neglected. In addition, the observation is confirmed that the low temperature saturation stress does not exhibit any temperature-dependence for  $A = \text{const.}$  and  $B = \text{const.}$ . Following a suggestion of (Kocks and Mecking, 2003), the temperature-dependence of the B parameter can be taken into account by assuming

$$B = B_0 \left( 1 - \frac{kT}{aGb^3} \ln \left( \frac{\dot{\epsilon}_0}{\dot{\epsilon}} \right) \right)^{-1}, \quad (55)$$

where  $B_0$  and  $a$  are calibration parameters. Fig. 17 shows the same comparison as in Fig. 16 but with Eq. (55) for  $B$  instead of  $B = \text{const.}$ .

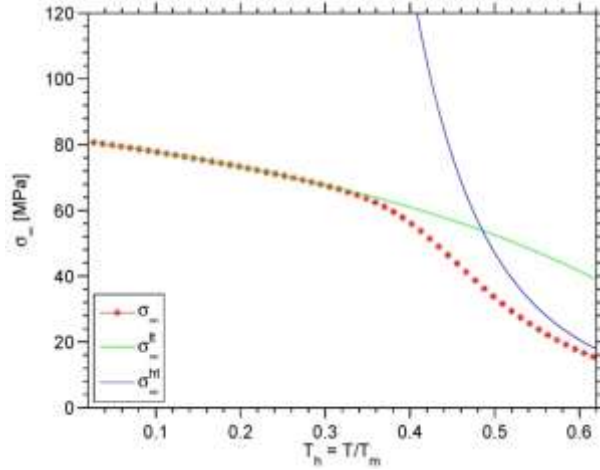


Fig. 17 comparison of  $\sigma_{\infty}^{lt}$  as calculated with Eq. (51),  $\sigma_{\infty}^{ht}$  as calculated with Eq. (54) and  $\sigma_{\infty}$  as calculated by numerical solving of Eq. (48) with constant  $A=35$ ,  $C=0.01$ .  $B$  is calculated according to Eq. (55) with  $B_0=5$  and  $a=1.2$ .

#### 4.2.2 Initial strain hardening rate

In this section, the relations between the initial strain hardening rate and the parameters  $A$ ,  $B$  and  $C$  are derived. Together with eq. (11), the strain hardening rate can be written as

$$\theta = \frac{d\sigma}{d\varepsilon} = \frac{g_1}{2} \frac{1}{\sqrt{\rho}} \frac{d\rho}{d\varepsilon} \quad (56)$$

Setting  $\rho = \rho_0$  it follows that  $\theta = \theta_0$ . Rearrangement of Eq. (56) leads to

$$\frac{d\rho_0}{d\varepsilon} = \frac{2\theta_0\sqrt{\rho_0}}{g_1}. \quad (57)$$

Assuming that the C-term is negligible at low temperatures, it follows from Eq. (45) that

$$\frac{2\theta_0^{lt}\sqrt{\rho_0}}{g_1} = \frac{M}{bA}\sqrt{\rho_0} - \frac{2BMd_{crit}}{b}\rho_0, \quad (58)$$

with Eq. (51)  $B$  can be replaced by

$$B = \frac{g_1}{2A\sigma_{\infty}^{lt}d_{crit}} \quad (59)$$

in Eq. (58) and rearrangement leads to

$$\theta_0^{lt} = \frac{g_1M}{2bA} \left( 1 - \frac{g_1\sqrt{\rho_0}}{\sigma_{\infty}^{lt}} \right), \quad (60)$$

where  $g_1\sqrt{\rho_0}$  is the stress contribution from forest hardening with a dislocation density of  $\rho_0$ . Since  $g_1\sqrt{\rho_0} \ll \sigma_{\infty}^{lt}$  it follows that

$$\theta_0^{\text{lt}} = \theta_0 \cong \frac{g_1 M}{2bA}. \quad (61)$$

At elevated temperatures and with neglecting the B-term, the equivalent high temperature form of Eq. (58) reads

$$\frac{2\theta_0^{\text{ht}} \sqrt{\rho_0}}{g_1} = \frac{M}{bA} \sqrt{\rho_0} - 2CD_d \frac{Gb^3}{\dot{\epsilon}kT} (\rho_0^2 - \rho_{\text{eq}}^2). \quad (62)$$

With  $\rho_0^2 \approx \rho_{\text{eq}}^2$ , the second term in Eq. (62) can be neglected and it follows that also at high temperatures

$$\theta_0^{\text{ht}} = \theta_0 \cong \frac{g_1 M}{2bA}. \quad (63)$$

### 4.2.3 Thermal activation of the ABC model

By inversion of Eqs. (51), (54) and (63)  $A$ ,  $B$  and  $C$  can be expressed in terms of  $\theta_0$ ,  $\sigma_\infty^{\text{lt}}$  and  $\sigma_\infty^{\text{ht}}$  reading

$$A = \frac{g_1 M}{2b\theta_0}, \quad (64)$$

$$B = \frac{b\theta_0}{\sigma_\infty^{\text{lt}} d_{\text{crit}} M}, \quad (65)$$

$$C = \frac{g_1^2}{(\sigma_\infty^{\text{ht}})^3} \frac{\theta_0 \dot{\epsilon} k T}{D_d G b^3}, \quad (66)$$

and can thus be directly calculated from experimentally derived values for  $\theta_0$ ,  $\sigma_\infty^{\text{lt}}$  and  $\sigma_\infty^{\text{ht}}$  or, alternatively, from the models describing  $\sigma_0 = \sigma_0(T, \dot{\epsilon}, s_1, s_2, \dots)$ ,  $\theta_0 = \theta_0(T, \dot{\epsilon}, s_1, s_2, \dots)$  and  $\sigma_\infty = \sigma_\infty(T, \dot{\epsilon}, s_1, s_2, \dots)$ , where  $s_1, s_2, \dots$  stands for any combination of state parameters such as solute content or precipitation state. In principle, any model can be applied for the expression of  $\sigma_0$ ,  $\theta_0$  and  $\sigma_\infty$  as a function of temperature, strain rate and material state. In literature, it is rather common to assume one quantity as being constant, e.g.  $\theta_0$  in (Roters et al., 2000), (Galindo-Nava et al., 2012), (Nes, 1997), (Kocks, 1976), which is not applied in the present work. In the present work, a suggestion for functional relations between  $\sigma_0$ ,  $\theta_0$  and  $\sigma_\infty$ , temperature, strain rate and material state is given in the simulation section, which is based on the analysis of experimentally derived values and the thermal activation framework as introduced in section 4.1.2.

#### 4.2.4 Stage IV extension for the ABC model

The strain hardening rate in stage IV  $\theta_{IV} = d\sigma_{IV}/d\varepsilon$  is – according to (Kocks and Mecking, 2003) – related to the stress at the onset of stage IV through a simple linear relation

$$\theta_{IV} = c_{IV}\sigma_{IV}, \quad (67)$$

where  $c_{IV}$  is a constant. Fig. 18 shows schematic stress strain curves with stages III and IV hardening for different temperatures together with a corresponding Kocks-plot illustrating Eq. (67).

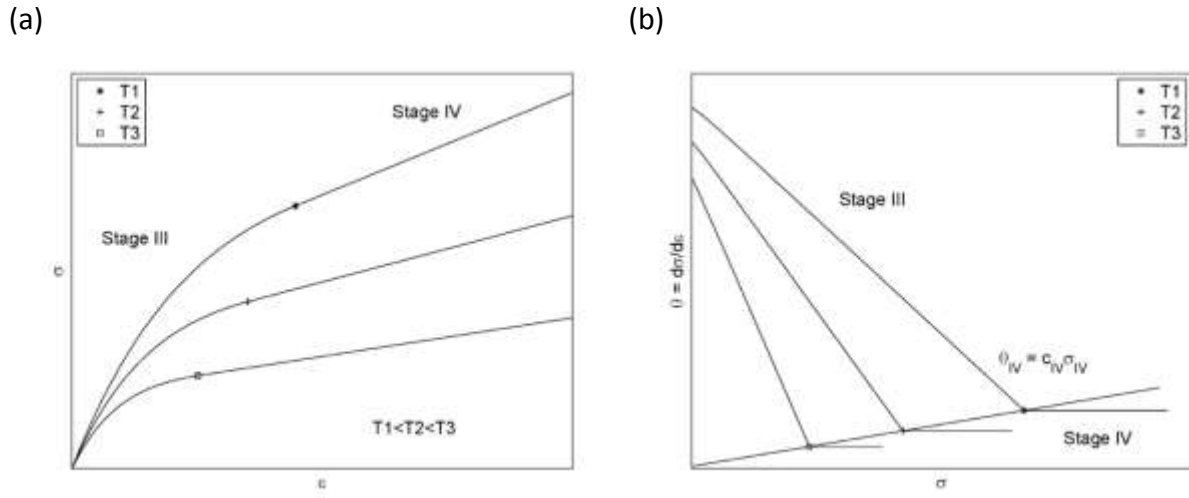


Fig. 18 (a) Schematic view of stress-strain curves for three different temperatures (b) Strain hardening rate over stress (Kocks-Plot) for data in (a)

At the point of intersection, the general KM law in the form of Eq. (22) reads

$$\theta_{IV} = \theta_0 - \frac{\theta_0}{\sigma_\infty} \sigma_{IV}. \quad (68)$$

Solving Eqs. (67) and (68) for  $\theta_{IV}$  results in

$$\theta_{IV} = \frac{\theta_0 c_{IV} \sigma_\infty}{\theta_0 + c_{IV} \sigma_\infty}. \quad (69)$$

This equation connects a given temperature or strain rate-dependence of  $\theta_0$  and  $\sigma_\infty$  in stage III with that of  $\theta_{IV}$ . Finally, the expression for  $\theta_{IV}$  is integrated in the evolution model for the dislocation density according to

$$\frac{dr}{de} = \max\left(\frac{2q_0}{g_1} \sqrt{r} - \frac{2q_0}{s_\infty} r, \frac{2q_{IV}}{g_1} \sqrt{r}\right). \quad (70)$$

# 5 Experimental

In section 4, the modelling framework has been derived and explained. The experimental part of the present work constitutes a collection of data for the validation and calibration of this model. The experimental set up comprises stress strain curves from compression testing in an AA 6061 aluminium alloy tested at eleven different temperatures and three different artificial ageing states. Additionally, EBSD analysis is conducted on a sub-set of deformed samples. According to the nature of the present model, the data analysis of stress strain curves is conducted with special emphasis on the initial yield stress,  $\sigma_0$ , the initial strain hardening rate,  $\theta_0$ , and the saturation stress,  $\sigma_\infty$ , as a function of material state, temperature and strain rate. Section 5 additionally illustrates the data preparation procedure that was applied both to data from literature and experiments conducted by the present author.

## 5.1 Material and sample preparation

Cylindrical specimens with a length of 15 mm and a diameter of 10 mm are extracted by spark erosion from commercial A6061 plate material. The chemical composition of the material is listed in Table (3).

Table 3 Chemical Composition

Element [wt.%]	Al	Si	Fe	Cu	Mn	Mg	Cr	Ni	Zn	Ti
AA 6061	97.35	0.69	0.45	0.23	0.11	0.85	0.18	<0.05	0.05	0.05

The industrially cast and homogenized material has been hot rolled into 30 mm thick sheets. Specimens are cut out along the Normal Direction (ND), perpendicular to the Rolling Direction (RD). Fig. 19 shows the hot rolled 300x300x30 mm AA6061 plate and the rolling as well as the sample extraction direction (ND).

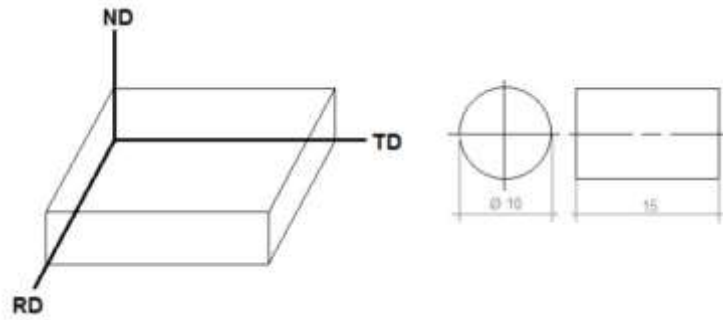


Fig. 19 Schematic view of AA6061 plate and sample dimensions.

## 5.2 Thermo-mechanical treatment

The material is solution heat treated for 1h at 540°C in a furnace, water quenched and, after storage at room temperature for one week, artificially aged for 1, 4 and 8h at 170°C. All specimens are subsequently tested on a Gleeble 1500 thermo-mechanical simulator at a strain rate of 0.01 s<sup>-1</sup> and at temperatures of 25, 50 100, 150, 200, 250, 300, 350, 400, 450 and 500°C. The tests are repeated three times, the experimental values represent the average of three experiments. The experimental data has been published in (Kreyca and Kozeschnik, 2017a). A subset of samples, heat treated for 4h at 170°C after solution heat treatment and deformed at 25, 150, 200, 350, 400 and 450°C up to a strain level of 0.2 is investigated by EBSD. Fig. 20 shows a schematic view of the EBSD sample preparation and mounting.

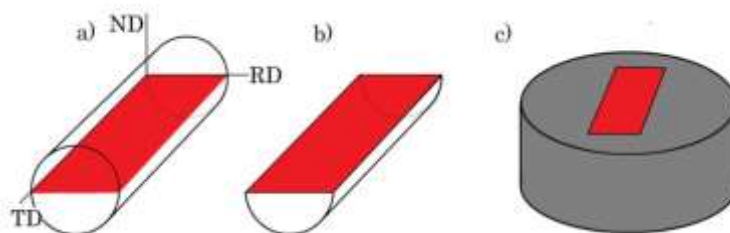


Fig. 20 Schematic view of EBSD sample cutting and mounting

Prior to mounting, the specimens are degreased with alcohol and dried with a blow dryer. The specimens are cold mounted in a conductive mounting material (CEM 3070) and water cooled during the curing process in order to avoid annealing due to sample preparation. The steps for grinding and polishing are summarized in Table 4.

Table 4 Grinding and polishing

Step	Polishing Disc	Grit ( $\mu\text{m}$ )	Time (min)
Grinding	Abrasive Paper	500	2
Polishing	Struers MD Largo	9	15
Polishing	Struers MD Dur	6	25
Polishing	Struers MD Mol	3	30
OPS	Struers MD-Chem	1	15
Cleaning	Struers MD-Chem	1	3

The EBSD investigations are performed on an FEI Quanta 200 FEG. The data analysis is conducted with the EDAX Orientation Imaging Microscopy (OIM) Data Analysis software.

### 5.3 Data preparation

Stress-strain curves are calculated from Gleeble output files as true stress and true strain according to Eqs. (1) and (2). The actual cross-section is calculated from the measured length and with the assumption of constant volume and no barrelling. Values for  $\sigma_0$  are taken at a strain of  $\varepsilon = 0.02$ . Accordingly, the plastic strain is assumed to be  $\varepsilon_p = \varepsilon - 0.02$ . The experimental values for  $\theta_0$  and  $\sigma_\infty$  are evaluated from the KM-plots ( $\theta$  vs.  $\sigma$ ) of the experimental data, where  $\theta$  is determined from numerical differentiation. Values of  $\sigma_p = \sigma - \sigma_0$  are used for calculation of the KM-plots. For the purpose of numerical differentiation, the experimental data is smoothed.

Fig. 21 (a) shows an exemplary plot of  $\sigma_p$  vs.  $\varepsilon$  together with smoothed values (signs) (b) shows the strain hardening rate as calculated by numerical differentiation of the original stress-strain curve (solid line) in comparison to the strain hardening rate as calculated from numerical differentiation of the smoothed data (signs). Initial strain hardening rate,  $\theta_0$ , and saturation stress,  $\sigma_\infty$ , are derived by minimization of the sum of least squares of the  $\theta$  vs.  $\sigma_p$  plot. Fig. 21 (c) shows a corresponding linear fit of the experimental data. The initial strain hardening rate,  $\theta_0$ , and saturation stress,  $\sigma_\infty$ , are calculated from the slope,  $h_2$ , and y-intercept,  $h_1$ , of the resulting straight line equation according to

$$\theta_0 = h_1 \text{ and} \quad (71)$$

$$\sigma_\infty = \frac{h_1}{h_2}. \quad (72)$$

Fig. 21 (d) shows the stress-strain curve resulting from integration of

$$\theta = \frac{d\sigma_p}{d\varepsilon} = \theta_0 \left( 1 - \frac{\sigma_p}{\sigma_\infty} \right) = h_1 - h_2 \sigma_p \tag{73}$$

in comparison to experimental results.

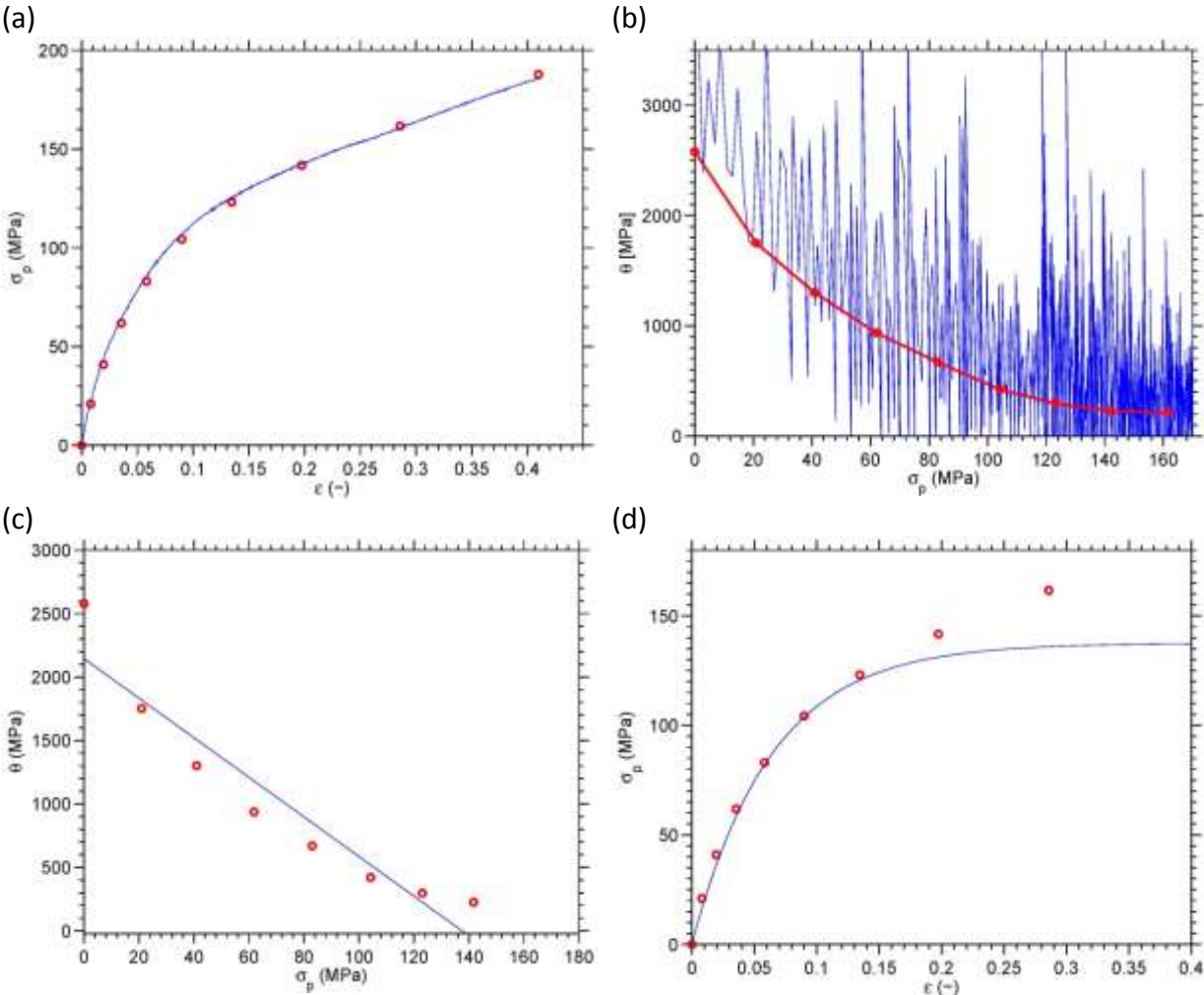


Fig. 21 (a) Exemplary stress strain curve together with smoothed values (b) corresponding Kocks-plot, (c) linear fits of Kocks-plot (solid line) (d) resulting stress strain curves calculated according to linear fit in (c).

## 6 Simulation

This section comprises three separate simulations: (i) an investigation of the thermal stability of hardening phases, i.e. the material state, in AA6061 and (ii) application of the stage IV model as introduced in section 4.2.4 and (iii) an application of the present model to Al-Mg binary solid solutions,

### 6.1 AA 6061

In this section, the thermal stability of hardening phases in an AA6061 aluminium alloy is investigated. For this purpose, the initial precipitation state prior to deformation is calculated with MatCalc. This work was published in (Kreyca and Kozeschnik, 2017a). Additionally, a calibration on AA6061 of the stage IV model as introduced in section 4.2.4 is presented. These results have also been published in (Kreyca and Kozeschnik, 2017b).

#### 6.1.1 Precipitation sequence

Fig. 22 shows the typical precipitation sequence observed during heat treatment of Al-Mg-Si alloys (Matsuda et al., 1998) and (Vissers et al., 2007).

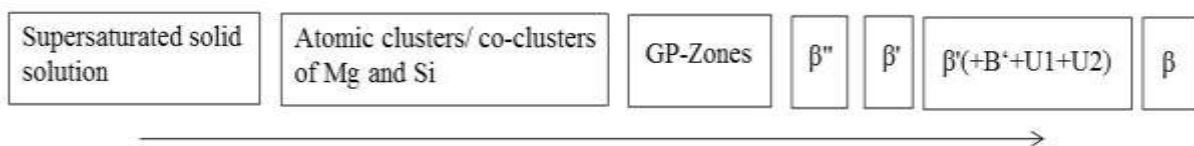


Fig. 22 Typical precipitation sequence in Al-Mg-Si alloys

In the Al-Mg-Si system, the mechanical properties mainly result from precipitation strengthening of Mg and Si-containing particles. In AA6061 alloys,  $Mg_5Si_6$  ( $\beta'''$ ) is the major hardening phase (Ninive et al., 2014), (Marioara et al., 2005), (Ravi and Wolverton, 2004), (Zandbergen et al., 2015). In the present simulation, the precipitation sequence occurring during heat treatment of a model Al-Mg-Si ternary alloy is simulated. The chemical composition (0.85 wt.% Mg, 0.69 wt.% Si, Al bal.) lies well within the range defined for

AA6061 aluminium. The phases GP-zones,  $\beta'$  and  $\beta''$ , are incorporated in the simulation. All calculations presented here are performed with the thermo-kinetic software package MatCalc (version 6.00 rel. 0.104) (Kozeschnik, 2017) using the databases *mc\_al.tdb* (Povoden-Karadeniz, 2017a) and *mc\_al.ddb* (Povoden-Karadeniz, 2017b). These databases are available under the Open Database License ("Open database license," n.d.) and can be downloaded for free from <http://matcalc.at>. They contain all thermodynamic and diffusion related parameters necessary for the reproduction of the present results. The interface energies are calculated according to the generalized nearest neighbour broken bond model (Sonderegger and Kozeschnik, 2009a), (Sonderegger and Kozeschnik, 2009b). This approach is coupled with a model describing the evolution of quenched-in excess vacancies (Fischer et al., 2011) and their impact on solute diffusion. The influence of coherent misfit stress on nucleation is taken into account by assuming an effective volumetric misfit between precipitates and matrix of 4, 4, and 2 % for GP-zones,  $\beta'$  and  $\beta''$ , respectively. The phases  $\beta'$  and  $\beta''$  are assumed to be rod-shaped with an aspect ratio of  $H/D=10$  (Kozeschnik et al., 2006) where  $H$  is the length of the precipitate, and  $D$  the thickness of a cylinder with equivalent volume. The heat treatment comprises a quenching step from annealing temperature to room temperature with  $900 \text{ Ks}^{-1}$ , subsequent heating with  $3 \text{ Ks}^{-1}$  and isothermal holding at  $170^\circ\text{C}$  for 4h.

### 6.1.2 Thermal stability of $\beta''$

The phase fraction and precipitate distribution of  $\beta''$  particles corresponding to the precipitation state according to the prior heat-treatment is subsequently used as starting condition for the simulation of the dissolution/growth kinetics of the  $\beta''$  phase during isothermal mechanical testing. Fig. 23 shows a schematic representation of the evolution of phase fraction during isothermal heat treatment at different temperatures. The isothermal heat-treatment simulations are conducted twice: (i) for 70s at incremental temperature steps of  $10^\circ\text{C}$  from room temperature up to  $500^\circ\text{C}$  and (ii) for 1000h at incremental temperature steps of  $10^\circ\text{C}$  from room temperature up to  $300^\circ\text{C}$ .

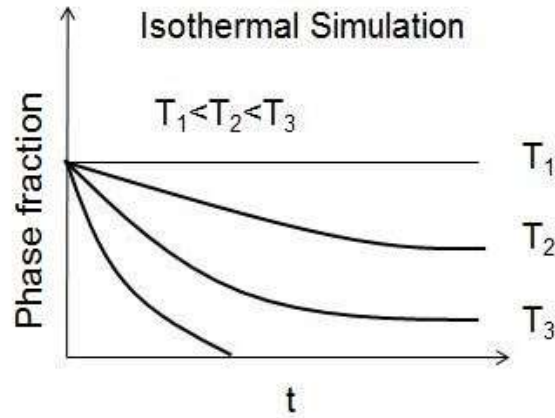


Fig. 23 Schematic representation of phase fraction evolution as function of different heat-treatment temperatures.

The resulting phase fraction evolutions are depicted in a plot of temperature vs. time, where the phase fraction evolution is represented by color-coding.

### 6.1.3 Stage IV

In section 4.2.4, an extension of the KM-model to stage IV hardening is introduced and explained. This approach is utilized for the reproduction of the experimentally derived stress-strain curves on an artificially aged AA6061 alloy (4h at 170°C) deformed at 25, 50, 100, 150 and 200°C, see section 5. For this purpose,  $A$  and  $B$  values are calculated with Eqs. (64) and (65) with the experimental values of  $\theta_0$  and  $\sigma_\infty$  derived according to the procedure described in section 5.3. Subsequently, stress-strain curves are calculated with Eqs. (67)-(70) and Eq. (5). All parameters used in the simulation are listed in Table 5.

Table 5 Parameters used in modeling (at 25, 50, 100, 150 and 200°C)

Abbreviation	Name	Value	Unit
$b$	Burgers vector	$2.85 \cdot 10^{-10}$	(m)
$M$	Taylor factor	3.06	(-)
$G$	Shear modulus	$29438.4 - 15.052 \cdot T$	(MPa)
$\dot{\epsilon}$	Strain rate	0.01	(-)
$\nu$	Poisson's ratio	0.3	(-)
$Q^v$	Vacancy formation energy	0.67	(eV)
$\alpha$	Coefficient for inner dislocation density strengthening	0.5	(-)
$A$	Dislocation production parameter	26, 26, 27.6, 33.38, 35.07	(-)
$B$	Dislocation annihilation parameter	3.98, 4.3, 4.76, 4.95, 6.74	(-)
$c_{IV}$	Stage IV coupling coefficient	1.5	(-)

## 6.2 Solid solutions

The model described in section 4 is tested on experimental data on Al-Mg binary alloys reported by (Sherby et al., 1951). This reference has been given preference over other sources from literature on Al-Mg (Podkuiko et al., 1972), (Kocks and Chen, 1993), (Verdier et al., 1998), (Ryen et al., 2006a), (Ryen et al., 2006b), (Niewczas et al., 2015), (Jobba et al., 2015) because it offers a consistent experimental set of stress strain curves for five different Al-Mg alloys at seven different temperatures from 78K to 650K. In the selected Al-Mg system, precipitation processes can be neglected. The preparation of the experimental data is reported in section 5.3. The values of  $\sigma_0$ ,  $\theta_0$  and  $\sigma_\infty$  derived from the experimental data are fitted with the expressions listed in Table 6. The expressions for  $\sigma_0$  and  $\theta_0$  are chosen according to the thermal activation framework derived in section 4.1.2.

Table 6 Expressions for  $\sigma_0$ ,  $\theta_0$  and  $\sigma_\infty$

	low temperature	high temperature	summation
$\sigma_0$	$\sigma_0^{\text{lt}} = \hat{\sigma}_0 \exp\left(-\frac{kT \ln(\dot{\epsilon}_0/\dot{\epsilon})}{\Delta F_{\sigma_0}^{\text{lt}}}\right)$	$\sigma_0^{\text{ht}} = \left(\frac{\hat{\sigma}_0 g_1^2 \dot{\epsilon} k T}{2bc \exp(-\Delta F_{\sigma_0}^{\text{ht}}/kT) \Delta F_{\sigma_0}^{\text{ht}}}\right)^{1/3}$	$\frac{1}{\sigma_0} = \frac{1}{\sigma_0^{\text{lt}}} + \frac{1}{\sigma_0^{\text{ht}}}$
$\theta_0$	$\theta_0^{\text{lt}} = \hat{\theta}_0 \exp\left(-\frac{kT \ln(\dot{\epsilon}_0/\dot{\epsilon})}{\Delta F_{\theta_0}^{\text{lt}}}\right)$	$\theta_0^{\text{ht}} = \left(\frac{\hat{\theta}_0 g_1^2 \dot{\epsilon} k T}{2bc \exp(-\Delta F_{\theta_0}^{\text{ht}}/kT) \Delta F_{\theta_0}^{\text{ht}}}\right)^{1/3}$	$\frac{1}{\theta_0} = \frac{1}{\theta_0^{\text{lt}}} + \frac{1}{\theta_0^{\text{ht}}}$
$\sigma_\infty$	$\sigma_\infty^{\text{lt}} = \hat{\sigma}_\infty \left(1 - \exp\left(-\frac{kT \ln(\dot{\epsilon}_0/\dot{\epsilon})}{\Delta F_{\sigma_\infty}^{\text{lt}}}\right)\right)^{-1}$	$\sigma_\infty^{\text{ht}} = g_1 \left(\frac{M \dot{\epsilon} k T}{2b D_{d0} \exp(-\Delta F_{\sigma_\infty}^{\text{ht}}/kT) G b^3}\right)^{1/3}$	no summation

The framework presented in Table 6 comprises 9 parameters, which are: the mechanical threshold,  $\hat{\sigma}_0$ , the initial strain hardening rate at 0K,  $\hat{\theta}_0$ , a calibration parameter for the saturation stress,  $\hat{\sigma}_\infty$ , and two activation energies for each of the three quantities  $\Delta F_x^{\text{lt}}$  and  $\Delta F_x^{\text{ht}}$ , where x stands for the individual parameter. These parameters are discussed in the following. For the calculation of the mechanical threshold stress,  $\hat{\sigma}_0$ , two contributions are considered,

$$\hat{\sigma}_0 = \hat{\sigma}_b + \hat{\sigma}_{ss}, \quad (74)$$

where  $\hat{\sigma}_{ss}$  comprises all strengthening contributions from Mg solute atoms including dynamic strain ageing and  $\hat{\sigma}_b$  includes all contributions, which are not directly related to Mg solute atoms, e.g., the basic yield stress from pure Al, grain boundary strengthening and solid solution hardening from other impurity elements.  $\hat{\sigma}_b$  is treated as a temperature and

strain rate-independent calibration parameter in the present simulation. The MTS contribution of solute atoms,  $\hat{\sigma}_{ss}$ , is based on a Labusch type approach (Labusch, 1970) in combination with a model on dynamic strain ageing by (Curtin et al., 2006). The explicit relations read

$$\hat{\sigma}_{ss} = \left( \frac{f_{\max}^4 c_{\text{eff}}^2 w}{8E_L b^7} \right)^{1/3} = \left( \frac{f_{\max}^4 c_{\text{eff}}^2 w}{4Gb^9} \right)^{1/3} \quad (75)$$

with

$$f_{\max} = \frac{\sqrt{3}}{2} \left( \frac{1+\nu}{1-\nu} \right) Gb^2 |\varepsilon_m| \quad (76)$$

and

$$c_{\text{eff}} = c_0 + c_0 \tanh\left(\frac{\Delta W}{2kT}\right) \left[ 1 - \exp\left(\left(-6 \cosh\left(\frac{\Delta W}{2kT}\right) \Gamma_c \frac{\Omega}{\dot{\varepsilon}}\right)^n\right) \right], \quad (77)$$

where  $w = 5b$  (Kato, 1999) is the range of interaction between a solute and a dislocation,  $f_{\max}$  is the maximum interaction force,  $E_L = Gb^2/2$  (Haasen, 1996) is the dislocation line tension,  $\varepsilon_m$  the misfit strain between solute and matrix atoms,  $c_0$  the nominal solute content,  $\Omega = b\rho^{1/2}$  is the incremental strain,  $\Gamma_c = \nu_0 \exp(-\Delta H_c/kT)$  is a reference core transition rate,  $\Delta W$  is the average binding energy difference between tension and compression site,  $\Delta H_c$  is the average activation enthalpy for transitions between these sites,  $\nu_0$  is an attempt frequency and  $n$  is an exponent. According to Eq. (77), the material state represented by the effective solute content,  $c_{\text{eff}}$ , is a function of temperature and strain rate. Consequently, the mechanical threshold is also. The initial strain hardening rate at 0K,  $\hat{\theta}_0$ , is assumed to be constant with a value of 1/20 of the shear modulus (Estrin, 1996).  $\hat{\sigma}_\infty$  is a parameter with the unit of stress. The activation energies for the initial yield stress and initial strain hardening rate are fitted in dependence on  $c_{\text{eff}}$ . The activation energy for the low temperature saturation stress linearly depends on  $c_\infty = c_0 + c_{\text{eff}}^\infty - c_{\text{eff}}^0$ , where  $c_{\text{eff}}^0 = c_{\text{eff}}(\rho_0)$  and  $c_{\text{eff}}^\infty = c_{\text{eff}}(\rho_\infty)$ . All parameters used in the simulations are summarized in Table 7.

Table 7. Symbols and Values

Symbol	Name	Unit	Value	Source
$\nu$	Poisson's ratio	(-)	0.347	(Hirth and Lothe, 1991)
$G$	Shear modulus	(MPa)	29438.4-15.052T	(Galindo-Nava et al., 2012)(Mecking et al., 1986)
$b$	Burgers vector	(m)	$2.86 \cdot 10^{-10}$	(Frost and Ashby, 1982)
$M$	Taylor factor	(-)	3.06	(Bergström, 1983)(Kato, 1999)
$\alpha$	Strengthening coefficient	(-)	0.34	(Sauzay and Kubin, 2011)(Madec et al.,

$c$	Speed of sound	(m/s)	5100	2002)(Schoeck and Frydman, 1972)
$Q_{vac}$	Activation energy for vacancy formation	(eV)	0.67	(Lide, 2008)
$Q_v$	Activation energy for lattice diffusion	(J/mol)	$127.2 \cdot 10^3$	(Tzanetakis et al., 1976)
$D_{v0}$	Pre-exponential factor for lattice diffusion	(m <sup>2</sup> /s)	$1.4 \cdot 10^{-5}$	(Campbell and Rukhin, 2011)
$Q_d$	Activation energy for pipe diffusion	(J/mol)	$83.2 \cdot 10^3$	(Campbell and Rukhin, 2011)
$D_{d0}$	Pre-exponential factor for pipe diffusion	(m <sup>2</sup> /s)	$1.5 \cdot 10^{-6}$	(Stechauner and Kozeschnik, 2014)
$\Delta W$	binding energy difference between tension and compression site Al-Mg	(eV)	0.13	(Stechauner and Kozeschnik, 2014)
$\Delta H_c$	activation enthalpy for transitions from tension to compression site Al-Mg	(eV)	0.87	(Curtin et al., 2006)
$n$	exponent in Eq.(77)	(-)	1/3	(Curtin et al., 2006)
$\nu_0$	attempt frequency	(s <sup>-1</sup> )	$3.8 \cdot 10^{13}$	(Soare and Curtin, 2008)
$\varepsilon_m$	misfit-strain for Mg	(-)	0.0123	(Fujikawa and Hirano, 1977)
$\hat{\sigma}_b$	basic yield strength	(MPa)	40	(Uesugi and Higashi, 2013)
$\rho_{eq}$	equilibrium dislocation density	(m/m <sup>3</sup> )	$1 \cdot 10^{11}$	(Sherby et al., 1951)
$\hat{\theta}_0$	strain-hardening rate at 0K	(MPa)	$G/20$	this work
$\hat{\sigma}_\infty$	high temperature saturation stress	(MPa)	30	(Estrin, 1996)
$\Delta F_{\sigma_0}^{lt}$	low temperature activation energy for yield stress	(J)	$(0.25 + 0.4 \cdot c_{eff}^{1/3}) \cdot Gb^3$	this work
$\Delta F_{\sigma_0}^{ht}$	high temperature activation energy for yield stress	(J/mol)	$Q_v + 3.5 \cdot 10^5 \cdot c_{eff}$	(Frost and Ashby, 1982)
$\Delta F_{\theta_0}^{lt}$	low temperature activation energy for strain hardening rate	(eV)	$0.29 + 29.4 \cdot c_{eff}$	this work
$\Delta F_{\theta_0}^{ht}$	high temperature activation energy for strain hardening rate	(J/mol)	$Q_v + 1.27 \cdot 10^5 \cdot c_{eff}$	this work
$\Delta F_{\sigma_\infty}^{lt}$	low temperature activation energy for saturation stress	(J)	$(0.17 + 8.525 \cdot c_{eff}) \cdot Gb^3$	this work
$\Delta F_{\sigma_\infty}^{ht}$	high temperature activation energy for saturation stress	(J/mol)	$Q_d$	(Stechauner and Kozeschnik, 2014)

From the expressions given in Table 6, stress-strain curves are calculated based on the modelling framework as introduced in section 4. For the sake of better understanding, the modelling steps are summarized here. The values of  $A$ ,  $B$  and  $C$  are calculated according to

$$A = \frac{g_1 M}{2b\theta_0}, \quad (78)$$

$$B = \frac{b\theta_0}{\sigma_\infty^{lt} d_{crit} M}, \quad (79)$$

$$C = \frac{2b\theta_0}{g_1M}, \quad (80)$$

where Eqs. (78) and (79) are identical to Eqs. (64) and (66). Eq. (80) follows from the assumption on  $\sigma_\infty^{\text{ht}}$  as given in Table 5 and Eq. (67). The dislocation density evolution as function of temperature, strain rate and material state is calculated with the  $A$ ,  $B$  and  $C$  as calculated with Eqs. (78)-(80) and according to

$$\frac{d\rho}{d\varepsilon} = \frac{M}{bA} \sqrt{\rho} - \frac{2BMd_{\text{crit}}}{b} \rho - 2CD_d \frac{Gb^3}{\dot{\varepsilon}kT} (\rho^2 - \rho_{\text{eq}}^2). \quad (81)$$

The resulting plastic stress is calculated according to the Taylor equation Eq. (11) as

$$\sigma_p = \alpha M G b \sqrt{\rho}. \quad (82)$$

Finally, the stress,  $\sigma$ , is calculated according to Eq. (26)

$$\sigma = \sigma_0 + \sigma_p, \quad (83)$$

where  $\sigma_0$  is modelled according to the expressions given in Table 5 and the calibration given in Table 6.

## **7 Results**

In this section, the experimental data and simulation results are presented, where, first, the experimental data on AA6061, simulations on precipitates and stage IV reported and, subsequently, the modelling results on solid solutions are described.

### **7.1 AA6061**

#### **7.1.1 Experimental data**

Fig. 24 summarizes the experimental stress strain curves as observed after the thermo-mechanical treatment described in section 5.2.

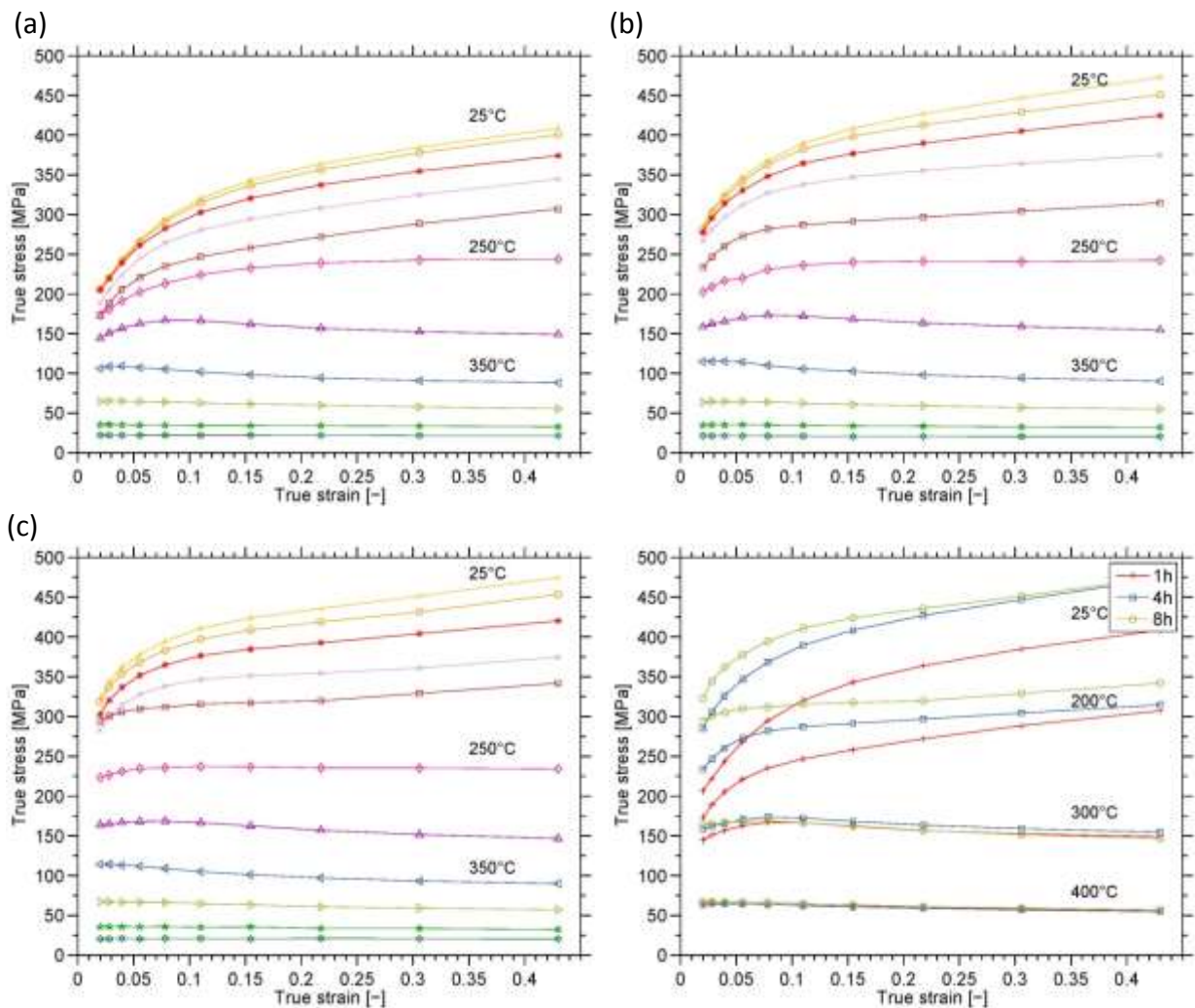


Fig. 24 Stress strain curves for 25, 50 100, 150, 200, 250, 300, 350, 400, 450 and 500°C, after (a) 1h, (b) 4h, and (c) 8h artificial ageing at 170°C. (d) shows selected true stress over true strain curves for 1, 4 and 8h and 25, 200, 300, 400°C.

Fig. 24 shows plots of true stress vs. true strain for all artificial ageing times and temperatures. From room temperature up to roughly 200°C, stage III hardening is observed in the beginning, followed by stage IV hardening with a constant strain hardening rate. With increasing temperature, the degree of strain hardening decreases in both stages. Up to 250°C, the stress is continuously increasing during deformation, i.e. the strain hardening rate is positive throughout the whole deformation process. At 250°C the strain hardening rate in stage IV becomes zero, i.e.  $\theta_{IV} = d\sigma_{IV}/d\varepsilon = 0$ . In the temperature range between 250°C and 400°C, an initial region of strain hardening is followed by a region of softening during deformation. At temperatures above 400°C, no conceivable strain hardening occurs and stress saturation is reached almost immediately after deformation start.

Fig 24 (d) displays selected stress-strain curves for the same test temperatures but different precipitation states, i.e., aging times. At temperatures below 300°C, the initial yield stress as well as the strain hardening behaviour are significantly different for different ageing times. At 300°C, only a weak difference in yield stress and strain hardening rate between different precipitations states is observed at deformation start and deformation at 400°C renders identical stress strain curves. Fig. 25 shows the values of initial yield stress,  $\sigma_0$ , initial strain hardening rate,  $\theta_0$ , stage III saturation stress,  $\sigma_\infty$ , and strain hardening rate in stage IV,  $\theta_{IV}$ .

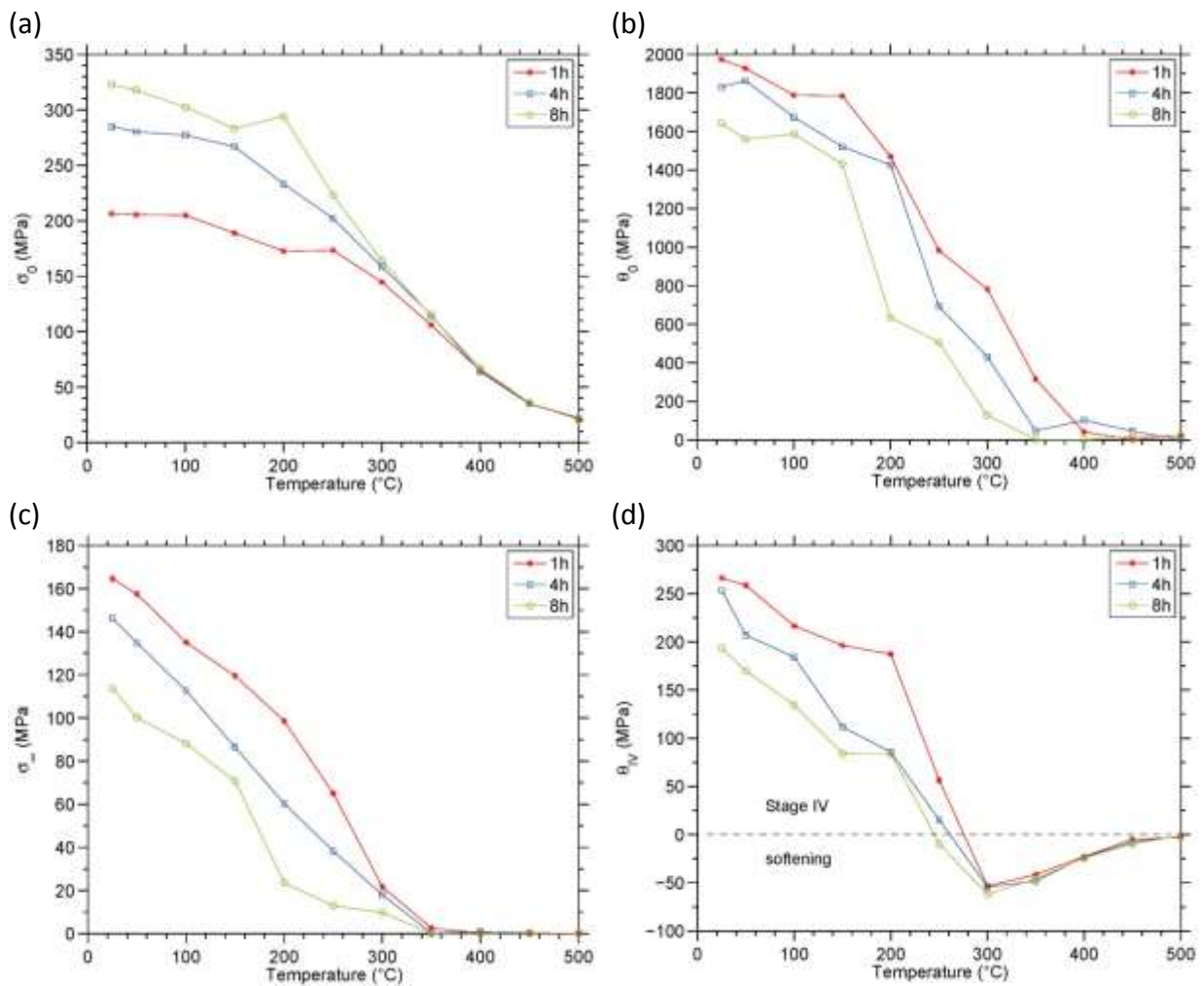


Fig. 25 (a) yield stress, (b) initial strain hardening rate, (c) saturation stress and (d) strain hardening rate in stage IV for 1, 4 and 8h of artificial ageing at 170°C over temperature.

As expected, the initial yield stress,  $\sigma_0$ , is increasing with increasing ageing time due to the increasing contribution of precipitation strengthening. At the same time,  $\theta_0$  and  $\sigma_\infty$  are decreasing with increasing ageing time. Consequently, the presence of precipitates leads to higher initial yield stress values but reduces the materials capacity for strain hardening. Fig.

25 (d) shows the evolution of  $\theta_{IV}$  over temperature. Up to temperatures of roughly 250°C, clear evidence of stage IV hardening is observed (compare Fig. 24), the magnitude of the hardening coefficient, however, is quickly decreasing with increasing temperatures. Just as for stage III hardening, the stage IV strain hardening potential decreases with increasing precipitation strengthening. At roughly 250°C,  $\theta_{IV}$  becomes zero and the stress-strain curve saturates after the end of stage III. At even higher temperatures,  $\theta_{IV}$  is negative and must be interpreted as measure of softening due to precipitate dissolution rather than conventional strain hardening.

Fig. 26 shows values for  $\sigma_0$ ,  $\theta_0$  and  $\sigma_\infty$  normalized with the corresponding values at room temperature. Most interestingly, the evolution over temperature shows a similar ‘s’ shape for all three quantities with almost identical slope, where only the point of inflection is shifted to lower temperature from  $\sigma_0$  over  $\theta_0$  to  $\sigma_\infty$ .

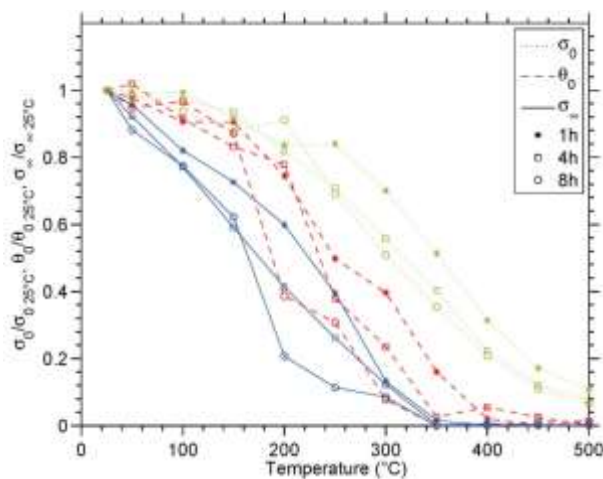


Fig. 26 Yield stress, initial strain hardening rate and saturation stress normalized by room temperature values.

Fig. 27 shows EBSD micrographs as derived according to the preparation procedure described in section 5.2. Fig. 27 (a)-(c) shows a geometrically ordered microstructure, which is typically observed after deformation at lower temperatures (Sparber, 2016), (Hurley and Humphreys, 2003), (Hansen and Jensen, 1999), (Hansen and Huang, 1998), (Liu et al., 1998). At elevated temperatures, non-conservative motion of dislocations, e.g., vacancy-assisted dislocation climb, becomes the predominant mechanism determining the stress-strain behaviour. The enhanced mobility of dislocations at elevated temperature results in a characteristic microstructure, dominated by randomly oriented subgrains, Fig. 27 (d) and (e),

which is commonly associated with lower levels of yield stress and strain hardening. At even higher temperatures, a mixture of grains structured with subgrains and recrystallized grains is observed, Fig. 27 (f). Two regions of different deformation microstructures are consequently found in experimentally determined stress strain curves: One with high yield stress and high strain hardening rate due to thermally activated cross-slip and another one dominated by vacancy assisted climb with lower yield stress and reduced strain hardening rate. The shift between the two mechanisms is expected to occur between 200 and 350°C.

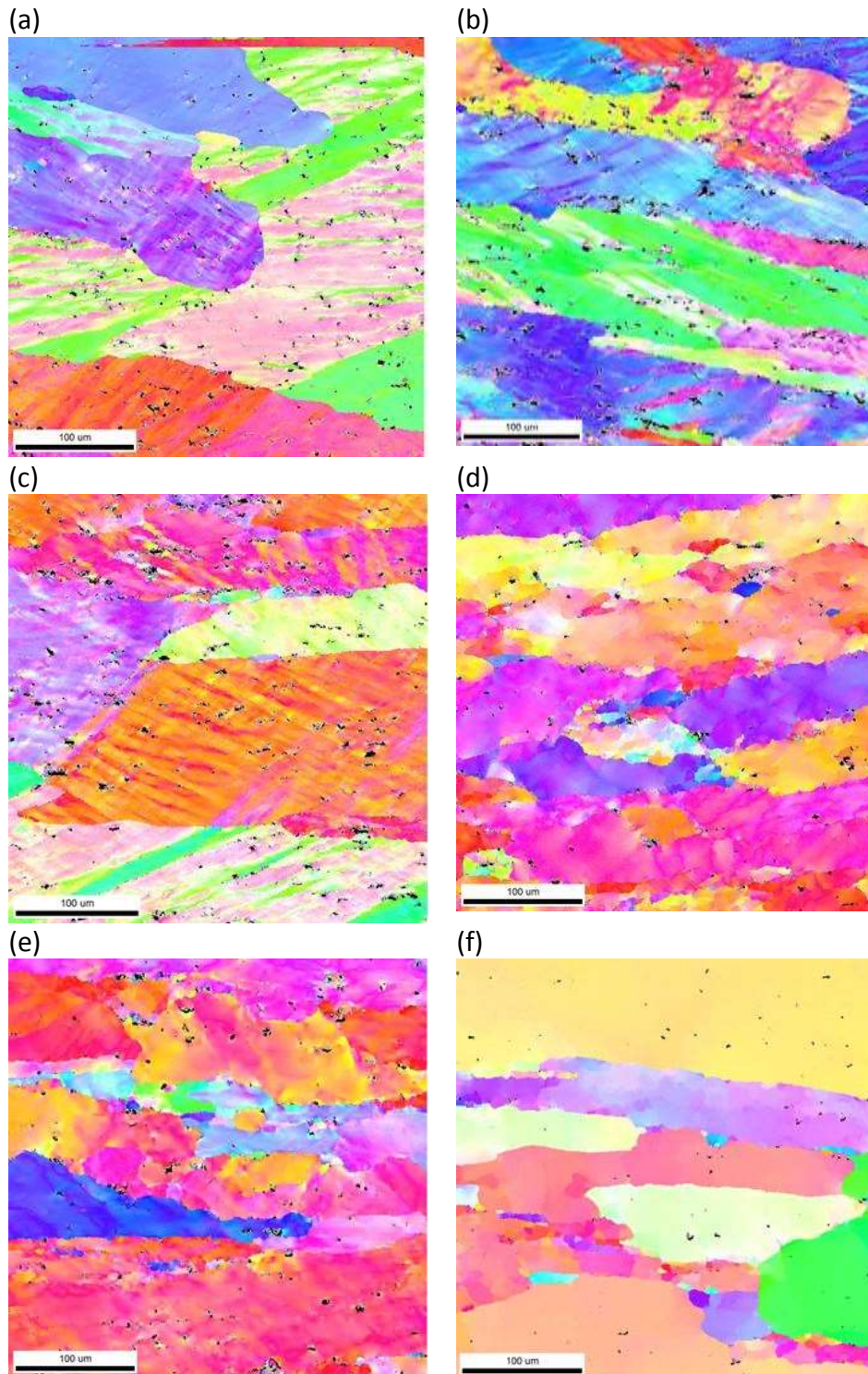
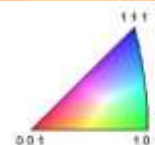


Fig. 27 EBSD Micrographs of A6061 artificially aged for 4h hours and tested at (a) 25, (b) 150, (c) 200, (d) 350, (e) 400 and (f) 450°C at a strain of 0.2



### 7.1.2 Simulation

Fig. 28 shows simulation results for the precipitation sequence, as modelled for the artificial ageing at 170°C, and a pre-treatment as described in section 6.1.

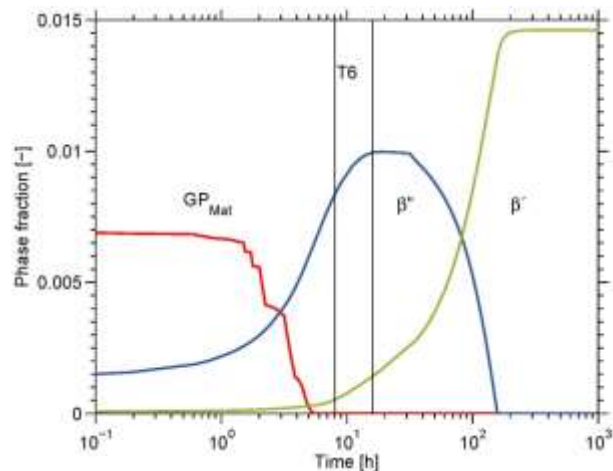


Fig. 28 Precipitation sequence of Mg-Si precipitates after quenching from solution annealing temperature to room temperature with  $900 \text{ Ks}^{-1}$ , heating with  $3 \text{ Ks}^{-1}$  and isothermal holding at  $170^\circ\text{C}$  for the phases GP-Mat,  $\beta''$  and  $\beta'$ . Also shown is the T6 region according to DIN EN 2700.

Fig. 28 also shows the T6 material state, which represents the standard heat treatment for peak strengthening of Al alloys, corresponds to a condition with close-to-maximum phase fraction of  $\beta''$ . It is important to note, that Fig. 28 is only valid for an isothermal heat treatment carried out at  $170^\circ\text{C}$  after solution annealing, quenching and reheating with the rates given in the caption of Fig. 40.

Fig. 29 shows the phase fraction evolution of  $\beta''$  during isothermal heat-treatment at different temperatures and over (a) 70 seconds, where 70 seconds corresponds to deformation test conditions up to a strain of 0.7 with a strain rate of 0.01 and (b) 1000h. The precipitate evolution in Fig. 29 (b) is shown to demonstrate the long-term evolution of precipitates when approaching equilibrium conditions and even longer testing duration. The initial precipitation state / phase fraction of  $\beta''$  is taken from Fig. 28 after isothermal heat-treatment at  $170^\circ\text{C}$  for four hours.

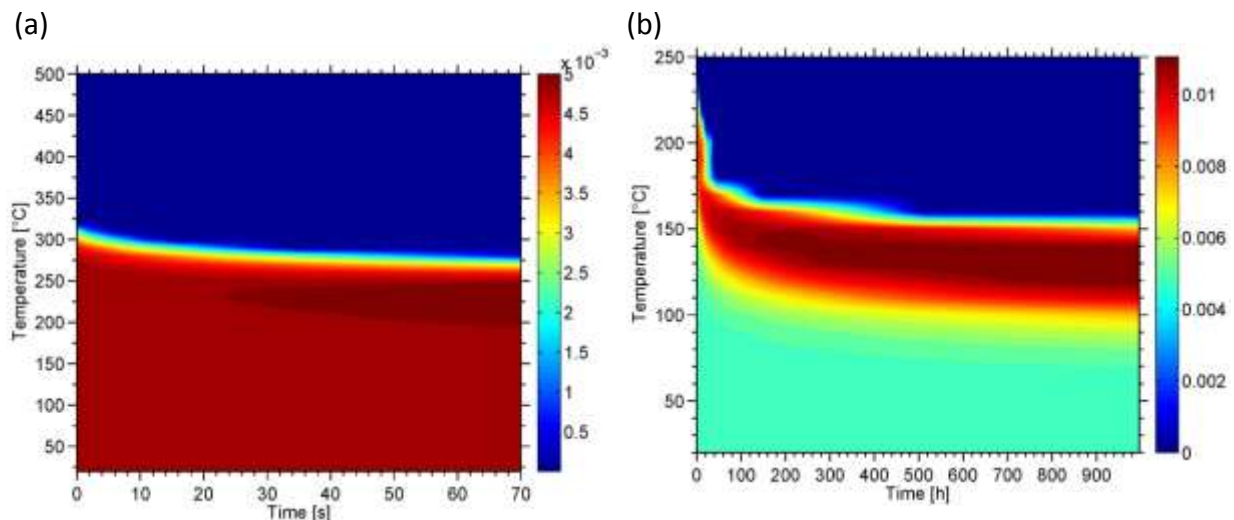


Fig. 29 Dissolution of  $\beta''$  precipitates during iso-thermal heat treatment for (a) 70 s and (b) 1000h, with the phase-fractions given by the color coding.

Fig. 29 (a) shows three distinct regions: (i) from room temperature up to approximately 250°C, the phase fraction of  $\beta''$  is stable or even slightly increasing, (ii) between 250°C-300°C,  $\beta''$  dissolves within the first 70 seconds and (iii) above 300°C precipitates are dissolved within the first instances of heat treatment. Especially interesting is the region between 250 and 300°C where, in the beginning of mechanical testing, precipitates act as obstacles, but they are dissolved during deformation. An initial strain hardening with a subsequent softening is, consequently, expected for stress strain curves in this region, which is in good accordance with Fig. 24. Fig. 29 (b) shows that, for temperatures higher than 170°C, and for testing with rather slow strain rates and long testing duration,  $\beta''$  is dissolved within approximately the first 100h. The simulations also show that any  $\beta''$  precipitation is rapidly dissolved at temperatures higher than 300°C, continuously dissolved between 250 and 300°C, growing at temperatures lower than 250°C and unchanged for temperatures lower than 100°C.

The main strength contribution in age hardenable alloys comes from precipitation. These hardening phases are stable at room temperature but lose their stability with increasing temperature and dissolve completely above a certain threshold (precipitate solvus). In our experiments, no difference in yield stress between different artificial ageing times is observed for high temperature tests since the precipitates formed in the artificial aging treatment dissolve rapidly in the beginning of the test. At intermediate temperatures, the dissolution process takes place simultaneously to deformation. In this region, we observe a clear softening in the stress-strain curve (Fig. 24 (a), (b), (c) curves for 300°C), which is

attributable to the precipitate dissolution mechanism. Interestingly, dynamic recrystallization can be excluded as mechanism responsible for this softening, since recrystallization does not occur until temperatures above 400°C (Fig. 39). A comparison with the simulated precipitation state shown in Fig. 29 indicates that the reduction in strength coincides with the region of  $\beta''$  dissolution, which apparently commences in the course of compression testing and continues to a higher degree with increasing test temperature. This dissolution is accompanied by a loss in precipitation strengthening and, thus, an integral softening in the stress-strain curve.

Fig. 30 (a) shows the simulation results for the KM model extended for stage IV hardening according to the parameters given in section 6.1.3. (b) shows the corresponding dislocation density evolution. It is observed that the experimental data is very well reproduced.

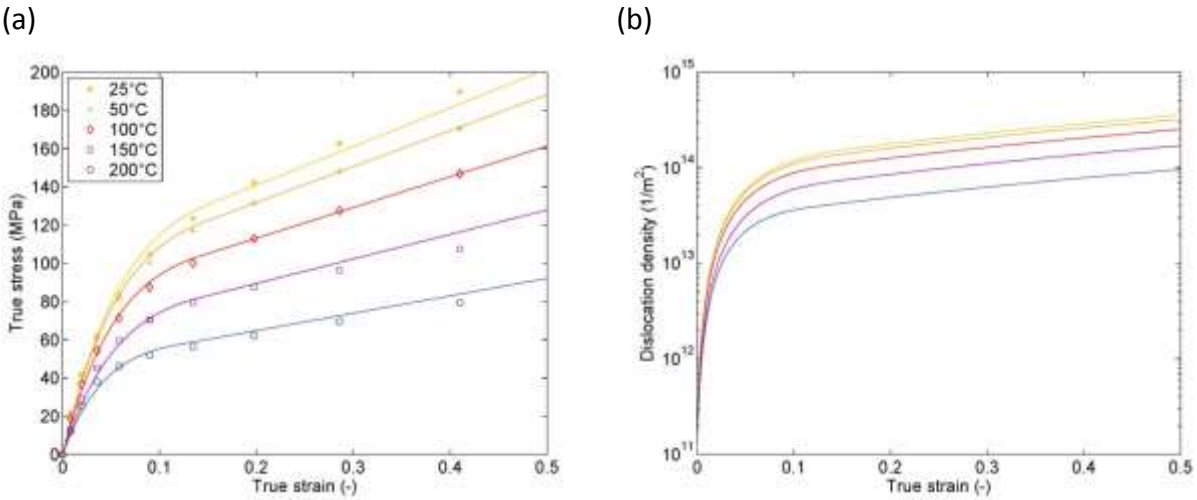


Fig. 30 (a) Experimental (symbols) and simulated (lines)  $\sigma_p$  vs.  $\epsilon$  curves for five different temperatures (b) corresponding simulated dislocation density evolution.

## 7.2 Solid solutions

Fig. 31 shows a plot of the (a) initial yield stress, (b) initial strain hardening rate and (c) saturation stress normalized with the temperature-dependent shear modulus as a function of temperature and solute content as derived according to the data preparation described in section 5.3 and stress strain curve data from (Sherby et al., 1951). Fig. 31 (d) shows the values for  $\sigma_0$ ,  $\theta_0$  and  $\sigma_\infty$  in Al-Mg solid solution for different solute contents and normalized with the corresponding values at 3.2 at.% Mg.

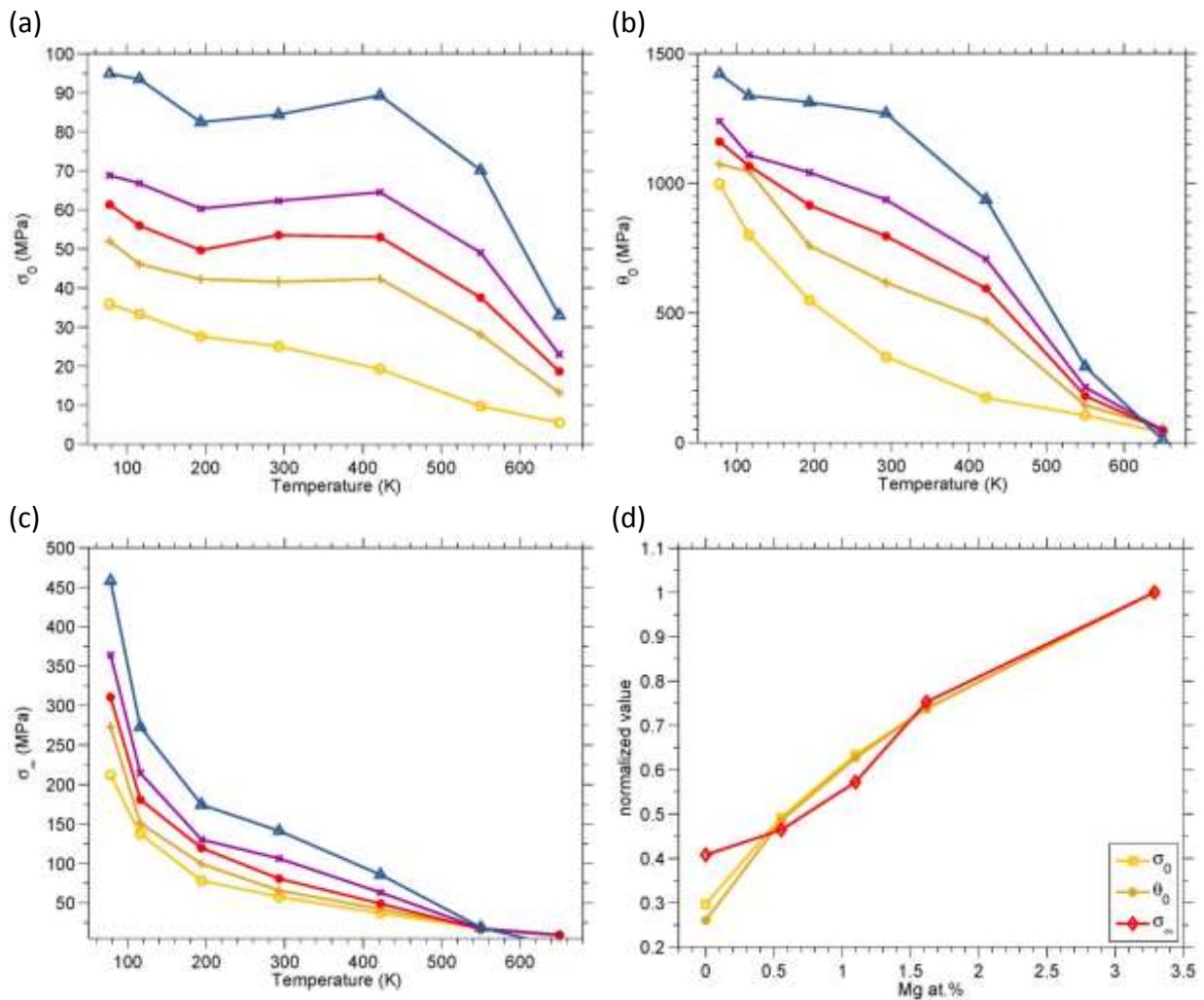


Fig. 31 (a) Initial yield stress (b) Initial strain hardening rate and (c) saturation stress as a function of temperature and solute content.  $\Delta$  3.2 at.% Mg,  $\times$  1.6 at.% Mg,  $*$  1.1 at.% Mg,  $+$  0.6 at.% Mg and pure Al. (d) normalized values for initial yield stress, initial strain hardening rate and saturation stress as a function of Mg content at room temperature, a strain rate of  $2 \times 10^{-3} \text{ s}^{-1}$  and normalized with the value at 3.2 at.% Mg. Data from (Sherby et al., 1951).

A general tendency for lower stress values with increasing temperature is observed. This tendency is interrupted at medium temperature in the region, where dynamic strain ageing (DSA) occurs. The impact of DSA is most pronounced for  $\sigma_0$  and  $\theta_0$ . In general, solid solution hardening leads to an increase of the initial yield stress and at the same time leads to an increase in strain hardening potential. Most interestingly, the dependence of  $\sigma_0$ ,  $\theta_0$  and  $\sigma_\infty$  on the solute content is very similar when normalized, Fig. 31 (d).

Fig 32 (a) compares the results of the present model on  $\sigma_0$  with the data depicted in Fig. 32 (a). All curves are calculated with the parameters listed in Table 7 and no additional modification or fitting is applied. For the sake of better interpretation, Fig. 32 (a) also shows simulation results where  $c_0$  instead of  $c_{\text{eff}}$  is used for the calculations (dashed lines) not taking into account dynamic strain ageing. Fig. 32 (b) displays the strain rate sensitivity (SRS) given by  $m_{\text{SRS}} = d \ln \sigma / d \ln \dot{\epsilon}$  as a function of temperature.

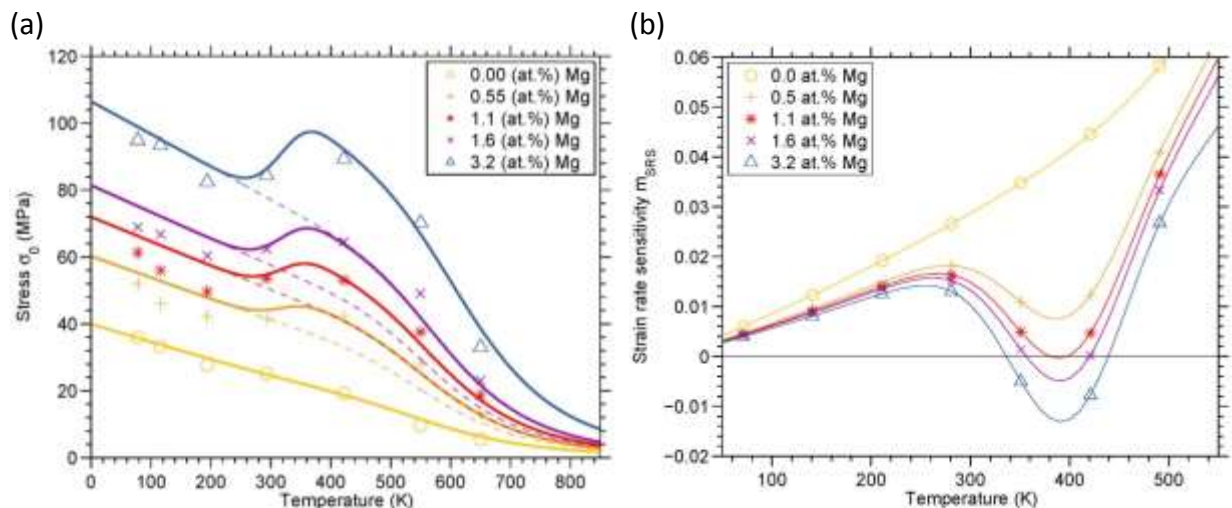


Fig. 32 (a) Comparison of experimental (symbols) and simulated stresses at a strain rate of  $2 \cdot 10^{-3} \text{ s}^{-1}$  and using either  $c_{\text{eff}}$  (solid lines) or  $c_0$  (dashed lines) in Eq. (3), the latter replacing  $c_{\text{eff}}$ . (b) Strain rate sensitivity as a function of solute content and temperature.

According to the mechanical threshold concept, the SRS is zero at zero Kelvin. The SRS increases monotonically up to a certain point where considerable dynamic strain ageing sets in. All Mg-containing alloys considered in this work exhibit a local maximum at around room temperature and a subsequent local minimum at roughly 400 K. Interestingly, the minimum is observed for all Mg containing alloys, but negative strain rate sensitivity (nSRS) is observed only above a characteristic Mg level. In the alloys showing nSRS at a given strain rate, the regions of nSRS are delimited by two characteristic points of zero SRS.

An overview of SRS over a larger temperature and strain rate range is shown in Fig. 33, where the strain rate sensitivity is displayed in a gray scale contour plot over strain rate and temperature. The bold lines indicate the loci of zero strain rate sensitivity with a field of negative strain rate sensitivity enclosed. The plots emphasize that the region with nSRS extends farther with increasing Mg content. Interestingly, at any given deformation temperature, it is possible to find strain rates where the region of nSRS can be avoided. The same applies to any given strain rate, where deformation temperatures exist outside the region of nSRS.

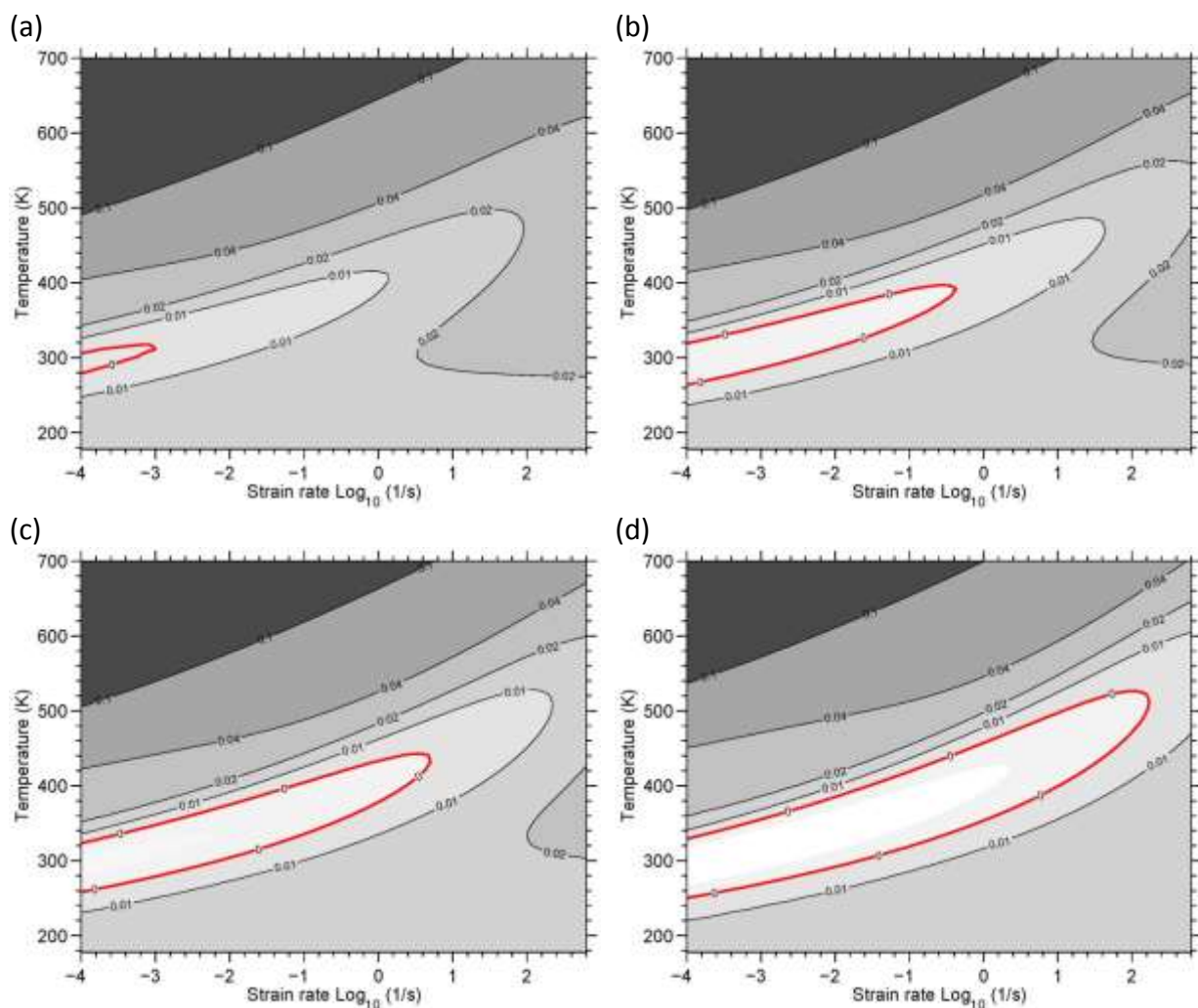


Fig. 33 Strain rate sensitivity as function of temperature and strain rate for (a) 0.5 (b) 1.1 (c) 1.6 and (d) 3.2 at % Mg. The bold line designates the contour of zero strain rate sensitivity.

Fig. 34 (a) and (b) shows the assessed experimental values (symbols) and the corresponding modelling results (lines) for  $\theta_0$  and  $\sigma_\infty$ . In addition, Fig. 34 (c) and (d) display the values of  $A$  and  $B$  calculated with Eqs. (78)-(80) and the parameterization given in Table 7.

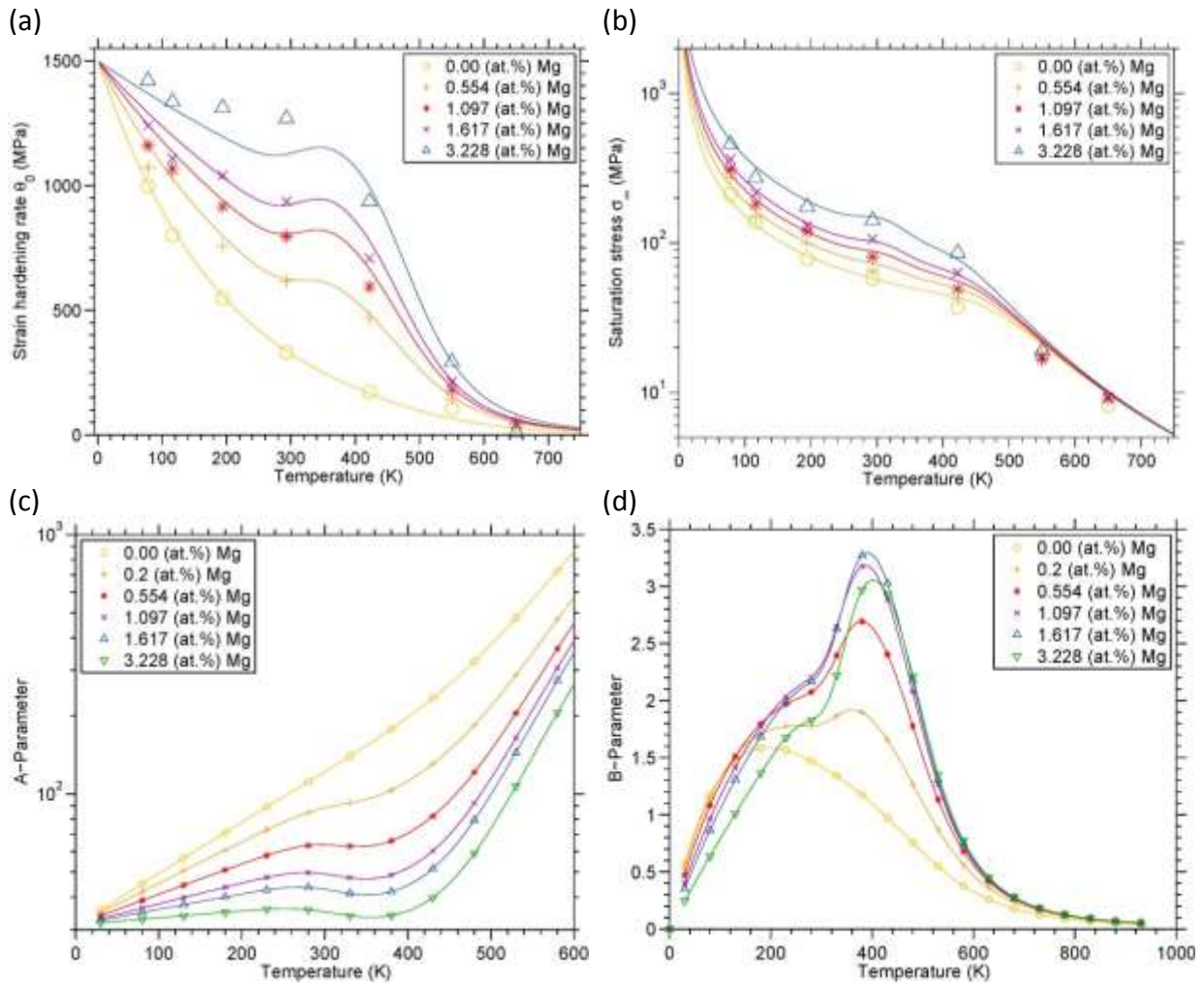


Fig. 34 Comparison between experimental (symbols) and modelled (lines) values for (a) the initial strain hardening rate,  $\theta_0$ , and (b) the saturation stress,  $\sigma_\infty = \sigma - \sigma_0$ . (c) A parameter and (d) B parameter of the extended KM-model over temperature.

The experimentally determined initial strain hardening rate and saturation stress show a tendency for higher values with decreasing temperature and increasing solute content. This applies over the entire temperature range. For both,  $\theta_0$  and  $\sigma_\infty$ , a low and a high temperature regime is observed. The widest spread of values at a particular temperature and varying solute content is observed at intermediate temperatures, where dynamic strain ageing is of major importance. At low temperature, values for the initial strain hardening rate seem to converge at a constant value of  $\hat{\theta}_0 = G/20$ , in accordance with previous findings of (Estrin, 1996). For the saturation stress, no such convergence to a limiting value is observed: in the limit of  $T \rightarrow 0$ ,  $\sigma_\infty \rightarrow \infty$  and  $B \rightarrow 0$ . In other words, the relevance of dynamic

recovery is decreasing with decreasing temperature. In this context, it must be emphasized again that stages IV and V hardening are not considered in the present simulation, which would set a natural limit to this extrapolation.

In the absence of solute atoms, i.e., for pure aluminium, the  $A$ -term is continuously increasing with temperature. For intermediate Mg contents and temperatures, corresponding to the cross-core diffusion region, a nearly constant value of the parameter  $A$  is observed. This is due to the antagonistic effects of thermal activation and dynamic strain ageing. The evolution of the  $B$ -parameter over temperature, Fig. 34 (d), in pure Al is also essentially different to the one in Al-Mg solid solutions. In pure Al, the recovery term  $B$  shows a maximum at around 200K and a subsequent monotonic decrease. The curves for solid solutions show a weak point of inflection around 200K and a pronounced maximum in the region of cross-core diffusion. It should be mentioned, here, that dynamic recovery is often related to thermally activated cross-slip (Püschl, 2002) and that the direct correlation of the  $B$ -term to  $\theta_0$  and  $\sigma_\infty$  offers an elegant means for investigation of the latter.

Fig. 35 (a)-(e) compiles the experimental stress-strain values together with the simulation results based on the present analysis. The accurate reproduction of the complex stress-strain relations including the impact of dynamic strain aging is one of the main achievements of the present work. Fig. 35 (f) shows a close up of Fig. 35 (e) focusing on low strains, where the simulated stress-strain curves for 194K, 293K and 422K clearly intersect in the beginning, in accordance with experiments.

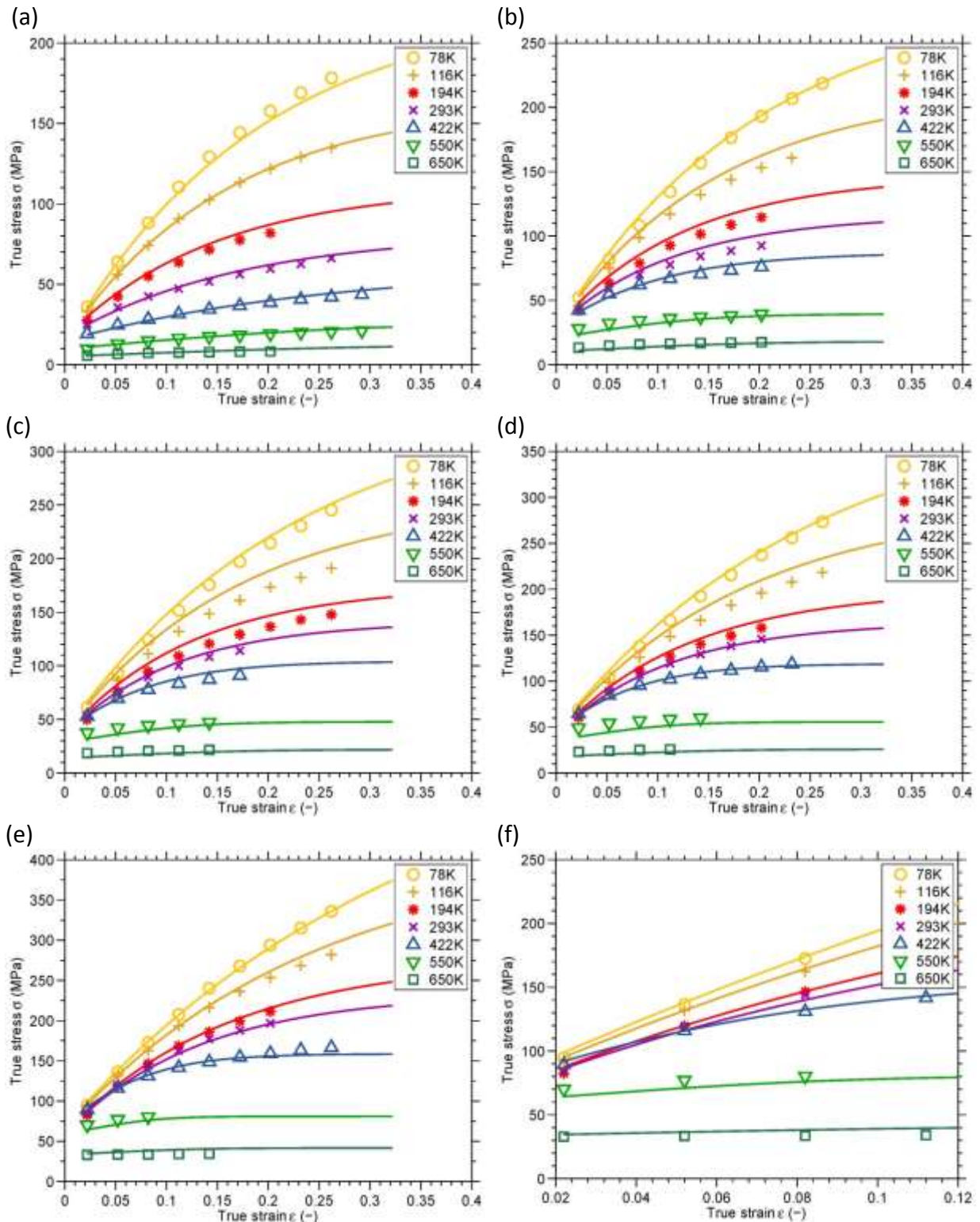


Fig. 35 Comparison between experimental (symbols) and simulated (lines) stress-strain curves for (a) 0.0 at.% Mg, (b) 0.55 at.% Mg, (c) 1.1 at.% Mg, (d) 1.6 at.% Mg, (e) 3.2 at.% Mg at a strain rate of  $0.002 \text{ s}^{-1}$ . (f) is a close-up of (e).

## 8 Discussion

Experimental findings clearly indicate that the initial yield strength,  $\sigma_0$ , the initial strain hardening rate,  $\theta_0$ , and the saturation stress,  $\sigma_\infty$ , depend on temperature, strain rate and material state. The general tendency for the temperature and strain rate-dependence for all three quantities is decreasing values for increasing temperature and decreasing strain rate. However, in some temperature or strain rate ranges, one of the three quantities can be assumed constant, as assumed in some alternative state parameter-based models (Roters et al., 2000), (Galindo-Nava et al., 2012), (Nes, 1997), (Kocks, 1976). Fig. 36 shows two sets of (a) schematic stress-strain curves and (b) corresponding Kocks-plots, where in both cases one characteristic quantity is assumed to be independent of temperature and strain rate.

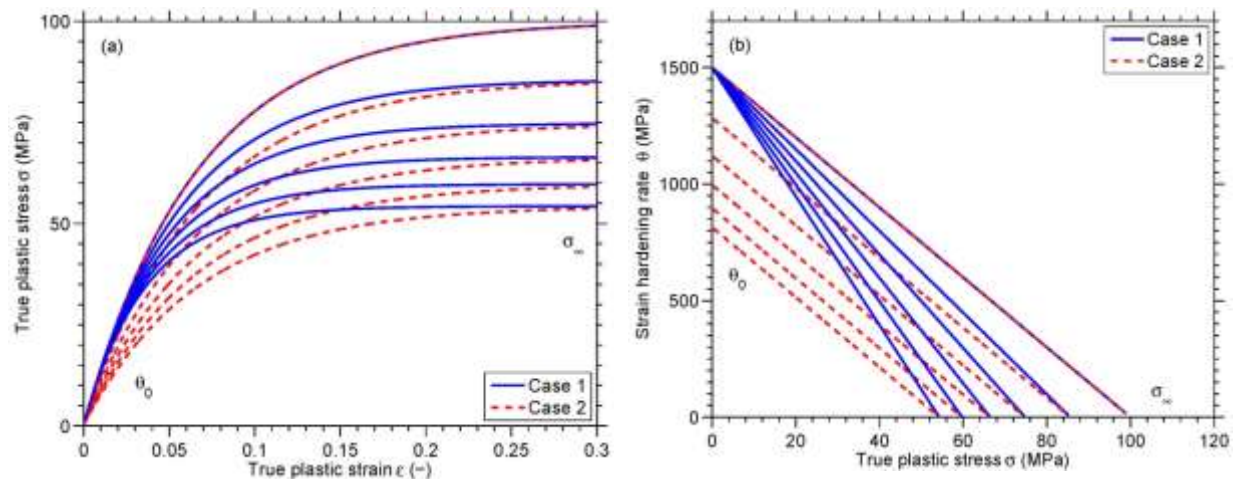


Fig. 36 (a) schematic stress-strain curves with stage III hardening, and (b) corresponding Kocks-plots, generated with the Kocks-Mecking model, according to Case 1 (solid lines) and Case 2 (dashed lines).

In the first case, Case 1 (solid lines), it is the initial strain hardening rate,  $\theta_0$ , in the second case, Case 2 (dashed lines), it is the critical strain,  $\epsilon_c$ , which is an athermal quantity. Comparison with experimental data on  $\theta_0$  and  $\sigma_\infty$  in section 7 shows that both cases are observed in real materials, e.g., Case 1 is observed in an intermediate temperature range for Al-Mg solid solutions where  $\theta_0$  appears to be rather insensitive to changes in temperature. This latter independence of  $\theta_0$  appears to be due to dynamic strain ageing effects – in the

same temperature range  $\sigma_0$  and  $\sigma_\infty$  are rather insensitive to temperature and strain rate – and does not seem to be a general material property, especially not of pure materials. The experimental results on pure Al, Fig. 31, rather show some similarities with Case 2 behaviour. In general, it must be said that both assumptions represent simplifications and, in experiment, all three quantities,  $\sigma_\infty$ ,  $\theta_0$  and  $\sigma_0$ , exhibit some individual dependencies on temperature and strain rate, which are not fully explained on the basis of any first-principles theory. Consequently, the expressions for the temperature and strain rate-dependence of  $\sigma_0 = \sigma_0(T, \dot{\varepsilon}, s_1, s_2, \dots)$ ,  $\theta_0 = \theta_0(T, \dot{\varepsilon}, s_1, s_2, \dots)$  and  $\sigma_\infty = \sigma_\infty(T, \dot{\varepsilon}, s_1, s_2, \dots)$  must have individual character or at least calibration. In Al-Mg, the evolution of  $\sigma_0$  and  $\theta_0$  is very well reproduced by the thermal activation framework outlined in section 4.1. The experimental data on the saturation stress,  $\sigma_\infty$ , was not found to be in accordance with a finite value at 0K (MTS) and could consequently not be reproduced by the same thermal activation framework. However, at low temperatures, a dependence on  $kT/Gb^3 \ln(\dot{\varepsilon}_0/\dot{\varepsilon})$  is observed in all cases and at high temperatures some kind of power-law appears to be suitable for all three quantities. It is also observed that two deformation regimes, one for low and one for high temperature deformation appear to be sufficient for an accurate reproduction of the initial yield stress and the dislocation density evolution. This is in good accordance with some constitutive models, e.g., the Freiburger Ansatz Eqs. (15) and (16), where also two expressions are utilized. Fig. 37 shows the absolute values of the production term  $d\rho^+/d\varepsilon$  in comparison to the absolute values of the dynamic recovery  $d\rho_d^-/d\varepsilon$ , and static recovery term  $d\rho_s^-/d\varepsilon$  at saturation over temperature.

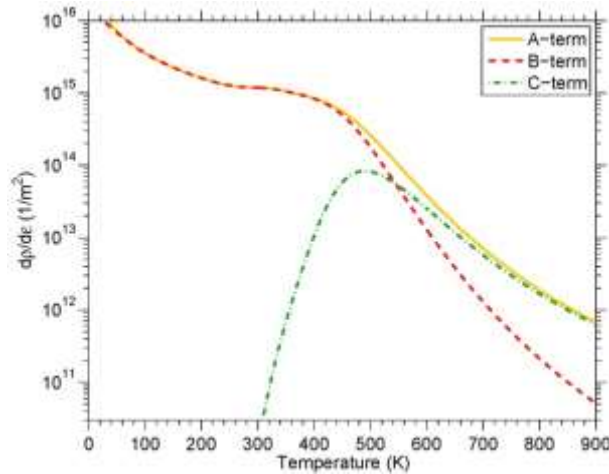


Fig. 37 Comparison between production term (A-term) and dynamic (B-term) static (C-term) recovery term for different temperatures at saturation for 1.1 at.% Mg.

At room temperature, static recovery is of practically no relevance in Al-Mg alloys. Static recovery reaches its peak value around 500K, where dynamic recovery is still the dominant recovery mode. After a short period of similar relevance, static recovery becomes prevalent at roughly 600K up to melting temperature. Consequently, contributions from both, static and dynamic recovery, are essential for a dislocation density evolution model covering the entire temperature range. The EBSD micrographs in section 7.4.1 support this observation by showing a transition in the deformation microstructure from geometrically ordered to vacancy-assisted climb dominated randomly oriented subgrains, which is in good accordance with the results depicted in Fig. 37.

$\sigma_0$ ,  $\theta_0$  and  $\sigma_\infty$  also heavily depend on the material state, e.g., solute atoms lead to an increase of the initial yield strength,  $\sigma_0$ , the initial strain hardening rate,  $\theta_0$ , and the saturation stress,  $\sigma_\infty$ . In the present work, the influence of solute atoms on strain hardening potential is represented by a dependence of the activation energies and the mechanical threshold on an effective solute concentration. Consequently, also the dislocation density evolution is affected by the effect of solute atoms including that of dynamic strain ageing. The dependence of the dislocation density evolution on DSA or even solute atoms is not taken into account in the models on stress strain curve prediction in Al-Mg by (Soare and Curtin, 2008) and (Keralavarma et al., 2014).

It should be mentioned that, generally, the observed increase in strain hardening potential is said to be related to a variation in stacking fault energy with solute content, which is not

taken into account on a strictly physical basis in the present model. According to (Thornton et al., 1962), the stacking fault energy is closely related to the mechanism of cross-slip. (Kocks and Mecking, 2003) pointed out that the strain hardening potential in pure materials scales with the stacking fault energy. (Weertman, 1965) and (Guo et al., 2006) investigated the influence of stacking fault energy on high-temperature creep. The influence of alloying elements and temperature on the stacking fault energy was investigated by (Gallagher, 1970). (Parvin and Kazeminezhad, 2014) presented a model relating the stacking fault energy to the dislocation density. Also, (Estrin, 1996) and (Galindo-Nava et al., 2014), relate strain hardening and atoms in solid solution through the stacking fault energy. These observations could be comprised in a future development of the present model. However, it should be emphasized that the resulting values of  $\sigma_\infty$ ,  $\theta_0$  and  $\sigma_0$  and, consequently, of  $A$ ,  $B$  and  $C$  would have to be the same as in the present work if the calibration is based on the same experimental results.

In the present formulation of the model, the MTS contribution from solute atoms and thus the material state is rendered temperature and strain rate-dependent. Fig. 38 summarizes the MTS contribution from Mg solute atoms as function of temperature and strain rate.

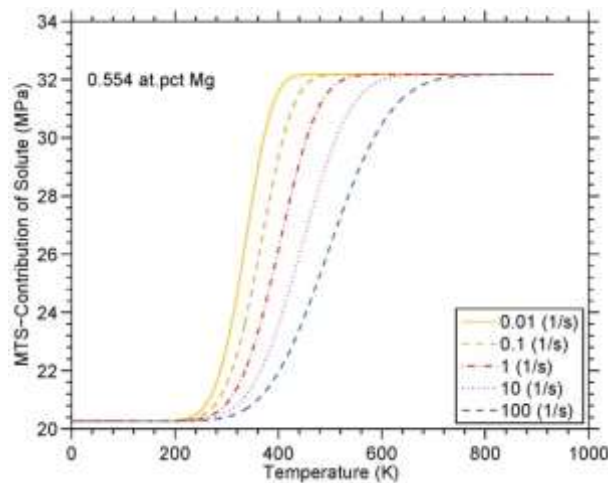


Fig. 38 Solute element contribution to the mechanical threshold from 0.554 at.pct Mg as a function of temperature and strain rate, according to the present model and calibration

A dependence of material state on temperature is also observed in artificially aged AA6061 alloys. Comparison of experiments and simulations clearly indicates that, at intermediate temperatures, hardening phases are metastable and dissolve during plastic deformation.

This leads to initial strain-hardening with subsequent softening, which was observed for all precipitation states. The location and appearance of this maximum in yield stress is additionally dependent on strain-rate. This is a consequence of the diffusive character of the dissolution process. Most interestingly, artificial ageing leads to an increase in initial yield strength,  $\sigma_0$ , but a decrease in hardening potential. Consequently,  $\theta_0$  and the saturation stress  $\sigma_\infty$  are decreasing with increasing initial yield strength. A similar behaviour was observed by (Fribourg et al., 2011) for a 7000 series aluminium alloy. Any model, being either constitutive or physical, would have to reproduce this inverse relation between initial yield strength and hardening potential. It should be mentioned here, that, to the present author's opinion, the combined effects of temperature dependence of material state and temperature and strain-rate dependence due to thermal activation and increased dislocation mobility are often confused in literature, although they are essential for a successful simulation of stress strain curves over a large range of temperatures.

## 9 Summary

A comprehensive model for the simulation of temperature, strain rate and material state dependent stress-strain curves is developed. The total yield stress is calculated as superposition of a strain-independent initial yield stress and a strain-dependent plastic stress. The strain-independent stress contribution is calculated on the basis of the mechanical threshold concept and a thermal activation framework. Strain hardening is calculated on the basis of an extended Kocks-Mecking type model utilizing an average dislocation density as state parameter. As an important feature for practical application, the present model seamlessly extends existing approaches for yield stress modeling based on dislocation glide into the high-temperature deformation region dominated by vacancy-assisted dislocation climb. Experimental data on Al-Mg binary solid solutions and an artificially aged AA6061 aluminum alloy are analyzed in the light of the present model, where precipitation kinetics during artificial aging and the thermal stability of the corresponding material state are simulated with the thermo-kinetic software package MatCalc. It is shown that the present approach consistently represents the yielding behaviour of alloys in a variety of microstructural conditions with respect to the production history of the alloy and the testing conditions, i.e. temperature and strain rate.

## 10 References

- Ahad, F.R., K., E., Solanki, K.N., Bammann, D.J., 2014. Nonlocal modeling in high-velocity impact failure of 6061-T6 aluminum. *Int. J. Plast.* 55, 108–132.
- Ahmadi, M., Rath, M., Povoden-Karadeniz, E., Primig, S., Wojcik, T., Danninger, A., Stockinger, M., Kozeschnik, E., 2017. Modeling of precipitation strengthening in Inconel 718 including non-spherical gamma dp precipitates. *Model. Simul. Mater. Sci. Eng.* 25, 1–16. doi:<https://doi.org/10.1088/1361-651X/aa6f54>
- Ahmadi, M.R., Povoden-Karadeniz, E., Öksüz, K.I., Falahati, A., Kozeschnik, E., 2014. A model for precipitation strengthening in multi-particle systems. *Comput. Mater. Sci.* 91, 173–186. doi:10.1016/j.commatsci.2014.04.025
- Argon, A.S., 1996. Mechanical properties of single phase crystalline media: Deformation at low temperatures, in: Cahn, R., Haasen, P. (Eds.), *Physical Metallurgy III*. pp. 1878–1955.
- Asgari, S., El-Danaf, E., Kalidindi, S.R., Doherty, R.D., 1997. Strain hardening regimes and microstructural evolution during large strain compression of low stacking fault energy fcc alloys that form deformation twins. *Metall. Mater. Trans. A* 28, 1781–1795. doi:10.1007/s11661-997-0109-3
- Austin, R.A., McDowell, D.L., 2011. A dislocation-based constitutive model for viscoplastic deformation of fcc metals at very high strain rates. *Int. J. Plast.* 27, 1–24.
- Baird, J., Gale, B., 1965. Attractive dislocation intersections and work hardening in metals. *Philos Trans Roy Soc* 257, 553–590.
- Barlat, F., Glazov, M. V., Brem, J.C., Lege, D.J., 2002. A simple model for dislocation behavior, strain and strain rate hardening evolution in deforming aluminum alloys. *Int. J. Plast.* 18, 919–939. doi:10.1016/S0749-6419(01)00015-8
- Basinski, S., Basinski, Z., 1979. Plastic deformation and work hardening, in: Nabarro, F. (Ed.), *Dislocations in Solids Vol. 4*. Amsterdam: North-Holland, pp. 261–362.
- Bergström, Y., 1983. The plastic deformation of metals - a dislocation model and its applicability. *Rev. Powder Metall. Phys. Ceram.* 2/3, 79–265.
- Bertin, N., Capolungo, L., Beyerlein, I.J., 2013. Hybrid dislocation dynamics based strain hardening constitutive model. *Int. J. Plast.* 49, 119–144.
- Beyerlein, I.J., Tome, C.N., 2007. A dislocation-based constitutive law for pure Zr including temperature effect. *Int. J. Plast.* 24, 867–895.
- Bolling, G., Richman, R., 1965a. Continual mechanical twinning. *Acta Metall.* 13, 709–722. doi:10.1016/0001-6160(65)90136-7
- Bolling, G., Richman, R.H., 1965b. Continual mechanical twinning. *Acta Metall.* 13, 723–743. doi:10.1016/0001-6160(65)90137-9
- Brinckmann, S., Sivanesapillai, R., Hartmaier, A., 2011. On the formation of vacancies by edge dislocation dipole annihilation in fatigued copper. *Int. J. Fatigue* 33, 1369–1375. doi:10.1016/j.ijfatigue.2011.05.004
- Burgahn, F., Schulze, V., Vöhringer, O., Macherauch, E., 1996. Modellierung des Einflusses von Temperatur und Verformungsgeschwindigkeit auf die Fließspannung von Ck 45 bei Temperaturen  $T < 0,3 T_s$ . *Materwiss. Werksttech.* 27, 521–530.
- Campbell, C.E., Rukhin, A.L., 2011. Evaluation of Self-Diffusion Data Using Weighted Means Statistics. *Acta Mater.* 59, 5194–5201.
- Canova, G., Kocks, U., Jonas, J., 1984. Theory of torsion texture development. *Acta Metall. Mater.* 32, 211–226.
- Christian, J.W., Mahajan, S., 1995. Deformation twinning. *Prog. Mater. Sci.* 39, 1–157. doi:10.1016/0079-6425(94)00007-7
- Coble, R., 1963. A model for boundary diffusion controlled creep in polycrystalline materials. *J. Appl. Phys.* 34, 1679. doi:<http://dx.doi.org/10.1063/1.1702656>
- Csanadi, T., Chinh, N., Gubicza, J., Voeroes, G., Langdon, T., 2014. Characterization of stress-strain relationships in Al over a wide range of testing temperature. *Int. J. Plast.* 54, 176–192.
- Curtin, W.A., Olmsted, D.L., Hector Jr., L.G., 2006. A predictive mechanism for dynamic strain

- ageing in aluminium-magnesium alloy. *Nat. Mater.* 5, 875–880. doi:10.1038/nmat1765
- Dahl, W., Krabiell, A., 1979. Influence of the Temperature and Strain rate on yield strength of various ferritic steels, in: *Strength of Metals and Alloys*. pp. 583–588.
- Deschamps, A., Bréchet, Y., Necker, C.J., Saimoto, S., Embury, J.D., 1996. Study of large strain deformation of dilute solid solutions of Al-Cu using channel-die compression. *Mater. Sci. Eng. A* 207, 143–152. doi:10.1016/0921-5093(95)09992-1
- Diehl, J., 1956. Zugverformung von Kupfer Einkristallen 1. Verfestigungskurven und Oberflächenerscheinungen. *Zeitschrift für Met.* 47, 331–343.
- Diehl, J., Mader, S., Seeger, A., 1955. Gleitmechanismus und Oberflächenerscheinungen bei kubisch flächenzentrierten Metallen. *Zeitschrift für Met.* 46, 650–657.
- Doherty, R.D., Hughes, D.A., Humphreys, F.J., Jonas, J.J., Jensen, D.J., Kassner, M.E., King, W.E., McNelley, T.R., McQueen, H.J., Rollett, A.D., 1997. Current issues in recrystallization: a review. *Mater. Sci. Eng. A* 238, 219–274. doi:10.1016/S0921-5093(97)00424-3
- Duparc, O.H., 2005. Alfred Wilm and the beginnings of Duralumin. *Zeitschrift für Met.* 96, 398–404.
- El-Danaf, E.A., Almajid, A.A., Soliman, M.S., 2008a. Hot deformation of AA6082-T4 aluminum alloy. *J. Mater. Sci.* 43, 6324–6330. doi:10.1007/s10853-008-2895-4
- El-Danaf, E.A., Almajid, A.A., Soliman, M.S., 2008b. High-temperature deformation and ductility of a modified 5083 Al alloy. *J. Mater. Eng. Perform.* 17, 572–579. doi:10.1007/s11665-007-9173-5
- Essmann, U., Mughrabi, H., 1979. Annihilation of dislocations during tensile and cyclic deformation and limits of dislocation densities. *Philos. Mag. A* 40, 731–756.
- Estrin, Y., 1996. Dislocation-Density-Related Constitutive Modeling, in: Krausz, A.S., Krausz, K. (Eds.), *Unified Constitutive Laws of Plastic Deformation*. Academic Press, Inc., New York City, pp. 69–106.
- Estrin, Y., Mecking, H., 1984. A unified phenomenological description of work hardening and creep based on oneparameter models. *Acta Metall. Mater.* 32, 57–70.
- Evans, R.W., Wilshire, B., 1996. Constitutive Laws for High-Temperature creep and creep fracture, in: Krausz, A.S., Krausz, K. (Eds.), *Unified Constitutive Laws of Plastic Deformation*. pp. 107–152.
- Eyring, H., 1936. Viscosity, Plasticity, and Diffusion as Examples of Absolute Reaction Rates. *J. Chem. Phys.* 4, 283–291. doi:10.1063/1.1749836
- Falkinger, G., Simon, P., 2017. Static recovery of an AlMg4.5Mn aluminium alloy during multi-pass hot-rolling, in: *ICTP*.
- Fan, X.G., Yang, H., 2011. Internal-state-variable based self-consistent constitutive modeling for hot working of two-phase titanium alloys coupling microstructure evolution. *Int. J. Plast.* 27, 1833–1852.
- Fischer, F.D., Svoboda, J., Appel, F., Kozeschnik, E., 2011. Modeling of excess vacancy annihilation at different types of sinks. *Acta Mater.* 59, 3463–3472. doi:10.1016/j.actamat.2011.02.020
- Fribourg, G., Brechet, Y., Deschamps, A., Simar, A., 2011. Microstructure-based modelling of isotropic and kinematic strain hardening in a precipitation-hardened aluminium alloy. *Acta Mater.* 59, 3621–3635. doi:10.1016/j.actamat.2011.02.035
- Frost, H., Ashby, M., 1982. *Deformation-mechanism maps*, 1st ed. Pergamon Press, Oxford.
- Fujikawa, S., Hirano, K., 1977. Diffusion of 28Mg in aluminum. *Mater. Sci. Eng.* 27, 25–33.
- Furu, T., Orsund, R., Nes, E., 1995. Subgrain Growth in Heavily Deformed Aluminum-Experimental Investigation and Modeling Treatment. *Acta Metall. Mater.* 43, 2209–2232.
- Galindo-Nava, E.I., Perlade, A., Rivera-Díaz-Del-Castillo, P.E.J., 2014. A thermostatistical theory for solid solution effects in the hot deformation of alloys: an application to low alloy steels. *Model. Simul. Mater. Sci. Eng.* 22, 1–22.
- Galindo-Nava, E.I., Rivera-Díaz-Del-Castillo, P.E.J., 2012. A thermodynamic theory for dislocation cell formation and misorientation in metals. *Acta Mater.* 60, 4370–4378. doi:10.1016/j.actamat.2012.05.003
- Galindo-Nava, E.I., Sietsma, J., Rivera-Díaz-Del-Castillo, P.E.J., 2012. Dislocation annihilation in plastic deformation: II. Kocks-Mecking Analysis. *Acta Mater.* 60, 2615–2624. doi:10.1016/j.actamat.2012.01.028

- Gallagher, P.C. J., 1970. The Influence of Alloying, Temperature, and related effects on the Stacking Fault Energy. *Metall. Trans.* 1, 2429–2461.
- Gao, C.Y., Zhang, L.C., 2012. Constitutive modelling of plasticity of fcc metals under extremely high strain rates. *Int. J. Plast.* 32–33, 121–133.
- Gensamer, M., 1938. The yield point in metals. *Trans. AIME* 128, 104–117.
- Gifkins, R.C., 1976. Grain-boundary sliding and its accommodation during creep and superplasticity. *Metall. Trans. A* 7, 1225–1232. doi:10.1007/BF02656607
- Gil Sevillano, J., van Houtte, P., Aernoudt, E., 1981a. Large strain work hardening and textures. *Prog. Mater. Sci.* 25, 69–412.
- Gil Sevillano, J., van Houtte, P., Aernoudt, E., 1981b. The deformed state of metals (I). work hardening. *Prog. Mater. Sci.* 25, 69–412.
- Guo, Z., Miodownik, A.P., Saunders, N., Schillé, J.P., 2006. Influence of stacking-fault energy on high temperature creep of alpha titanium alloys. *Scr. Mater.* 54, 2175–2178. doi:10.1016/j.scriptamat.2006.02.036
- Haasen, P., 1996. Mechanical properties of solid solutions, in: Cahn, R., Haasen P (Eds.), *Physical Metallurgy III*. pp. 2010–2073.
- Hamasaki, H., Morimitsu, Y., Yoshida, F., 2017. Stress relaxation of AA5182-O aluminum alloy sheet at warm temperature, in: ICTP.
- Hansen, B.I., Beyerlein, I.J., Bronkhorst, C.A., Cerreta, E.K., Dennis-Koller, D., 2013. A dislocation-based multi-rate single crystal plasticity model. *Int. J. Plast.* 44, 129–146.
- Hansen, N., Huang, X., 1998. Microstructure and flow stress of polycrystals and single crystals. *Acta Mater.* 46, 1827–1836. doi:10.1016/S1359-6454(97)00365-0
- Hansen, N., Jensen, D., 1999. Development of Microstructure in FCC Metals during Cold Work Author. *Philos Trans Roy Soc* 357, 1447–1469. doi:DOI: 10.1098/rsta.1999.0384
- Herring, C., 1950. Diffusional viscosity of a polycrystalline solid. *J. Appl. Phys.* 21, 437–445.
- Hirth, J.P., 1972. The influence of grain boundaries on mechanical properties. *Metall. Trans.* 3, 3047–3067. doi:10.1007/BF02661312
- Hirth, J.P., Lothe, J., 1991. *Theory of Dislocations*. Krieger Publishing Company.
- Hollomon, J., 1945. Tensile Deformation. *Trans. AIME* 162, 268–290.
- Holt, D.L., 1970. Dislocation cell formation in metals. *J. Appl. Phys.* 41, 3197–3201. doi:10.1063/1.1659399
- Hu, P., Liu, Y., Zhu, Y., Ying, L., 2016. Crystal plasticity extended models based on thermal mechanism and damage functions: Application to multiscale modeling of aluminum alloy tensile behavior. *Int. J. Plast.* 86, 1–25.
- Hughes, D.A., Nix, W.D., 1989. Strain-Hardening and Substructural Evolution in Ni-Co Solid-Solutions at Large Strains. *Mater. Sci. Eng. a-Structural Mater. Prop. Microstruct. Process.* 122, 153–172. doi:Doi 10.1016/0921-5093(89)90627-8
- Hurley, P.J., Humphreys, F.J., 2003. The application of EBSD to the study of substructural development in a cold rolled single-phase aluminium alloy. *Acta Mater.* 51, 1087–1102. doi:10.1016/S1359-6454(02)00513-X
- Jackson, P., 1985. Dislocation modeling of shear in fcc crystals. *Prog. Mater. Sci.* 29, 139–175. doi:https://doi.org/10.1016/0079-6425(85)90009-X
- Jobba, M., Mishra, R.K., Niewczas, M., 2015. Flow stress and work-hardening behaviour of Al-Mg binary alloys. *Int. J. Plast.* 65, 43–60. doi:10.1016/j.ijplas.2014.08.006
- Johnson, G.R., Cook, W.H., 1983. A constitutive model and data for metal subjected to large strains, high strain rate and temperatures, in: *Proceedings of the Seventh International Symposium on Ballistic*. pp. 541–547.
- Jonas, J.J., 1969. The back stress in high temperature deformation. *Acta Metall.* 17, 397–405. doi:10.1016/0001-6160(69)90020-0
- Kato, M., 1999. *Introduction to the Theory of Dislocations*. Shokabo, Tokyo.
- Keralavarma, S.M., Bower, A.F., Curtin, W.A., 2014. Quantum-to-continuum prediction of ductility loss in aluminium-magnesium alloys due to dynamic strain aging. *Nat. Commun.* 5, 1–8. doi:10.1038/ncomms5604
- Khan, A., Huang, S., 1992. Experimental and theoretical study of mechanical behavior of 1100 aluminum in the strain rate range of 10<sup>-5</sup>-104s<sup>-1</sup>. *Int. J. Plast.* 8, 397–424.
- Khan, A., Liang, R., 1999. Behaviors of three BCC metal over a wide range of strain rates and temperatures: experiments and modeling. *Int. J. Plast.* 15, 1089–1109.
- Khan, A.S., Kazmi, R., Pandey, A., Stoughton, T., 2009. Evolution of subsequent yield surfaces

- and elastic constants with finite plastic deformation. Part-I: A very low work hardening aluminum alloy (Al6061-J6511). *Int. J. Plast.* 25, 1611–1625. doi:10.1016/j.ijplas.2008.07.003
- Khan, A.S., Pandey, A., Stoughton, T., 2010a. Evolution of subsequent yield surfaces and elastic constants with finite plastic deformation. Part II: A very high work hardening aluminum alloy (annealed 1100 Al). *Int. J. Plast.* 26, 1421–1431.
- Khan, A.S., Pandey, A., Stoughton, T., 2010b. Evolution of subsequent yield surfaces and elastic constants with finite plastic deformation. Part III: Yield surface in tension-tension stress space (Al 6061-T6511 and annealed 1100 Al). *Int. J. Plast.* 26, 1432–1441.
- Kocks, U., 1970. The relation between polycrystal deformation and single crystal deformation. *Metall. Trans.* 1, 1121–1143.
- Kocks, U.F., 1998. Solute drag as an upper bound to high temperature strength. *Scr. Mater.* 39, 431–436.
- Kocks, U.F., 1985. Kinetics of solution hardening. *Metall. Trans. A* 16, 2109–2129. doi:10.1007/BF02670415
- Kocks, U.F., 1976. Laws for Work-Hardening and Low-Temperature Creep. *J. Eng. Mater. Technol.* 76–85. doi:doi:10.1115/1.3443340
- Kocks, U.F., Argon, A.S., Ashby, M.F., 1975. *Thermodynamics and Kinetics of Slip*, 1st ed, Progress in Materials Science. Pergamon Press, Oxford. doi:10.1016/0079-6425(75)90009-2
- Kocks, U.F., Chen, S.R., 1993. Constitutive laws for deformation and dynamic recrystallization in cubic metals, in: *Aspects of High Temperature Deformation and Fracture in Crystalline Materials*. pp. 593–600.
- Kocks, U.F., Mecking, H., 2003. Physics and phenomenology of strain hardening: The FCC case. *Prog. Mater. Sci.* 48, 171–273. doi:10.1016/S0079-6425(02)00003-8
- Kozeschnik, E., 2017. MatCalc [WWW Document]. Solid state Precip. Kinet. Simul. Softw. URL <http://matcalc.tuwien.ac.at/> (accessed 10.2.17).
- Kozeschnik, E., Svoboda, J., Fischer, F.D., 2006. Shape factors in modeling of precipitation. *Mater. Sci. Eng. A* 441, 68–72. doi:10.1016/j.msea.2006.08.088
- Kozeschnik, E., Svoboda, J., Fischer, F.D., 2004a. Modified evolution equations for the precipitation kinetics of complex phases in multi-component systems. *Calphad Comput. Coupling Phase Diagrams Thermochem.* 28, 379–382. doi:https://doi.org/10.1016/j.calphad.2004.11.003
- Kozeschnik, E., Svoboda, J., Fischer, F.D., 2004b. Modelling of kinetics in multi-component multi-phase systems with spherical precipitates: II: numerical solution and application. *Mater. Sci. Eng. A* 385, 157–165. doi:https://doi.org/10.1016/j.msea.2004.06.016
- Kreyca, J., Kozeschnik, E., 2017a. Temperature-dependent strain hardening, precipitation and deformation-induced microstructure evolution in AA 6061. *Mater. Sci. Eng. A* 708, 411–418.
- Kreyca, J., Kozeschnik, E., 2017b. Flow stress modelling and microstructure development during deformation of metallic materials. *Mater. Sci. Forum* 892, 44–49.
- Krumphals, F., Sherstnev, P., Mitsche, S., Randjelovic, S., Sommitsch, C., 2009. Physically Based Microstructure Modelling of AA6082 during Hot Extrusion. *Key Eng. Mater.* 424, 27–34. doi:10.4028/www.scientific.net/KEM.424.27
- Kubin, L.P., Estrin, Y., 1990. Evolution of Dislocation densities and the Critical Conditions for the Portevin-le Chatelier Effect. *Acta Metall.* 38, 697–708.
- Labusch, R., 1970. A Statistical Theory of Solid Solution Hardening. *Phys. Status Solidi* 41, 659–669. doi:10.1002/pssb.19700410221
- Lagneborg, R., 1972. A modified Recovery Creep Model and its evaluation. *Met. Sci. J.* 6, 127–133.
- Langford, G., Cohen, M., 1969. Strain hardening of Iron by severe plastic deformation. *Trans. ASM* 62, 623–638.
- Les, P., Stuewe, H., Zehetbauer, M., 1997. Hardening and strain rate sensitivity in stage IV of deformation in fcc and bcc metals. *Mater. Sci. Eng. A* 453–455.
- Leyson, G., Curtin, W., 2016. Thermally activated flow in nominally binary Al-Mg alloys. *Scr. Mater.* 111, 85–88.
- Leyson, G.P.M., Curtin, W. a, Hector, L.G., Woodward, C.F., 2010. Quantitative prediction of solute strengthening in aluminium alloys. *Nat. Mater.* 9, 750–755.

doi:10.1038/nmat2813

- Li, D., Zbib, H., Sun, X., Khaleel, M., 2014. Predicting plastic flow and irradiation hardening or iron single crystal with mechanism-base continuum dislocation dynamics. *Int. J. Plast.* 52, 3–17.
- Li, Y., Nutt, S.R., Farghalli, M.A., 1997. An investigation of creep and substructure formation in 2124 Al. *Acta Mater.* 45, 2607–2620.
- Lide, D.R., 2008. *CRC Handbook of chemistry and Physics*. CRC Press.
- Lifshitz, M., 1963. On the theory of diffusion viscous flow of polycrystalline Bodies. *J. Exp. Theor. Phys.* 17, 909.
- Lindgren, L.E., Domkin, K., Hansson, S., 2008. Dislocations, vacancies and solute diffusion in physical based plasticity model for AISI 316L. *Mech. Mater.* 40, 907–919. doi:10.1016/j.mechmat.2008.05.005
- Liu, J., Tan, M.J., Jarfors, A.E.W., Aue-u-lan, Y., Castagne, S., 2010. Formability in AA5083 and AA6061 alloys for light weight applications. *Mater. Des.* 31, S66–S70. doi:10.1016/j.matdes.2009.10.052
- Liu, Q., Juul Jensen, D., Hansen, N., 1998. Effect of grain orientation on deformation structure in cold-rolled polycrystalline aluminium. *Acta Mater.* 46, 5819–5838. doi:10.1016/S1359-6454(98)00229-8
- Lloyd, J.T., Clayton, J.D., Becker, R., McDowell, D.L., 2014. Simulation of shock wave propagation in single crystal and polygrystalline aluminum. *Int. J. Plast.* 60, 118–144.
- Ludwik, P., 1909. *Elemente der Technologischen Mechanik*. Springer, Berlin.
- Luton, M., Sellars, C., 1969. Dynamic recrystallization in nickel and nickel-iron alloys during high temperature deformation. *Acta Metall.* 17, 1033–1043. doi:10.1016/0001-6160(69)90049-2
- Madec, R., Devincere, B., Kubin, L.P., 2002. From Dislocation Junctions to Forest Hardening. *Phys. Rev. Lett.* 89. doi:10.1103/PhysRevLett.89.255508
- Malin, A.S., Hatherly, M., 1979. Microstructure of cold rolled copper. *Met. Sci.* 463–471.
- Marioara, C., Andersen, S., Zandbergen, H., Holmestad, R., 2005. The influence of alloy composition on precipitates of the Al-Mg-Si System. *Metall. Mater. Trans. A* 36A, 691–702. doi:http://dx.doi.org/10.1007/s11661-005-0185-1
- Marthinsen, K., Nes, E., 2001. Modelling strain hardening and steady state deformation of Al–Mg alloys. *Mater. Sci. Technol.* 17, 376–388. doi:10.1179/026708301101510096
- Matsuda, K., Gamada, H., Fujii, K., Uetani, Y., Sato, T., Kamio, A., Ikeno, S., 1998. High-Resolution Electron Microscopy on the Structure of Guinier–Preston Zones in an Al-1.6 Mass Pct Mg 2 Si Alloy. *Metall. Mater. Trans. A* 29A, 1161–1167. doi:10.1007/s11661-998-0242-7
- McQueen, H., Ryan, N., 2002. Constitutive analysis in hot working. *Mater. Sci. Eng. A* 43–63.
- Mecking, H., Grinberg, A., 1979. Discussion on the development of a stage of steady-state flow at large strains, in: 5th ICSMA, *Int. Conf. on the Strength of Metals and Alloys*. p. 289.
- Mecking, H., Kocks, U.F., 1981. Kinetics of flow and strain hardening. *Acta Metall.* 29, 1865–1875.
- Mecking, H., Kocks, U.F., Hartig, C., 1996. Taylor Factors in Materials With Many Deformation Modes. *Scr. Mater.* 35, 465–471.
- Mecking, H., Nicklas, B., Zarubova, N., 1986. A universal temperature scale for plastic flow. *Acta Metall.* 34, 527–535.
- Mengoni, M., Ponthot, J.P., 2015. A generic anisotropic continuum damage model integration scheme adaptable to both ductile damage and biological damage-like situations. *Int. J. Plast.* 66, 46–70.
- Messerschmidt, U., Bartsch, M., Dieztsch, C., 2006. The flow stress anomaly in Fe-43at%Al single crystals. *Intermetallics* 14, 607–619.
- Mott, N., 1952. A theory of work hardening of metal crystals. *Philos. Mag.* 43, 1151.
- Mughrabi, H., 2016. The alpha factor in the Taylor flow stress law in monotonic, cyclic and quasi stationary deformations: Dependence on slip mode dislocation arrangement and density. *Curr. Opin. solid State Mater. Sci.* 20, 411–420.
- Nabarro, F., Holt, D., Basinski, Z., 1964. Plasticity of pure single crystals. *Adv. Phys.* 13, 193–.
- Nabarro, F.R.N., 1948. Report of a conference on the strength of solids, in: *The Physical Society, London*. pp. 75–90.

- Nes, E., 1997. Modelling of work hardening and stress saturation in FCC metals. *Prog. Mater. Sci.* 41, 129–193. doi:10.1016/S0079-6425(97)00032-7
- Nes, E., 1995. Constitutive laws for steady state deformation of metals, a microstructural model. *Scr. Metall. Mater.* 33, 225–231. doi:10.1016/0956-716X(95)00103-3
- Nes, E., 1994. Recovery Revisited. *Acta Metall.* 43, 2189–2207.
- Nes, E., Furu, T., 1995. Application of Microstructurally based constitutive laws to hot deformation of aluminium alloys. *Scr. Mater.* 33, 87–92.
- Niewczas, M., Jobba, M., Mishra, R.K., 2015. Thermally activated flow of dislocations in Al-Mg binary alloys. *Acta Mater.* 83, 372–382. doi:10.1016/j.actamat.2014.09.056
- Ninive, P., Strandlie, A., Gulbrandsen-Dahl, S., Lefebvre, W., Marioara, C., Andersen, S., Friis, J., Holmestad, R., 2014. Detailed atomistic insight into the beta dp phase in Al-Mg-Si alloys. *Acta Mater.* 69, 126–134. doi:https://doi.org/10.1016/j.actamat.2014.01.052
- Nix, W.D., Gibeling, J.C., Hughes, D.A., 1985. Time dependent deformation of metals. *Metall. Trans. A* 16, 2215–2226.
- Open database license [WWW Document], n.d. . ODbL. URL <https://opendatacommons.org/licenses/odbl/1.0/> (accessed 10.2.17).
- Orowan, E., 1940. Problems of plastic gliding. *Proc. Phys. Soc.* 52, 8. doi:10.1088/0959-5309/52/1/303
- Pandey, A., Khan, A.S., Kim, E.Y., Choi, S.H., Gnaeupl-Herold, T., 2013. Experimental and numerical investigations of yield surface, texture and deformation mechanisms in AA5754 over low to high temperatures and strain rates. *Int. J. Plast.* 41, 165–188.
- Pantleon, W., 2005. Disorientations in dislocation structures. *Mater. Sci. Eng. A* 400–401, 118–124.
- Parvin, H., Kazeminezhad, M., 2014. Development a dislocation density based model considering the effect of stacking fault energy: Severe plastic deformation. *Comput. Mater. Sci.* 95, 250–255. doi:10.1016/j.commatsci.2014.07.027
- Podkuiko, V., Pustovalov, V., Roitman, L., Startsev, V., 1972. Critical shear stress temperature dependence in Al-Mg single crystal alloys of various concentrations in the range of 1.6–300K. *Strength Mater.* 4, 963–967.
- Povoden-Karadeniz, E., 2017a. MatCalc Thermodynamic Database [WWW Document]. “mc\_al.tdb.” URL <http://matcalc.tuwien.ac.at/index.php/databases/open-databases> (accessed 10.2.17).
- Povoden-Karadeniz, E., 2017b. MatCalc Diffusion Database [WWW Document]. “mc\_al.ddb.” URL <http://matcalc.tuwien.ac.at/index.php/databases/open-databases> (accessed 10.2.17).
- Prinz, F.B., Argon, A.S., 1984. The evolution of plastic resistance in large strain plastic flow of single phase subgrain forming metals. *Acta Metall.* 32, 1021–1028. doi:10.1016/0001-6160(84)90004-X
- Püschl, W., 2002. Models for dislocation cross-slip in close-packed crystal structures: A critical review. *Prog. Mater. Sci.* 47, 415–461. doi:10.1016/S0079-6425(01)00003-2
- Raj, R., Ashby, M.F., 1971. On grain boundary sliding and diffusional creep. *Metall. Trans.* 2, 1113–1127. doi:10.1007/BF02664244
- Ravi, C., Wolverton, C., 2004. First-principles study of crystal structure and stability of Al-Mg-Si-(Cu) precipitates. *Acta Mater.* 52, 4213–4227. doi:https://doi.org/10.1016/j.actamat.2004.05.037
- Reed, R.P., 1972. Aluminium 2 . A review of deformation properties of high purity aluminium and dilute aluminium alloys. *Cryogenics (Guildf)*. 259–291.
- Rollet, A., 1988. Strain Hardening at Large Strains in Aluminium Alloys.
- Rong, Q., Shi, Z., Sun, X., Li, Y., Yang, Y., Meng, L., Lin, J., 2017. Experimental studies and constitutive modelling of AA6082 in stress-relaxation age forming conditions, in: ICTP.
- Roters, F., Raabe, D., Gottstein, G., 2000. Work hardening in heterogeneous alloys—a microstructural approach based on three internal state variables. *Acta Mater.* 48, 4181–4189. doi:10.1016/S1359-6454(00)00289-5
- Ryen, O., 2003. Work hardening and mechanical anisotropy of aluminium sheets and profiles. Norwegian University of Science and Technology.
- Ryen, Ø., Holmedal, B., Nes, E., Ekstro, H., 2006a. Strengthening Mechanisms in Solid Solution Aluminum Alloys 37, 1999–2006.
- Ryen, Ø., Laukli, H.I., Holmedal, B., Nes, E., 2006b. Large strain work hardening of aluminum

- alloys and the effect of mg in solid solution. *Metall. Mater. Trans. A* 37, 2007–2013. doi:10.1007/s11661-006-0143-6
- Saada, G., 1960. Sur le durcissement du a la recombinaison des jonctions. *Acta Metall.* 8, 841–847.
- Safaei, M., Yoon, J.W., De Waele, W., 2014. Study on the definition of equivalent plastic strain under non-associated flow rule for finite element formulation. *Int. J. Plast.* 58, 219–238.
- Sauzay, M., Kubin, L.P., 2011. Scaling laws for dislocation microstructures in monotonic and cyclic deformation of fcc metals. *Prog. Mater. Sci.* 56, 725–784. doi:10.1016/j.pmatsci.2011.01.006
- Schmidtchen, M., Spittel, M., 2011. Fließkurven für Warm und Kaltumformung, in: *MEFORM 2011 Werkstoffkennwerte Für Die Simulation von Umformprozessen*. pp. 35–64.
- Schoeck, G., 1965. The Activation energy of Dislocation Movement. *Phys. Status Solidi* 8, 499–505.
- Schoeck, G., Frydman, R., 1972. The contribution of the dislocation forest to the flow stress. *Phys. Status Solidi* 53, 661–673.
- Schoeck, G., Seeger, A., 1955. Defects in Crystalline Solids, in: Mott, N. (Ed.), *Report of the Conference on Defects in Crystalline Solids*. The Physical Society, London, p. 340.
- Schulze, V., Vohringer, O., 2000. Influence of alloying elements on the strain rate and temperature dependence of the flow stress of steels. *Metall. Mater. Trans. A* 31, 825–830. doi:10.1007/s11661-000-1002-5
- Seeger, A., 1957. Work hardening of single crystals, in: Fisher, J., Johnston, W., Thompson, R., Vreeland, J.T. (Eds.), *Dislocations and Mechanical Properties of Crystals*. Wiley, New York, p. 243.
- Sellars, C.M., Tegart, W.J., 1966. La relation entre la resistance et la structure dans la deformation a chaud. *Mem. Sci. rev. Met.* LXIII.
- Shan, Z., 2004. Grain Boundary-Mediated Plasticity in Nanocrystalline Nickel. *Science* (80-. ). 305, 654–657. doi:10.1126/science.1098741
- Sherby, O.D., Anderson, R.A., Dorn, J.E., 1951. Effect of Alloying Elements on the Elevated temperature plastic properties of alpha solid solutions of Aluminum. *J. Met.* 3, 643–652.
- Silbermann, C.B., Shutov, A.V., Ihlemann, J., 2014. Modeling the evolution of dislocation populations under non-proportional loading. *Int. J. Plast.* 55, 58–79.
- Soare, M., Curtin, W., 2008. Solute Strengthening of Both Mobile and Forest Dislocations The Origin of Dynamic Strain Aging in fcc Metals. *Acta Mater.* 56, 4046–4061.
- Sommitsch, 1999. Theorie und Modell der mikrostrukturellen entwicklung von Nickel-bais legierungen wahrend des Warmwalzens - Die virtuelle Walzstrasse.
- Sonderegger, B., Kozeschnik, E., 2009a. Generalized nearest-neighbour broken-bond analysis of randomly oriented coherent interfaces in multicomponent fcc and bcc structures. *Metall. Mater. Trans. A* 40, 499–510. doi:DOI: 10.1007/s11661-008-9752-6
- Sonderegger, B., Kozeschnik, E., 2009b. Size dependence of the interfacial energy in the generalized nearest-neighbour broken-bond approach. *Scr. Mater.* 60, 635–638. doi:https://doi.org/10.1016/j.scriptamat.2008.12.025
- Sparber, D., 2016. Dislocation substructure evolution of an Al-6016-T4 alloy during cold deformation.
- Spigarelli, S., Evangelista, E., McQueen, H.J., 2003. Study of hot workability of a heat treated AA6082 aluminum alloy. *Scr. Mater.* 49, 179–183.
- Spittel, M., Spittel, T., 2009. Landolt-Börnstein Group VIII.
- Staker, M., Holt, D., 1972. The Dislocation Cell Size and Dislocation Density in Copper Deformed at Temperatures Between 25 and 700 C. *Acta Mater.* 20, 569–579.
- Stechauner, G., Kozeschnik, E., 2014. Assessment of substitutional self-diffusion along short-circuit paths in Al, Fe and Ni. *Calphad Comput. Coupling Phase Diagrams Thermochem.* 47, 92–99.
- Svoboda, J., Fischer, F.D., Fratzl, P., Kozeschnik, E., 2004. Modelling of kinetics in multi-component multi-phase systems with spherical precipitates: I: Theory. *Mater. Sci. Eng. A* 385, 166–174. doi:https://doi.org/10.1016/j.msea.2004.06.018
- Taylor, G., 1938. Plastic strain in metals. *J. Inst. Met.* 62, 307.
- Taylor, G.I., 1934. The Mechanism of Plastic Deformation of Crystals. Part I. Theoretical. *Proc. R. Soc. A Math. Phys. Eng. Sci.* 145, 362–387. doi:10.1098/rspa.1934.0106

- Tello, K.E., Gerlich, a. P., Mendez, P.F., 2010. Constants for hot deformation constitutive models for recent experimental data. *Sci. Technol. Weld. Join.* 15, 260–266. doi:10.1179/136217110X12665778348380
- Thornton, P.R., Mitchell, T.E., Hirsch, P.B., 1962. The dependence of cross-slip on stacking fault energy in face centered cubic metals and alloys. *Philos. Mag.* 7, 1349.
- Tóth, L.S., Molinari, A., Estrin, Y., 2002. Strain Hardening at Large Strains as Predicted by Dislocation Based Polycrystal Plasticity Model. *J. Eng. Mater. Technol.* 124, 71. doi:10.1115/1.1421350
- Tutyshkin, N., Müller, W.H., Wille, R., Zapara, M., 2014. Strain-induced damage of metals under large plastic deformation: Theoretical framework and experiments. *Int. J. Plast.* 59, 133–151.
- Tzanetakis, P., Hillairet, J., Revel, G., 1976. Formation energy of vacancies in aluminum and magnesium. *Phys. Status Solidi* 75, 433–439. doi:10.1002/pssb.2220750205
- Uesugi, T., Higashi, K., 2013. First-principles studies on lattice constants and local lattice distortions in solid solution aluminum alloys. *Comput. Mater. Sci.* 67, 1–10. doi:10.1016/j.commatsci.2012.08.037
- Umbrello, D., M'Saoubi, R., Outeiro, J.C., 2007. The influence of Johnson-Cook material constants on finite element simulation of machining of AISI 316L steel. *Int. J. Mach. Tools Manuf.* 47, 462–470. doi:10.1016/j.ijmachtools.2006.06.006
- Verdier, M., Janecek, M., Bréchet, Y., Guyot, P., 1998. Microstructural evolution during recovery in Al-2.5%Mg alloys. *Mater. Sci. Eng. A* 248, 187–197. doi:10.1016/S0921-5093(98)00488-2
- Vissers, R., van Huis, M.A., Jansen, J., Zandbergen, H.W., Marioara, C.D., Andersen, S.J., 2007. The crystal structure of the beta-prime phase in Al-Mg-Si alloys. *Acta Mater.* 55, 3815–3823. doi:10.1016/j.actamat.2007.02.032
- Voce, E., 1955. A practical strain-hardening function. *Metallurgia* 51, 219–226.
- Weertman, J., 1965. Theory of the Influence of Stacking-Fault Width of Split Dislocations on High-temperature Creep Rate. *Trans. Metall. Soc. AIME* 533, 2069–2074.
- Weertman, J., 1957. Steady State creep through dislocation climb. *J. Appl. Phys.* 28, 362–363. doi:10.1063/1.1722747
- Weertman, J., 1956. Creep of polycrystalline aluminium as determined from strain rate tests. *J. Mech. Phys. Solids* 4, 230–234.
- Yan, S.L., Yang, H., Li, H.W., Yao, X., 2016. Variation of strain rate sensitivity of an aluminum alloy in a wide strain rate range: Mechanism analysis and modeling. *J. Alloys Compd.* 688, 776–786.
- Yoshida, F., Uemori, T., 2002. A model of large strain cyclic plasticity describing the Bauschinger effect and workhardening stagnation. *Int. J. Plast.* 18, 661–686.
- Zandbergen, M., Xu, Q., Cerezo, A., Smith, G., 2015. Study of precipitation in Al-Mg-Si alloys by atom probe tomography I. Microstructural changes as a function of ageing temperature. *Acta Mater.* 101, 136–148. doi:https://doi.org/10.1016/j.actamat.2015.08.017
- Zehetbauer, M., Seumer, V., 1993. Cold work hardening in stages IV and V of fcc metals I experiments and interpretation. *Acta Metall. Mater.* 41, 577–588.
- Zehetbauer M., 1993. Cold work hardening in stages IV and V of fcc metals - II. MOdel fits and physical results. *Acta Metall. Mater.* 41, 589–599.
- Zerilli, F., Armstrong, W., 1987. Dislocation mechanics based constitutive relations for material dynamics calculations. *J. Appl. Phys.* 61, 1816–1825.
- Zheng, J., Davies, C.M., Lin, J., Pan, R., Li, C., 2017. Constitutive modelling of a T74 multi-step creep ageing behaviour of AA7050 and its application to stress relaxation ageing in age formed aluminium components, in: ICTP.

# Appendix

## Key Publications

### Paper 1

Kreyca, J., Kozeschnik, E., 2017a. Temperature-dependent strain hardening, precipitation and deformation-induced microstructure evolution in AA 6061. *Mater. Sci. Eng. A* 708, 411–418.

### Paper 2

Kreyca, J., Kozeschnik, E., 2017. Analysis of the Temperature and Strain-Rate Dependences of Strain hardening, *Metall. Mater. Trans. A*, in print.

### Paper 3

Kreyca, J., Kozeschnik, E., 2017. State parameter-based constitutive modelling of stress strain curves in Al-Mg solid solutions. *Int. J. Plast.*, submitted.

## Paper 1

# Temperature-dependent strain hardening, precipitation and deformation-induced microstructure evolution in AA 6061

Johannes Kreyca<sup>a,1\*</sup>, Ernst Kozeschnik<sup>a,2</sup>

<sup>a</sup>*Institute of Materials Science and Technology, TU Wien,  
Getreidemarkt 9, Vienna, 1060, Austria*

<sup>1</sup>*johannes.kreyca@tuwien.ac.at*, <sup>2</sup>*ernst.kozeschnik@tuwien.ac.at*

*\*corresponding author*

### Abstract

The effect of  $\beta''$  precipitation on strain hardening and yield stress evolution in an A6061 aluminium alloy is studied experimentally and through thermokinetic computer simulation. Samples were deformed by compression at temperatures from 25 to 500°C to strains of about 0.4 and three different precipitation states. Simulations on the thermal stability of  $\beta''$  are conducted on an equivalent model Al-Mg-Si alloy resulting in an explanation for the experimentally observed softening at intermediate temperatures. EBSD micrographs confirm that different dislocation storage and annihilation mechanisms are operative at low and high temperatures. The low temperature microstructure correlates very well with the subgrain structures typically observed during stage IV strain hardening.

**Keywords** stress/strain measurements; modelling/simulations; aluminium alloys

### Introduction

AA6061 is a heat treatable aluminium alloy belonging to the 6xxx Al-Mg-Si system. It is appreciated for its good combination of specific strength, corrosion resistance and good weldability. The mechanical properties of A6061 alloy have been investigated intensively. Ozturk et al. [1] published tensile tests for artificial ageing at 200°C and different aging times. Evangelista et al. [2] investigated the hot formability of AA6061 PM in the temperature range of 250-500°C and strain rates from 0.005 to 0.5 s<sup>-1</sup>. Maisonette et al. [3] reports the effect of previous thermal history representative for electron beam welding. Lee and Tang [4] investigated the stress-strain response with a compressive split-Hopkinson pressure bar

system in the temperature range of 100 to 350 °C and strain rates between  $10^3$  and  $5 \cdot 10^3$ . Mechanical properties of 6061 aluminum alloy processed by accumulative roll bonding were studied by Lee et al. [5]. Severe plastic deformation of AA6061 was investigated by Khamei and Deghani [6] and Farshidi et al. [7]. For further experimental data see [8][9][10].

In the present work, the focus lies on the investigation and characterization of thermally activated processes occurring during deformation. In this respect, two aspects need to be accounted for, which are (i) the thermal stability of precipitates and (ii) the characterization of dominant deformation mechanism at different temperatures. For this purpose, a CALPHAD-based thermokinetic simulation of the precipitation and dissolution behaviour of the major hardening phase  $\beta''$  is conducted, first. Subsequently, EBSD micrographs are acquired for artificially aged material that is deformed at different temperatures. Finally, experimentally determined stress-strain curves derived from compression tests at several different temperatures and three different initial precipitation states are interpreted based on the information from the computer simulations and the EBSD micrographs.

#### **Initial strain hardening rate, stage III saturation stress and stage IV strain hardening rate**

As first introduced by Diehl [11][12], stress strain curves are commonly divided into five stages of strain hardening. In polycrystalline materials – such as the material, which is subject to the present work – only stages III and IV are typically observed. Stage III is characterized by a decreasing strain hardening rate with increasing degree of deformation and a strong dependence on temperature and strain rate, where the strain hardening rate,  $\theta$ , is defined as  $\theta = d\sigma/d\varepsilon$ .  $\varepsilon$  represents strain and  $\sigma$  is stress. In the sense of the Kocks-Mecking (KM) model [13], [14] for the strain hardening stage III, the strain hardening rate,  $\theta$ , and stress,  $\sigma$ , follow a simple linear relation (see also [15]) in the form of

$$\theta = \theta_0 \left( 1 - \frac{\sigma - \sigma_0}{\sigma_\infty} \right),$$

where  $\sigma_0$  and  $\theta_0$  are the yield stress and the strain hardening rate at deformation start, respectively, and  $\sigma_\infty$  is the saturation stress. The quotient  $\varepsilon_c = \theta_0/\sigma_\infty$  is sometimes referred to as critical strain. Fig. 1 shows a schematic representation of a stress strain curve generated by application of the KM model for stage III hardening.

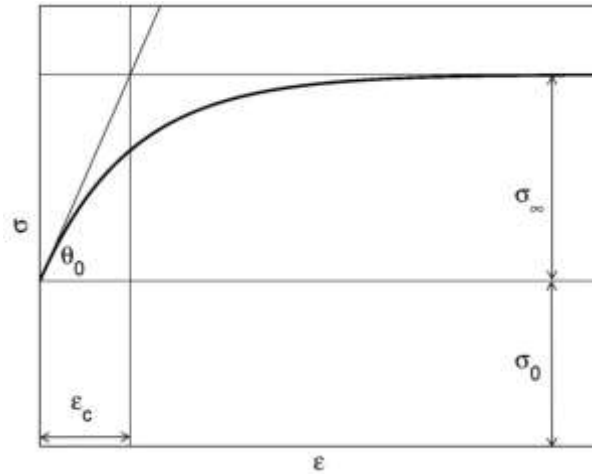


Fig. 1 Schematic stress-strain curve in stage III with  $\sigma_0$ ,  $\theta_0$ ,  $\varepsilon_c$  and  $\sigma_\infty$ .

According to the KM model, the dislocation density evolution is described by  $d\rho/d\varepsilon = k_1\sqrt{\rho} - k_2\rho$ , where  $k_1$  is the dislocation storage parameter and  $k_2$  is the dynamic recovery coefficient. Together with the Taylor equation,  $\sigma = \sigma_0 + \alpha GbM\sqrt{\rho}$ , where  $\alpha$  is a strengthening coefficient [16],  $G$  is the shear modulus and  $b$  is the Burgers vector, it can be shown that the initial strain hardening rate and the critical strain are related to the dislocation storage parameter,  $k_1$ , and dynamic recovery coefficient,  $k_2$ , through  $\theta_0 = \alpha GbM^2 k_1/2$  and  $\varepsilon_c = k_2 M/2$  [17]. The KM model has been successfully applied to simulate strain hardening in Al alloys [18],[19],[20],[21] and [22].

Stage III is followed by Stage IV, which is characterized by a constant strain hardening rate resulting in a straight line in the stress strain diagram. Stage IV is fully determined by only a single parameter,  $\theta_{IV}$ .

### Precipitation sequence in AA6061

In the Al-Mg-Si system, the mechanical properties mainly result from precipitation strengthening of Mg and Si-containing particles. In 6061 alloys,  $Mg_5Si_6$  ( $\beta''$ ) is the major hardening phase [23], [24], [25], [26]. Fig. 2 shows the typical precipitation sequence observed during heat treatment of Al-Mg-Si alloys [27] and [28].

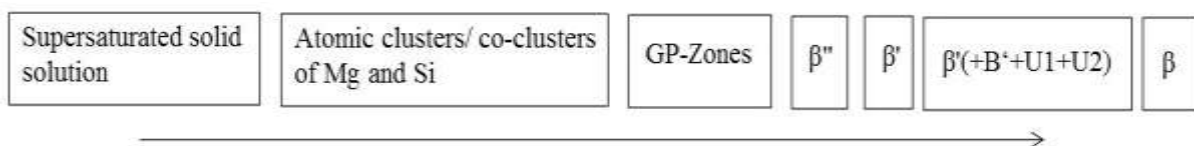


Fig. 2 Typical precipitation sequence in Al-Mg-Si alloys

The precipitation sequence is subject to numerous models predicting the yield stress evolution during artificial ageing as a function of composition, ageing time, temperature and, sometimes, also the thermal history of the material. In the present context, Shercliff and Ashby developed a corresponding model dealing with precipitation strengthening in age hardening alloys [29], [30]. Later on, Myhr and co-workers published a series of papers [31], [32], [33], [34] on this topic with special focus on Al alloys. The strengthening impact of needle-shaped precipitates, such as the  $\beta''$  phase, was investigated in [35]. The impact of precipitates on the dislocation density evolution (strain hardening) is incorporated in the model of Friis et al. [36] and, in a more complex form, of Simar et al. [37]. An exhaustive review on different models with special emphasis on modelling the heat affected zone during welding in heat treatable aluminium alloys is given in [38].

Independent of the particular type of Al-alloy, the precipitation processes occurring during heat treatment of technical alloys are reasonably well understood and they are nowadays often modelled in a combination of CALPHAD-type multi-component equilibrium thermodynamics and suitable approaches dealing with the kinetics of precipitation, e.g. [39], [40].

### **Simulation of the precipitation state of hardening phases**

In the present work, the precipitation sequence occurring during heat treatment of a model Al-Mg-Si ternary alloy is simulated. The chemical composition (0.85 wt.% Mg, 0.69 wt.% Si, Al bal.) lies well within the range defined for A6061 aluminium. The resulting phase fraction and precipitate distribution of  $\beta''$  particles corresponding to a specific precipitation state is subsequently used as starting condition for the simulation of the dissolution/growth kinetics of the  $\beta''$  phase during isothermal mechanical testing. This latter simulation of precipitation state is especially interesting, since, during deformation at elevated temperature, the precipitation state might change due to further precipitation, coarsening or, eventually, dissolution, which directly impacts the mechanical properties (stress-strain curves) of the material.

All calculations presented here are performed with the thermokinetic software package MatCalc (version 6.00 rel. 0.104) [41] using the databases *mc\_al.tdb* [42] and *mc\_al.ddb* [43]. These databases are available under the Open Database License [44] and can be

downloaded for free from <http://matcalc.at>. They contain all thermodynamic and diffusion related parameters necessary for the reproduction of the present results. MatCalc simulations utilize a mean-field approach for nucleation, growth and coarsening in multi-component, multi-phase and multi particle systems [45], [46], [47]. The interface energies are calculated according to the generalized nearest neighbour broken bond model [48], [49]. For simulations in Al-based alloys, this approach is coupled with a model describing the evolution of quenched-in excess vacancies [50] and their impact on solute diffusion. The influence of coherent misfit stress on nucleation is taken into account by assuming an effective volumetric misfit between precipitates and matrix of 4, 4, and 2 % for GP-zones,  $\beta'$  and  $\beta''$ , respectively. The phases  $\beta'$  and  $\beta''$  are assumed to be rod shaped with an aspect ratio of  $H/D=10$  [51] where  $H$  is the length of the precipitate, and  $D$  the thickness of a cylinder with equivalent volume. Fig. 3 shows simulation results for the intermediate region of the precipitation sequence, as modelled for the artificial ageing stage at 170°C, only, and a pre-treatment as described in the figure caption.

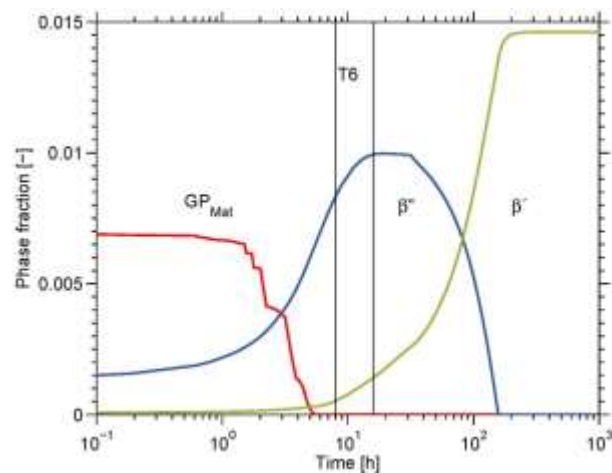


Fig. 3 Precipitation sequence of Mg-Si precipitates after quenching from solution annealing temperature to room temperature with  $900 \text{ Ks}^{-1}$ , heating with  $3 \text{ Ks}^{-1}$  and isothermal holding at 170°C for the phases GP-Mat,  $\beta''$  and  $\beta'$ . Also shown is the T6 region according to DIN EN 2700.

Fig. 3 shows that the T6 material state, which represents the standard heat treatment for peak strengthening of Al alloys, corresponds to a condition with close-to-maximum phase fraction of  $\beta''$ . It is important to note, that Fig. 3 is only valid for an isothermal heat treatment carried out at 170°C after solution annealing, quenching and reheating with the

rates given in the caption of Fig. 3. Above a certain temperature, the  $\beta''$  precipitates become thermodynamically unstable and start dissolving.

Fig. 4 shows the phase fraction evolution of  $\beta''$  during isothermal heat-treatment at different temperatures and over (a) 70 seconds and (b) 1000h, where 70 seconds corresponds to deformation test conditions up to a strain of 0.7 with a strain rate of 0.01. The precipitate evolution in Fig. 4 (b) is shown to demonstrate the long-term evolution of precipitates when approaching equilibrium conditions and even longer testing duration. The initial precipitation state / phase fraction of  $\beta''$  is taken from Fig. 3 after isothermal heat-treatment at 170°C for four hours.

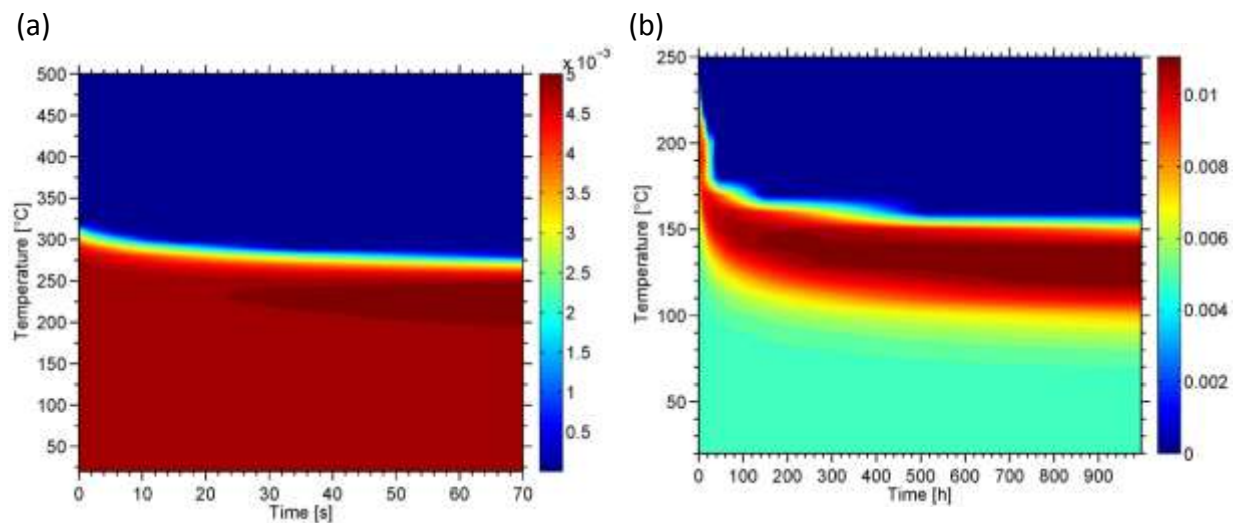


Fig. 4 Dissolution of  $\beta''$  precipitates during iso-thermal heat treatment for (a) 70 s and (b) 1000h, with the phase-fractions given by the color coding.

Fig. 4 (a) shows three regions: (i) from room temperature up to approximately 250°C, the phase fraction of  $\beta''$  is stable or even slightly increasing, (ii) between 250°C-300°C,  $\beta''$  is dissolved within the first 70 seconds and (iii) above 300°C precipitates are dissolved within the first instances of heat treatment, as carried out in the present investigation. Especially interesting is the region between 250 and 300°C where, in the beginning of mechanical testing, precipitates act as obstacles, but they are dissolved during deformation. An initial strain hardening with a subsequent softening is, consequently, expected for stress strain curves in this region.

Fig. 4 (b) shows that, for temperatures higher than 170°C, and for testing with rather slow strain rates and long testing duration,  $\beta''$  is dissolved within approximately the first 100h. The simulations thus show that any  $\beta''$  precipitation is rapidly dissolved at temperatures

higher than 300°C, continuously dissolved between 250 and 300°C, growing at temperatures lower than 250°C and unchanged for temperatures lower than 100°C. Apart from the temperature-dependent evolution of precipitates, the dominant deformation mechanism and, thus, the deformation-induced microstructure is gradually changing with increasing temperature [52]. In the present work, the temperature dependent deformation microstructure is characterized by EBSD micrographs and, finally, compared to stress-strain curves obtained from compression testing.

### Experimental Procedure

Cylindrical specimens of a commercial A6061 alloy with a length of 15mm and a diameter of 10mm are compression-tested on a Gleeble 1500 thermo-mechanical simulator. Colloidal graphite is used for lubrication. The chemical composition is summarized in Table 1.

Table 1 Chemical Composition

Element	Al	Si	Fe	Cu	Mn	Mg	Cr	Ni	Zn	Ti
Concentration [wt.%]	97.35	0.69	0.45	0.23	0.11	0.85	0.18	<0.05	0.05	0.05

The material is solution heat treated for 1h at 540°C in a furnace, water quenched and, after storage at room temperature for one week, artificially aged for 1, 4 and 8h at 170°C. All specimens are tested at a strain rate of 0.01 s<sup>-1</sup> and at temperatures of 25, 50 100, 150, 200, 250, 300, 350, 400, 450 and 500°C. The tests are repeated three times, the experimental values represent the average of three experiments. All stress-strain curves are calculated under the assumption of constant volume. Values for  $\sigma_0$  are taken at a strain of  $\varepsilon=0.02$ . The experimental values for  $\theta_0$  and  $\sigma_\infty$  are evaluated from the KM-plots ( $\theta$  vs.  $\sigma_p$ ) of the data in Fig. 5, where  $\theta$  is determined from numerical differentiation and  $\sigma_p = \sigma - \sigma_0$ . Minimization of the sum of least squares is then used to best-fit the linear relation between strain hardening rate and stress postulated by the KM model. The intercept of the resulting line with ordinate and abscissa determines the experimental values for  $\theta_0$  and  $\sigma_\infty$ . The strain hardening rate in stage IV,  $\theta_{IV}$ , is derived by fitting stress strain curves in the strain range of 0.15-0.4 with a straight line.

EBSD micrographs are taken from a subset of deformed samples ( $\varepsilon = 0.2$ ) after solution heat treatment for 1h at 540°C, heat treatment for 4h hours at 170°C and deformation at 25, 150, 200, 350, 400 and 450°C. The steps for grinding and polishing [11] are summarized in Table

2.

Table 2 Grinding and polishing

Step	Polishing Disc	Grit ( $\mu\text{m}$ )	Time (min)
Grinding	Abrasive Paper	500	2
Polishing	Struers MD Largo	9	15
Polishing	Struers MD Dur	6	25
Polishing	Struers MD Mol	3	30
OPS	Struers MD-Chem	1	15
Cleaning	Struers MD-Chem	1	3

The EBSD investigations are performed on an FEI Quanta 200 FEG. The data analysis is conducted with the EDAX Orientation Imaging Microscopy (OIM) Data Analysis software.

### Deformation-induced microstructures

Fig. 5 shows EBSD micrographs for the present A6061 alloy, heat treated for 4h at 170°C after solution heat treatment and deformed at 25, 150, 200, 350, 400 and 450°C up to a strain level of 0.2. For 25, 150 and 200°C, the appearance of microstructure can be clearly attributed to classical cold working. According to [53], [54] and [55], thermally activated cross-slip represents the main physical mechanism determining the temperature-dependence of stress-strain curves at low and intermediate temperatures. The geometrically ordered microstructure, which is typically observed after deformation at these temperatures [56], [57], [58], [59] is reflected in the images (a)-(c) of Fig. 5. At elevated temperatures, non-conservative motion of dislocations, e.g., vacancy-assisted dislocation climb, becomes the predominant mechanism determining the stress-strain behaviour. The enhanced mobility of dislocations at elevated temperature results in a characteristic microstructure, dominated by randomly oriented subgrains, Fig. 5 (d,e), which is commonly associated with lower levels of yield stress and strain hardening. At even higher temperatures, a mixture of grains structured with subgrains and recrystallized grains is observed, Fig. 5 (f). Two regions of different deformation microstructures are consequently found in experimentally determined stress strain curves: One with high yield stress and high strain hardening rate due to thermally activated cross-slip and another one dominated by vacancy assisted climb with lower yield stress and reduced strain hardening rate. The shift between the two mechanisms is expected to occur between 200 and 350°C, Fig. 5 (c,d).

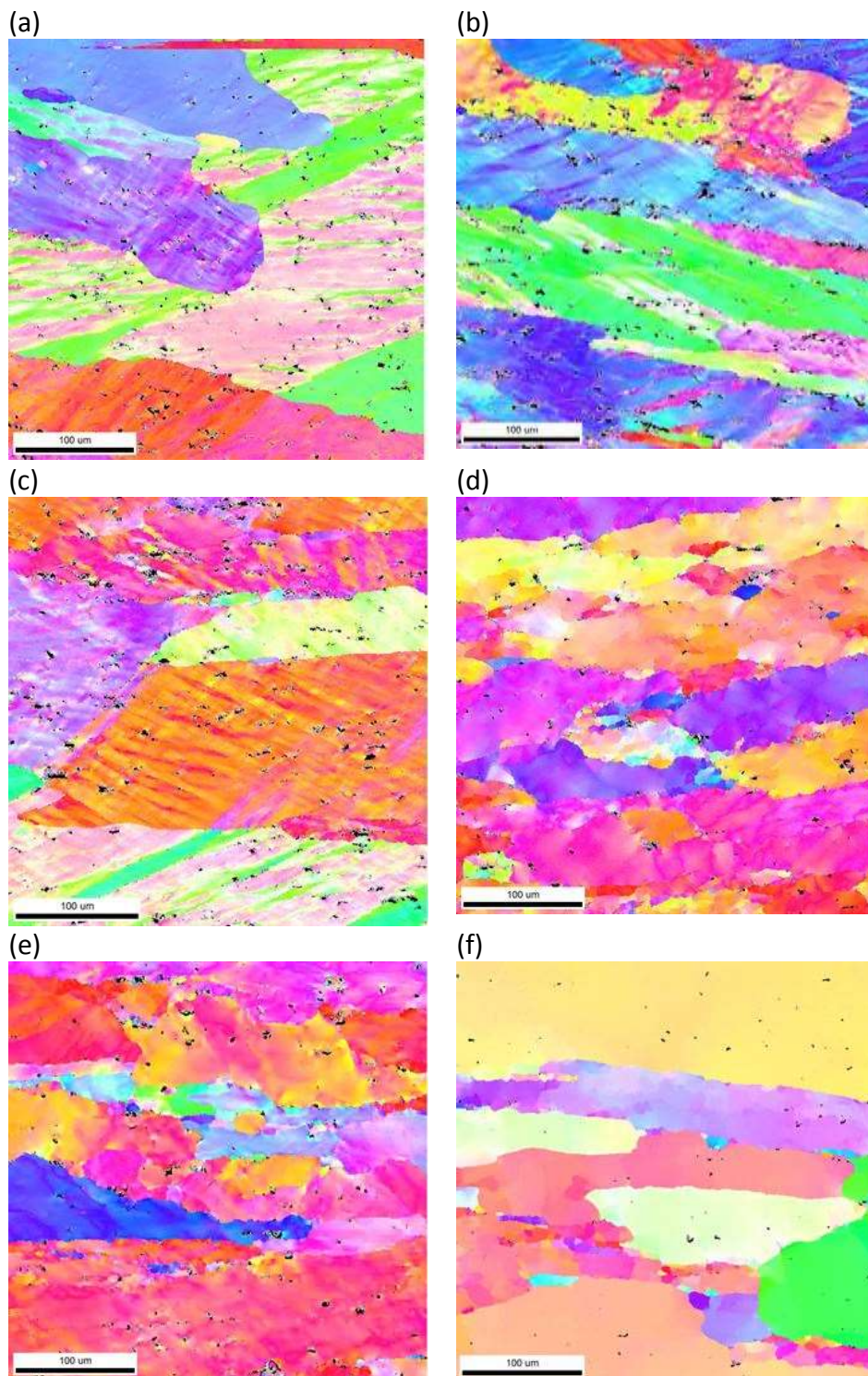
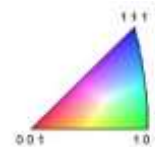


Fig. 5 EBSD Micrographs of A6061 artificially aged for 4h hours and tested at (a) 25, (b) 150, (c) 200, (d) 350, (e) 400 and (f) 450°C at a strain of 0.2



### Stress strain curves

Fig. 6 shows plots of true stress vs. true strain for all artificial ageing times and temperatures. From room temperature up to roughly 200°C, stage III hardening is observed in the beginning, followed by stage IV hardening with a constant strain hardening rate. With increasing temperature, the degree of strain hardening decreases in both stages. Up to 250°C, the stress is continuously increasing during deformation, i.e. the strain hardening rate is positive throughout the whole deformation process. At 250°C the strain hardening rate in stage IV becomes zero, i.e.  $\theta_{IV} = d\sigma_{IV}/d\varepsilon = 0$ .

In the temperature range between 250°C and 400°C, an initial region of strain hardening is followed by a region of softening during deformation. Interestingly, dynamic recrystallization can be excluded as mechanism responsible for this softening, since recrystallization does not occur until temperatures above 400°C (Fig. 5). A comparison with the simulated precipitation state shown in Fig. 3 indicates that this reduction in strength coincides with the region of  $\beta''$  dissolution, which apparently commences in the course of compression testing and continues to a higher degree with increasing test temperature. This dissolution is accompanied by a loss in precipitation strengthening and, thus, an integral softening in the stress-strain curve. At temperatures above 400°C, no conceivable strain hardening occurs and stress saturation is reached almost immediately after deformation start.

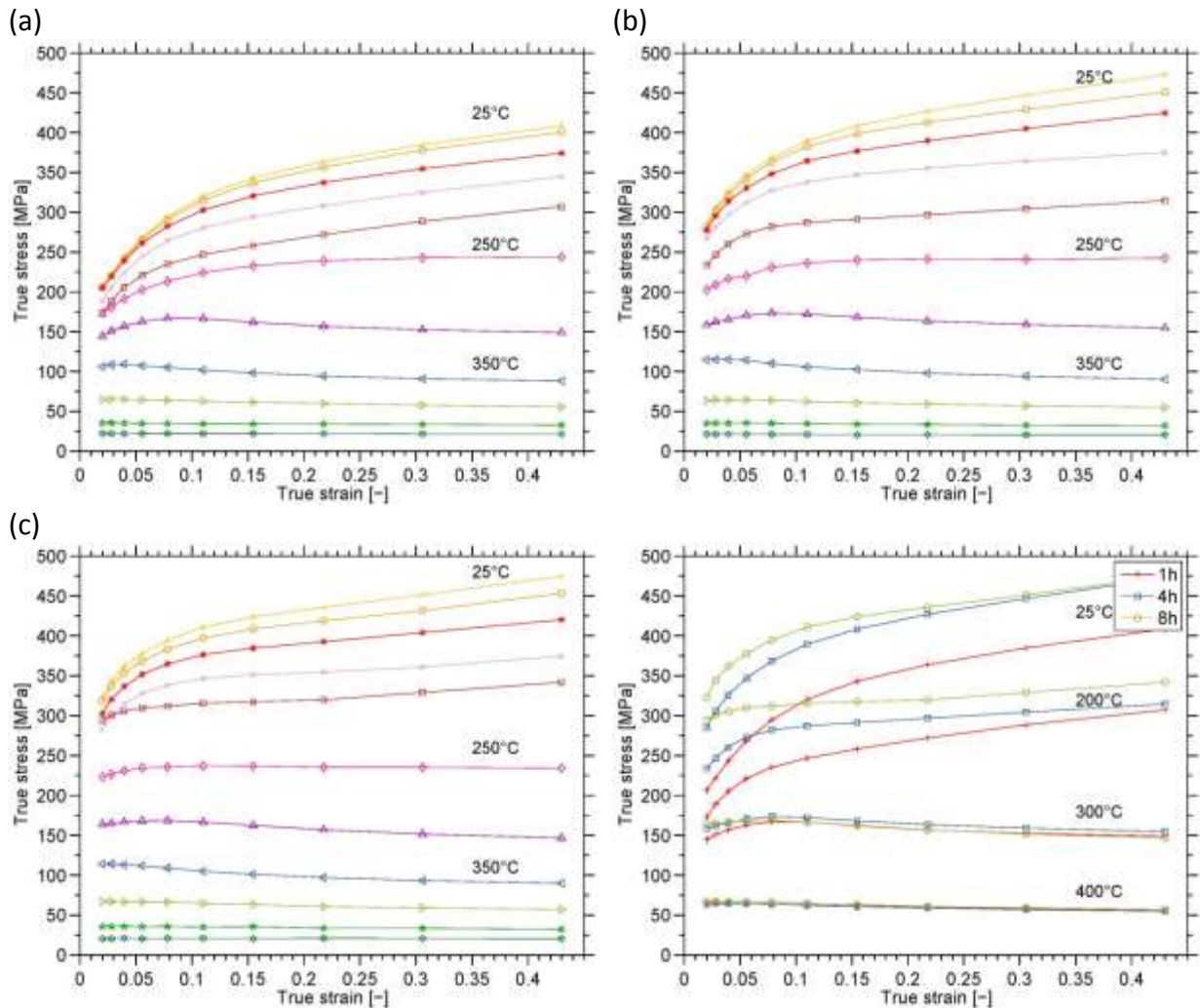


Fig 6. Stress strain curves for (from highest to lowest) 25, 50 100, 150, 200, 250, 300, 350, 400, 450 and 500°C, (a) 1h, (b) 4h, and (c) 8h artificial ageing at 170°C. (d) shows selected true stress over true strain curves for 1, 4 and 8h and 25, 200, 300, 400°C.

Fig 6 (d) displays selected stress-strain curves for the same test temperature but different precipitation states, i.e., aging times. Apparently, at temperatures below 300°C, the initial yield stress as well as the strain hardening behaviour are significantly different for different ageing times. At 300°C, only a weak difference in yield stress and strain hardening rate between different precipitations states is observed at deformation start. This difference, however, disappears as soon as the precipitates fully dissolve during the deformation process. Deformation at 400°C renders identical stress strain curves, indicating that precipitates are dissolved already quickly at deformation start and deformation occurs for almost identical microstructures, in the absence of the influence of precipitates, in all cases. The vast differences in stress-strain behaviour at lower temperatures are further analysed subsequently.

Fig. 7. shows the values of yield stress,  $\sigma_0$ , initial strain hardening rate,  $\theta_0$ , stage III saturation stress,  $\sigma_\infty$ , and strain hardening rate in stage IV,  $\theta_{IV}$ . All four quantities show decreasing tendency with increasing temperature. This is especially interesting for the initial strain hardening rate,  $\theta_0$ , as it is sometimes assumed to be athermal [13].

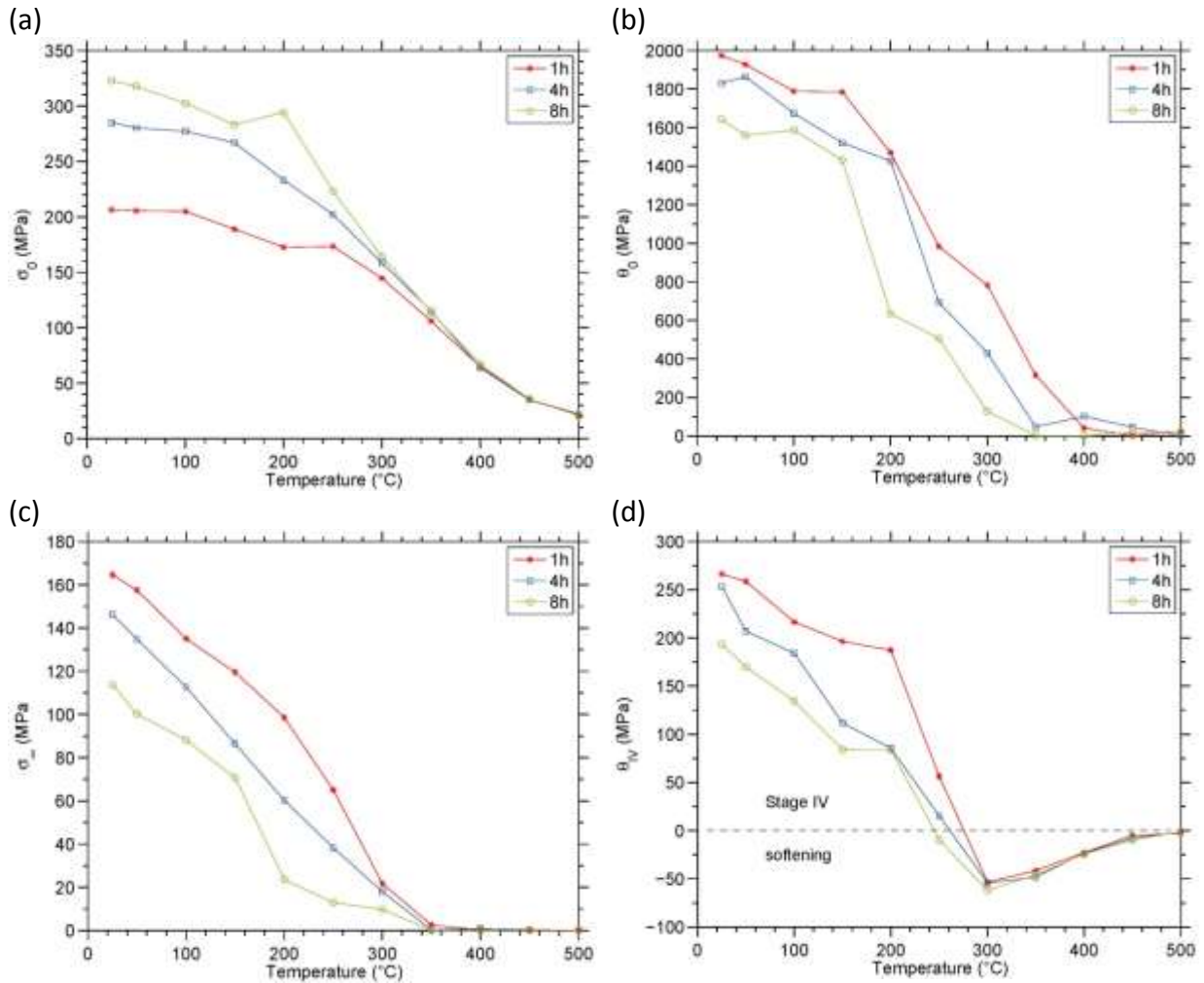


Fig. 7 (a) yield stress, (b) initial strain hardening rate, (c) saturation stress and (d) strain hardening rate in stage IV for 1, 4 and 8h of artificial ageing at 170°C over temperature.

As expected, the initial yield stress,  $\sigma_0$ , is increasing with increasing ageing time due to the increasing contribution of precipitation strengthening. At the same time,  $\theta_0$  and  $\sigma_\infty$  are decreasing with increasing ageing time. Consequently, the presence of precipitates leads to higher initial yield stress values but reduces the materials capacity for strain hardening. A similar behaviour was observed by Fribourg et al. [20] for a 7000 series aluminium alloy. At temperatures higher than 300°C, no significant strain hardening is observed any more. This is in good accordance with the shift in deformation mechanism from thermally activated cross slip to vacancy assisted climb, as observed from the analysis of EBSD micrographs.

Fig. 7 (d) shows the evolution of  $\theta_{IV}$  over temperature. Up to temperatures of roughly 250°C, clear evidence of stage IV hardening is observed (compare Fig. 6), the magnitude of the hardening coefficient, however, is quickly decreasing with increasing temperatures. Just as for stage III hardening, the stage IV strain hardening potential decreases with increasing precipitation strengthening. At roughly 250°C,  $\theta_{IV}$  becomes zero and the stress-strain curve saturates after the end of stage III. At even higher temperatures,  $\theta_{IV}$  is negative and must be interpreted as measure of softening due to precipitate dissolution rather than conventional strain hardening.

Fig. 8 shows values for  $\sigma_0$ ,  $\theta_0$  and  $\sigma_\infty$  normalized with the corresponding values at room temperature. Most interestingly, the evolution over temperature shows a similar ‘s’ shape for all three quantities with almost identical slope, where only the point of inflection is shifted to lower temperature from  $\sigma_0$  over  $\theta_0$  to  $\sigma_\infty$ . Fig. 8 leads to the speculation that a model for the thermal activation of the yield stress [52], [60] could – in principle and with individual parametrization – be also applied to the initial yield stress and the saturation stress and, with the relations between  $\theta_0$ ,  $\sigma_\infty$  and  $k_1$ ,  $k_2$ , deliver expressions for the thermal activation of dislocation storage and dynamic recovery. If, in addition to that, the empirical relation [14],[61] between the temperature and strain rate dependence of stage IV and that of stage III hardening is applied, a model for the temperature-dependence of yield stress, stage III and IV hardening and, thus, for the whole stress strain curve at lower temperatures could be derived. For higher temperatures, the observed precipitate dissolution and high temperature deformation mechanisms must additionally be taken into account.

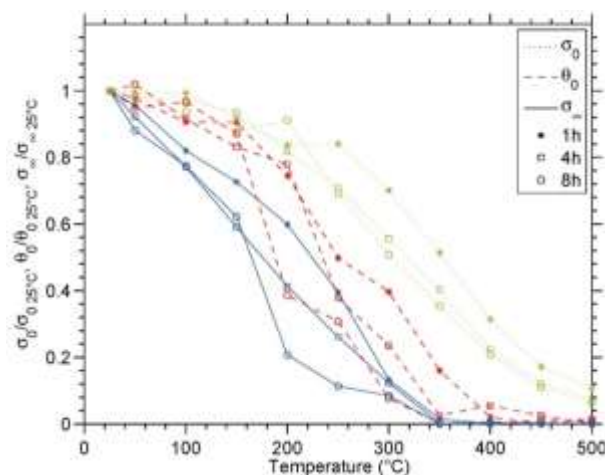


Fig. 8 Yield stress, initial strain hardening rate and saturation stress normalized by room temperature values.

## Conclusion

The plastic deformation of an A6061 heat treatable aluminium alloy is investigated over a large range of temperatures and three different precipitation states. At low temperature up to 200°C, stage III and IV hardening, which are characteristic for conditions of cold working, are observed in stress-strain curves. In this region, the evolution of yield stress during artificial ageing is observed to be indirectly proportional to the materials potential for strain hardening. The yield stress, initial strain hardening rate and saturation stress are monotonically decreasing with increasing temperatures. Corresponding EBSD micrographs show a highly organized banded structure with a geometrical relation to the rolling direction. At higher temperatures, the deformation microstructure is dominated by randomly oriented subgrains.

Thermokinetic simulation of the precipitation kinetics of the major hardening phase indicates that, between 250°C and 300°C, the main hardening phase  $\beta''$  dissolves within the first seconds of deformation resulting in softening that is clearly visible in the experimentally determined stress-strain curves. EBSD analysis confirms that, in the present case, the observed softening is not related to dynamic recrystallization.

## Acknowledgements

This research did not receive any specific grant from funding agencies in the public, commercial, or not-for-profit sectors.

- [1] F. Ozturk, A. Sisman, S. Toros, S. Kilic, R.C. Picu, Influence of aging treatment on mechanical properties of 6061 aluminum alloy, *Mater. Des.* 31 (2010) 972–975. doi:10.1016/j.matdes.2009.08.017.
  
- [2] E. Evangelista, A. Forcellese, F. Gabrielli, P. Mengucci, Hot formability of AA6061 PM aluminium alloy, *J. Mater. Process. Technol.* 24 (1990) 323–332. doi:https://doi.org/10.1016/0924-0136(90)90193-X.

- [3] D. Maisonette, M. Suery, D. Nelias, P. Chaudet, T. Epicier, Effects of heat treatments on the microstructure and mechanical properties of a 6061 aluminium alloy, *Mater. Sci. Eng. A.* 528 (2011) 2718–2724. doi:<https://doi.org/10.1016/j.msea.2010.12.011>.
- [4] W. Lee, Z. Tang, Relationship between mechanical properties and microstructural response of 6061-T6 aluminum alloy impacted at elevated temperatures, *Mater. Des.* 58 (2014) 116–124. doi:<https://doi.org/10.1016/j.matdes.2014.01.053>.
- [5] S.H. Lee, Y. Saito, T. Sakai, H. Utsunomiya, Microstructures and mechanical properties of 6061 aluminum alloy processed by accumulative roll-bonding, *Mater. Sci. Eng. A.* 325 (2002) 228–235. doi:10.1016/S0921-5093(01)01416-2.
- [6] A. Khamei, K. Deghani, Effects of strain rate and temperature on hot tensile deformation of severe plastic deformation 6061 aluminum alloy, *Mater. Sci. Eng. A.* 627 (2015) 1–9. doi:<https://doi.org/10.1016/j.msea.2014.12.081>.
- [7] M.H. Farshidi, M. Kazeminezhad, H. Miyamoto, Severe plastic deformation of 6061 aluminum alloy tube with pre and post heat treatments, *Mater. Sci. Eng. A.* 563 (2013) 60–67. doi:10.1016/j.msea.2012.11.025.
- [8] V.L. Niranjani, K.C. Hari Kumar, V. Subramanya Sarma, Development of high strength Al-Mg-Si AA6061 alloy through cold rolling and ageing, *Mater. Sci. Eng. A.* 515 (2009) 169–174. doi:10.1016/j.msea.2009.03.077.
- [9] B. Mirzakhani, M. Mansourinejad, Tensile properties of AA6061 in different designated precipitation hardening and cold working, *Procedia Eng.* 10 (2011) 136–140. doi:10.1016/j.proeng.2011.04.025.
- [10] D.D. Rianti, M. Yin, P.E.J.R.D. del Castillo, S. van der Zwaag, A systematic study of the effect of interrupted ageing conditions on the strength and toughness development of AA6061, *Mater. Sci. Eng. A.* 523 (2009) 99–111. doi:10.1016/j.msea.2009.06.044.
- [11] J. Diehl, Zugverformung von Kupfer Einkristallen 1. Verfestigungskurven und Oberflächenerscheinungen, *Zeitschrift Für Met.* 47 (1956) 331–343.
- [12] J. Diehl, S. Mader, A. Seeger, Gleitmechanismus und Oberflächenerscheinungen bei kubisch flächenzentrierten Metallen, *Zeitschrift Für Met.* 46 (1955) 650–657.
- [13] U.F. Kocks, Laws for Work-Hardening and Low-Temperature Creep, *J. Eng. Mater. Technol.* (1976) 76–85. doi:10.1115/1.3443340.

- [14] U.F. Kocks, H. Mecking, Physics and phenomenology of strain hardening: The FCC case, *Prog. Mater. Sci.* 48 (2003) 171–273. doi:10.1016/S0079-6425(02)00003-8.
- [15] E. Voce, A practical strain-hardening function, *Metallurgia.* 51 (1955) 219–226.
- [16] M. Sauzay, L.P. Kubin, Scaling laws for dislocation microstructures in monotonic and cyclic deformation of fcc metals, *Prog. Mater. Sci.* 56 (2011) 725–784. doi:10.1016/j.pmatsci.2011.01.006.
- [17] A. Simar, Y. Bréchet, B. de Meester, A. Denquin, T. Pardoen, Sequential modeling of local precipitation, strength and strain hardening in friction stir welds of an aluminum alloy 6005A-T6, *Acta Mater.* 55 (2007) 6133–6143. doi:10.1016/j.actamat.2007.07.012.
- [18] L.M. Cheng, W.J. Poole, J.D. Embury, D.J. Lloyd, The influence of precipitation on the work hardening behavior of the aluminum alloys AA6111 and AA7030, *Metall. Mater. Trans. A.* 34 (2003) 2913–2924. doi:DOI: 10.1007/s11661-003-0007-2.
- [19] S. Esmaili, L. Cheng, A. Deschamps, D. Lloyd, W. Poole, The deformation behaviour of AA6111 as a function of temperature and precipitation state, *Mater. Sci. Eng.* 319 (2001) 461–465. doi:https://doi.org/10.1016/S0921-5093(01)01113-3.
- [20] G. Fribourg, Y. Brechet, A. Deschamps, A. Simar, Microstructure-based modelling of isotropic and kinematic strain hardening in a precipitation-hardened aluminium alloy, *Acta Mater.* 59 (2011) 3621–3635. doi:10.1016/j.actamat.2011.02.035.
- [21] A. Deschamps, Y. Bréchet, C.J. Necker, S. Saimoto, J.D. Embury, Study of large strain deformation of dilute solid solutions of Al-Cu using channel-die compression, *Mater. Sci. Eng. A.* 207 (1996) 143–152. doi:10.1016/0921-5093(95)09992-1.
- [22] A. Deschamps, S. Esmaili, W.J. Poole, M. Militzer, Strain hardening rate in relation to microstructure in precipitation hardening materials, *Le J. Phys. IV.* 10 (2000) Pr6-151-Pr6-156. doi:10.1051/jp4:2000626.
- [23] P. Ninive, A. Strandlie, S. Gulbrandsen-Dahl, W. Lefebvre, C. Marioara, S. Andersen, J. Friis, R. Holmestad, Detailed atomistic insight into the beta dp phase in Al-Mg-Si alloys, *Acta Mater.* 69 (2014) 126–134. doi:https://doi.org/10.1016/j.actamat.2014.01.052.
- [24] C. Marioara, S. Andersen, H. Zandbergen, R. Holmestad, The influence of alloy composition on precipitates of the Al-Mg-Si System, *Metall. Mater. Trans. A.* 36A

(2005) 691–702. doi:<http://dx.doi.org/10.1007/s11661-005-0185-1>.

- [25] C. Ravi, C. Wolverton, First-principles study of crystal structure and stability of Al-Mg-Si-(Cu) precipitates, *Acta Mater.* 52 (2004) 4213–4227. doi:<https://doi.org/10.1016/j.actamat.2004.05.037>.
- [26] M. Zandbergen, Q. Xu, A. Cerezo, G. Smith, Study of precipitation in Al-Mg-Si alloys by atom probe tomography I. Microstructural changes as a function of ageing temperature, *Acta Mater.* 101 (2015) 136–148. doi:<https://doi.org/10.1016/j.actamat.2015.08.017>.
- [27] K. Matsuda, H. Gamada, K. Fujii, Y. Uetani, T. Sato, A. Kamio, S. Ikeno, High-Resolution Electron Microscopy on the Structure of Guinier–Preston Zones in an Al-1.6 Mass Pct Mg 2 Si Alloy, *Metall. Mater. Trans. A.* 29A (1998) 1161–1167. doi:[10.1007/s11661-998-0242-7](https://doi.org/10.1007/s11661-998-0242-7).
- [28] R. Vissers, M.A. van Huis, J. Jansen, H.W. Zandbergen, C.D. Marioara, S.J. Andersen, The crystal structure of the beta-prime phase in Al-Mg-Si alloys, *Acta Mater.* 55 (2007) 3815–3823. doi:[10.1016/j.actamat.2007.02.032](https://doi.org/10.1016/j.actamat.2007.02.032).
- [29] H. Shercliff, M. Ashby, A process model for age hardening of aluminium alloys I. The Model, *Acta Metall. Mater.* 38 (1990) 1789–1802. doi:[https://doi.org/10.1016/0956-7151\(90\)90291-N](https://doi.org/10.1016/0956-7151(90)90291-N).
- [30] H. Shercliff, M. Ashby, A process model for age hardening of aluminium alloys II Applications of the model, *Acta Metall. Mater.* 38 (1990) 1803–1812. doi:[https://doi.org/10.1016/0956-7151\(90\)90292-O](https://doi.org/10.1016/0956-7151(90)90292-O).
- [31] O. Myhr, O. Grong, K. Pedersen, A combined precipitation, yield strength and work hardening model for Al-Mg-Si alloys, *Metall. Mater. Trans. A.* 41A (2010) 2276–2289. doi:[DOI: 10.1007/s11661-010-0258-7](https://doi.org/10.1007/s11661-010-0258-7).
- [32] O. Myhr, O. Grong, S. C., An extended Age hardening model for Al-Mg-Si alloys incorporating the room temperature storage and cold deformation process stages, *Metall. Mater. Trans. A.* 46A (2015) 6018–6039. doi:[10.1007/s11661-015-3175-y](https://doi.org/10.1007/s11661-015-3175-y).
- [33] O. Myhr, O. Grong, S. Andersen, Modelling of the age hardening behaviour of Al-Mg-Si alloys, *Acta Mater.* 49 (2001) 65–75. doi:[https://doi.org/10.1016/S1359-6454\(00\)00301-3](https://doi.org/10.1016/S1359-6454(00)00301-3).
- [34] O. Myhr, O. Grong, H. Fjaer, C. Marioara, Modelling of the microstructure and

- strength evolution in Al-Mg-Si alloys during multistage thermal processing, *Acta Metall. Mater.* 52 (2004) 4997–5008. doi:<https://doi.org/10.1016/j.actamat.2004.07.002>.
- [35] D. Bardel, M. Perez, D. Nelias, A. Deschamps, C.R. Hutchinson, D. Maisonnette, T. Chaise, J. Garnier, F. Bourlier, Coupled precipitation and yield strength modelling for non-isothermal treatments of a 6061 aluminium alloy, *Acta Metall. Mater.* 62 (2014) 129–140. doi:<https://doi.org/10.1016/j.actamat.2013.09.041>.
- [36] J. Friis, B. Holmedal, O. Ryen, E. Nes, O. Myhr, O. Grong, T. Furu, K. Marthinsen, Work hardening behaviour of heat treated Al-Mg-Si alloys, *Mater. Sci. Forum.* (2006). doi:[10.4028/www.scientific.net/MSF.519-521.1901](https://doi.org/10.4028/www.scientific.net/MSF.519-521.1901).
- [37] A. Simar, Y. Brechet, B. de Meester, A. Denquin, T. Pardoen, Sequential modeling of local precipitation, strength and strain hardening in friction stir welds of an aluminum alloy 6005A-T6, *Acta Mater.* 55 (2007) 6133–6143. doi:[10.1016/j.actamat.2007.07.012](https://doi.org/10.1016/j.actamat.2007.07.012).
- [38] A. Simar, Y. Brechet, B. de Meester, A. Denquin, C. Gallais, T. Pardoen, Integrated modeling of friction stir welding of 6xxx series Al alloys: Process, microstructure and properties, *Prog. Mater. Sci.* 57 (2012) 95–183. doi:[10.1016/j.pmatsci.2011.05.003](https://doi.org/10.1016/j.pmatsci.2011.05.003).
- [39] E. Povoden-Karadeniz, P. Lang, P. Warczok, A. Falahati, W. Jun, E. Kozeschnik, CALPHAD modeling of metastable phases in the Al-Mg-Si system, *Calphad Comput. Coupling Phase Diagrams Thermochem.* 43 (2013) 94–104. doi:[10.1016/j.calphad.2013.03.004](https://doi.org/10.1016/j.calphad.2013.03.004).
- [40] P. Lang, E. Povoden-Karadeniz, A. Falahati, E. Kozeschnik, Simulation of the effect of composition on the precipitation in 6xxx Al alloys during continuous-heating DSC, *J. Alloys Compd.* 612 (2014) 443–449. doi:<https://doi.org/10.1016/j.jallcom.2014.05.191>.
- [41] E. Kozeschnik, MatCalc, Solid State Precip. Kinet. Simul. Softw. (2017). <http://matcalc.tuwien.ac.at/> (accessed October 2, 2017).
- [42] E. Povoden-Karadeniz, MatCalc Thermodynamic Database, “Mc\_al.tdb.” (2017). <http://matcalc.tuwien.ac.at/index.php/databases/open-databases> (accessed October 2, 2017).
- [43] E. Povoden-Karadeniz, MatCalc Diffusion Database, “Mc\_al.ddb.” (2017). <http://matcalc.tuwien.ac.at/index.php/databases/open-databases> (accessed October 2, 2017).

- [44] Open database license, ODbL. (n.d.). <https://opendatacommons.org/licenses/odbl/1.0/> (accessed October 2, 2017).
- [45] J. Svoboda, F.D. Fischer, P. Fratzl, E. Kozeschnik, Modelling of kinetics in multi-component multi-phase systems with spherical precipitates I: Theory, *Mater. Sci. Eng. A.* 385 (2004) 166–174. doi:10.1016/j.msea.2004.06.018.
- [46] E. Kozeschnik, J. Svoboda, F.D. Fischer, Modelling of kinetics in multi-component multi-phase systems with spherical precipitates: II: numerical solution and application, *Mater. Sci. Eng. A.* 385 (2004) 157–165. doi:<https://doi.org/10.1016/j.msea.2004.06.016>.
- [47] E. Kozeschnik, J. Svoboda, F.D. Fischer, Modified evolution equations for the precipitation kinetics of complex phases in multi-component systems, *Calphad Comput. Coupling Phase Diagrams Thermochem.* 28 (2004) 379–382. doi:<https://doi.org/10.1016/j.calphad.2004.11.003>.
- [48] B. Sonderegger, E. Kozeschnik, Generalized nearest-neighbour broken-bond analysis of randomly oriented coherent interfaces in multicomponent fcc and bcc structures, *Metall. Mater. Trans. A.* 40 (2009) 499–510. doi:DOI: 10.1007/s11661-008-9752-6.
- [49] B. Sonderegger, E. Kozeschnik, Size dependence of the interfacial energy in the generalized nearest-neighbour broken-bond approach, *Scr. Mater.* 60 (2009) 635–638. doi:<https://doi.org/10.1016/j.scriptamat.2008.12.025>.
- [50] F.D. Fischer, J. Svoboda, F. Appel, E. Kozeschnik, Modeling of excess vacancy annihilation at different types of sinks, *Acta Mater.* 59 (2011) 3463–3472. doi:10.1016/j.actamat.2011.02.020.
- [51] E. Kozeschnik, J. Svoboda, F.D. Fischer, Shape factors in modeling of precipitation, *Mater. Sci. Eng. A.* 441 (2006) 68–72. doi:10.1016/j.msea.2006.08.088.
- [52] H. Frost, M. Ashby, *Deformation-mechanism maps*, 1st ed., Pergamon Press, Oxford, 1982.
- [53] G. Schoeck, A. Seeger, Defects in Crystalline Solids, in: N. Mott (Ed.), *Rep. Conf. Defects Cryst. Solids*, The Physical Society, London, 1955: p. 340.
- [54] A. Seeger, Work hardening of single crystals, in: J. Fisher, W. Johnston, R. Thompson, J.T. Vreeland (Eds.), *Dislocations Mech. Prop. Cryst.*, Wiley, New York, 1957: p. 243.

- [55] P. Jackson, Dislocation modeling of shear in fcc crystals, *Prog. Mater. Sci.* 29 (1985) 139–175. doi:[https://doi.org/10.1016/0079-6425\(85\)90009-X](https://doi.org/10.1016/0079-6425(85)90009-X).
- [56] P.J. Hurley, F.J. Humphreys, The application of EBSD to the study of substructural development in a cold rolled single-phase aluminium alloy, *Acta Mater.* 51 (2003) 1087–1102. doi:[10.1016/S1359-6454\(02\)00513-X](https://doi.org/10.1016/S1359-6454(02)00513-X).
- [57] N. Hansen, D. Jensen, Development of Microstructure in FCC Metals during Cold Work Author, *Philos Trans Roy Soc.* 357 (1999) 1447–1469. doi:DOI: [10.1098/rsta.1999.0384](https://doi.org/10.1098/rsta.1999.0384).
- [58] N. Hansen, X. Huang, Microstructure and flow stress of polycrystals and single crystals, *Acta Mater.* 46 (1998) 1827–1836. doi:[10.1016/S1359-6454\(97\)00365-0](https://doi.org/10.1016/S1359-6454(97)00365-0).
- [59] Q. Liu, D. Juul Jensen, N. Hansen, Effect of grain orientation on deformation structure in cold-rolled polycrystalline aluminium, *Acta Mater.* 46 (1998) 5819–5838. doi:[10.1016/S1359-6454\(98\)00229-8](https://doi.org/10.1016/S1359-6454(98)00229-8).
- [60] U.F. Kocks, A.S. Argon, M.F. Ashby, *Thermodynamics and Kinetics of Slip*, 1st ed., Pergamon Press, Oxford, 1975. doi:[10.1016/0079-6425\(75\)90009-2](https://doi.org/10.1016/0079-6425(75)90009-2).
- [61] A.D. Rollett, U.F. Kocks, A review of the stages of work hardening, in: *Dislocations* 93, 1993.

## Paper 2

# Analysis of the Temperature and Strain Rate Dependences of Strain Hardening

Johannes Kreyca<sup>a,1\*</sup>, Ernst Kozeschnik<sup>a,2</sup>

<sup>a</sup>Institute of Materials Science and Technology, TU Wien,  
Getreidemarkt 9, 1060, Vienna, Austria

<sup>1</sup>johannes.kreyca@tuwien.ac.at, <sup>2</sup>ernst.kozeschnik@tuwien.ac.at

\*corresponding author

### Abstract

A classical constitutive modeling-based Ansatz for the impact of thermal activation on the stress-strain response of metallic materials is compared with the state parameter-based Kocks-Mecking model. The predicted functional dependencies suggest that, in the first approach, only the dislocation storage mechanism is a thermally activated process, whereas, in the second approach, only the mechanism of dynamic recovery is. In contradiction to each of these individual approaches, our analysis and comparison with experimental evidence shows that thermal activation contributes both to dislocation generation and annihilation.

Physical models describing the stress-strain evolution of a material during plastic deformation [1], [2], [3], [4], [5], [6] are commonly founded on (i) the Taylor equation [7], [8], which relates the stress contribution due to forest hardening, i.e. the true stress,  $\sigma$ , to the average dislocation density,  $\rho$ , as

$$\sigma = \alpha M G b \sqrt{\rho} = g_1 \sqrt{\rho}, \quad (1)$$

where  $M$  is the Taylor factor,  $\alpha$  is the strengthening coefficient,  $G$  is the shear modulus,  $b$  is the Burgers vector,  $g_1 = \alpha M G b$ , and (ii) a differential equation for the average dislocation density evolution in the form

$$\frac{d\rho}{d\varepsilon} = \frac{d\rho^+}{d\varepsilon} - \frac{d\rho^-}{d\varepsilon}. \quad (2)$$

In Eq. (2), the generation of dislocations due to plastic deformation is accounted for in the dislocation storage term,  $d\rho^+/d\varepsilon$ , whereas the annihilation of dislocations due to dynamic recovery is accounted for in the term  $d\rho^-/d\varepsilon = k_2\rho$ . The flow stress,  $\sigma$ , measured in a

polycrystal is related to the critical resolved shear stress,  $\tau$ , through  $\sigma = M\tau$ . The macroscopic plastic strain,  $\varepsilon$ , is related to the algebraic sum of crystallographic shears,  $\gamma$ , according to  $\varepsilon = \gamma/M$  [9]. The storage term is commonly related to the mean free path,  $L$ , of mobile dislocations through [10]

$$\frac{d\rho^+}{d\varepsilon} = \frac{M}{bL} . \quad (3)$$

With the assumption that the mean free path is indirectly proportional to the square root of the dislocation density,

$$L = \frac{A}{\sqrt{\rho}} , \quad (4)$$

Eq (2) delivers the well-known Kocks-Mecking equation [11] reading

$$\frac{d\rho}{d\varepsilon} = k_1\sqrt{\rho} - k_2\rho . \quad (5)$$

Here,  $k_1 = M/bA$  and  $A$  is a proportionality constant. Dynamic recovery was first associated with thermally activated cross slip by Mott [12]. A detailed theory was then developed in refs. [13], [14] concluding that the decreasing strain hardening rate during stage III hardening and its temperature and strain rate-dependence are a result of dynamic recovery due to thermally activated cross-slip. For a detailed review, see [15] and [16].

In most dislocation density-based models [1], [2], [3], [4], [5], [6],  $k_1$  is assumed to be temperature-independent (except for the temperature-dependence of the shear modulus), whereas  $k_2$  is treated as a temperature and strain rate-dependent parameter. The assumption of an athermal  $k_1$  is equivalent to stating that dislocation storage is not a thermally activated process.

Importantly, these two assumptions have severe implications on the shape of the modelled stress-strain curves. Within the Kocks-Mecking framework, this shape is characterized by the initial strain hardening rate,  $\theta_0$ , the saturation stress,  $\sigma_\infty$ , and the critical strain,  $\varepsilon_c$ . These quantities are fundamentally related to  $k_1$  and  $k_2$  [17] through

$$\theta_0 = \frac{g_1 k_1}{2} , \quad (6)$$

$$\sigma_\infty = \frac{g_1 k_1}{k_2} , \quad (7)$$

$$\varepsilon_c = \frac{\theta_0}{\sigma_\infty} = \frac{k_2}{2} . \quad (8)$$

The hardening coefficient,  $\alpha$ , is sometimes assumed to be a function of temperature and strain rate, e.g. in [11], however, most commonly  $\alpha$  is assumed to be a constant, rendering the initial strain hardening rate,  $\theta_0$ , athermal. As a consequence, many state parameter-based models, e.g. [6], [4], [5], [1] predict an athermal initial strain hardening rate and only the saturation stress and the critical strain, Eqs. (7) and (8), are functions of temperature and strain rate. This specific case is further denoted as Case 1.

Comparison with experiment, Fig. 1 (a) and (b), shows, however, that the initial strain hardening rate shows considerable strain rate and temperature-dependence in several different materials. This dependency appears quite prominently even when normalized by the temperature-dependent shear modulus, showing that the well-known temperature-dependence of  $G$  cannot explain this observation alone.

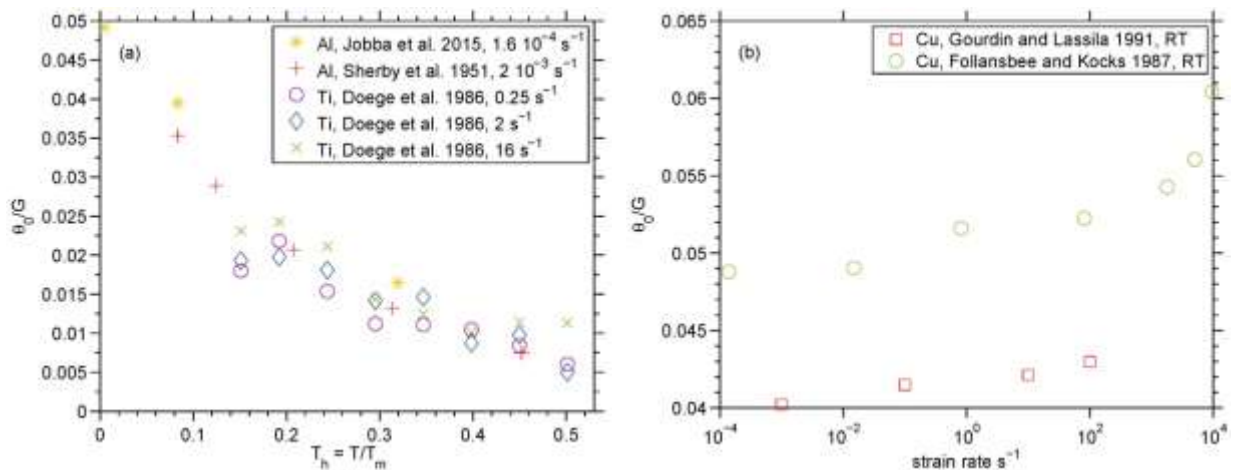


Fig. 1 Initial strain hardening rate normalized by the shear modulus,  $G$ , over (a) temperature for Al and Ti and (b) over strain rate for copper. Values for Cu [18], [19] and Al [20] are taken directly taken from literature. The values for Al [21] and Ti [22] are derived from a Kocks-plot of the published stress-strain curves.

In constitutive models, it is common to express the temperature and strain rate dependence of the stress as

$$\sigma(T, \dot{\epsilon}) = f(T, \dot{\epsilon}) \cdot \sigma_{\text{ref}}(\epsilon), \quad (9)$$

which comprises the product of a *strain*-dependent master-curve,  $\sigma_{\text{ref}}(\epsilon)$ , and a *temperature* and *strain rate*-dependent function,  $f(T, \dot{\epsilon})$ . Table 1 summarizes the functional dependence of a selection of constitutive models and indicates whether they are following the “product form” Eq. (9) or not.

Table 1. Overview of constitutive models for flow curves with different degree of complexity

Source	Eqs.	product form
[24], [25]	$\sigma = \sigma_0 + k\varepsilon^n$	no
[26]	$\sigma = A \cdot e^{m_1 T} \cdot \varepsilon^{m_2} \cdot e^{m_4/\varepsilon} \cdot \dot{\varepsilon}^{m_3}$	yes
[26]	$\sigma = A \cdot e^{m_1 T} \cdot \varepsilon^{m_2} \cdot e^{m_4/\varepsilon} \cdot (1 + \varepsilon)^{m_5 T} \cdot e^{m_7 \varepsilon} \cdot \dot{\varepsilon}^{m_3 T}$	yes
[27]	$\sigma = (A + B\varepsilon^n) \left( 1 + C \ln(\dot{\varepsilon}/\dot{\varepsilon}_0) \right) \left( 1 - \left[ \frac{T_m - T}{T_m - T_r} \right]^m \right)$	yes
[28]	$\sigma = c_0 + B_0 e^{-(\beta_0 - \beta_1 \ln \dot{\varepsilon})T} + k\varepsilon^n$	no
[29]	$\sigma = \left( \sigma_0 + E_\infty \varepsilon - a e^{-a\varepsilon} \left( 1 - \frac{\ln(\dot{\varepsilon})}{\ln(D_0)} \right) \right)^{-n}$	yes
[30]	$\sigma = \left[ A + B\varepsilon^{n_0} \left( 1 - \frac{\ln \dot{\varepsilon}}{\ln D_p} \right)^{n_1} \right] \left[ \frac{\dot{\varepsilon}}{\dot{\varepsilon}^*} \right]^C \left[ \frac{T_m - T}{T_m - T_r} \right]^m$	yes

When accepting that the stress follows the multiplicative dependency described by Eq. (9), the corresponding derivative quantity,  $\theta_0$ , as well as the saturation stress,  $\sigma_\infty$ , must also follow the same functional dependence  $f(T, \dot{\varepsilon})$ , i.e.,  $\theta_0 = \hat{\theta}_0 \cdot f(T, \dot{\varepsilon})$  and  $\sigma_\infty = \hat{\sigma}_\infty \cdot f(T, \dot{\varepsilon})$ , where  $\hat{\theta}_0$  and  $\hat{\sigma}_\infty$  are independent of temperature and strain rate. The initial strain hardening rate as well as the saturation stress are consequently functions of temperature and strain rate. The critical strain,  $\varepsilon_c = \hat{\theta}_0 / \hat{\sigma}_\infty$ , as a function of the athermal quantities  $\hat{\theta}_0$  and  $\hat{\sigma}_\infty$ , is athermal (Case 2).

Fig. 2 shows schematic stress-strain curves and Kocks-plots obtained from the Kocks-Mecking model, according to Case 1 (solid lines) and Case 2 (dashed lines). Both concepts are assuming one characteristic quantity to be independent of temperature and strain rate. In the first case, it is the initial strain hardening rate,  $\theta_0$ , which is an athermal quantity according to the arguments presented earlier in discussion of Eq. (6). In the second case, it is the critical strain,  $\varepsilon_c$ , which is an inherently athermal quantity as derived before. We emphasize, however, that both assumptions represent simplifications and, in experiment, all three quantities,  $\sigma_\infty$ ,  $\theta_0$  and  $\varepsilon_c$ , might exhibit some specific dependency on temperature and strain rate.

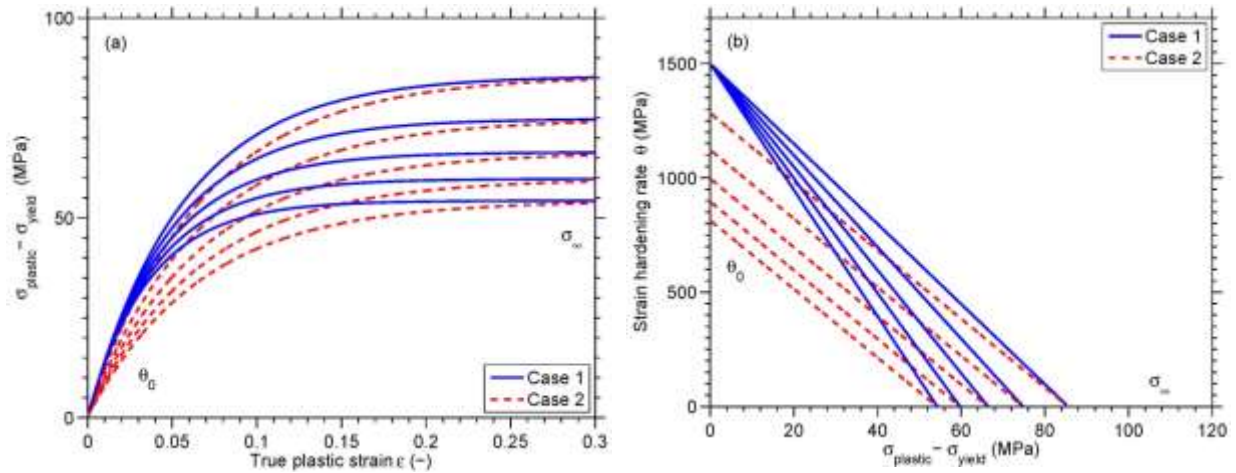


Fig. 2 (a) schematic stress-strain curves with stage III hardening, and (b) corresponding Kocks-plots, generated with the Kocks-Mecking model, according to Case 1 (solid lines) and Case 2 (dashed lines).

When finally integrating the simplification commonly utilized in constitutive models to a Kocks-Mecking dislocation density evolution-based approach, either  $g_1$  or  $k_1$  must depend on temperature and strain rate and  $k_2$  must be constant. If  $g_1$  is assumed to be a function of temperature and strain rate, as is the case in Refs. [23] and [3], the dislocation density evolution becomes independent of temperature and strain rate, which is in contradiction to experimental evidence. If, however,  $k_1$  is assumed to be a thermally activated quantity, the dislocation density evolution depends on temperature and strain rate in all cases. Dislocation storage should thus also be treated as a thermally activated process, at least to some extent.

These observations have two implications, one for constitutive modelling and one for the understanding of physical mechanisms. For constitutive modelling, these results suggest that the temperature and strain rate-dependence of  $\theta_0$  observed in experiment should be taken into account by a temperature-dependence of  $k_1$ . In terms of physical understanding, these results mean that the temperature and strain rate-dependence of plastic deformation is not sufficiently explained solely by dynamic recovery due to thermally activated cross-slip; and that the dislocation storage term may well be thermally activated and need further and appropriate consideration in this type of modelling.

### Acknowledgements

This research did not receive any specific grant from funding agencies in the public, commercial, or not-for-profit sectors.

- 1 U.F. Kocks: *J. Eng. Mater. Technol.*, 1976, pp. 76–85.
- 2 L.P. Kubin and Y. Estrin: *Acta Metall.*, 1990, vol. 38, pp. 697–708.
- 3 Y. Estrin: in *Unified Constitutive laws of plastic deformation*, A.S. Krausz and K. Krausz, eds., Academic Press, Inc., New York City, 1996, pp. 69–106.
- 4 E.I. Galindo-Nava, J. Sietsma, and P.E.J. Rivera-Díaz-Del-Castillo: *Acta Mater.*, 2012, vol. 60, pp. 2615–24.
- 5 E. Nes: *Prog. Mater. Sci.*, 1997, vol. 41, pp. 129–93.
- 6 F. Roters, D. Raabe, and G. Gottstein: *Acta Mater.*, 2000, vol. 48, pp. 4181–9.
- 7 G.I. Taylor: *Proc. R. Soc. A Math. Phys. Eng. Sci.*, 1934, vol. 145, pp. 362–87.
- 8 M. Sauzay and L.P. Kubin: *Prog. Mater. Sci.*, 2011, vol. 56, pp. 725–84.
- 9 H. Mecking, U.F. Kocks, and C. Hartig: *Scr. Mater.*, 1996, vol. 35, pp. 465–71.
- 10 F. Barlat, M. V. Glazov, J.C. Brem, and D.J. Lege: *Int. J. Plast.*, 2002, vol. 18, pp. 919–39.
- 11 U.F. Kocks and H. Mecking: *Prog. Mater. Sci.*, 2003, vol. 48, pp. 171–273.
- 12 N. Mott: *Philos. Mag.*, 1952, vol. 43, p. 1151.
- 13 G. Schoeck and A. Seeger: in *Report of the Conference on Defects in Crystalline Solids*, N. Mott, ed., The Physical Society, London, 1955, p. 340.
- 14 A. Seeger: in *Dislocations and Mechanical Properties of Crystals*, J. Fisher, W. Johnston, R. Thompson, and J.T. Vreeland, eds., Wiley, New York, 1957, p. 243.
- 15 P. Jackson: *Prog. Mater. Sci.*, 1985, vol. 29, pp. 139–75.
- 16 W. Püschl: *Prog. Mater. Sci.*, 2002, vol. 47, pp. 415–61.
- 17 A. Simar, Y. Brechet, B. de Meester, A. Denquin, C. Gallais, and T. Pardoen: *Prog. Mater. Sci.*, 2012, vol. 57, pp. 95–183.
- 18 W. Gourdin and D. Lassila: *Acta Metall. Mater.*, 1991, vol. 39, pp. 2337–48.
- 19 P.S. Follansbee and U.F. Kocks: *Acta Metall.*, 1988, vol. 36, pp. 81–93.
- 20 M. Jobba, R.K. Mishra, and M. Niewczas: *Int. J. Plast.*, 2015, vol. 65, pp. 43–60.
- 21 O.D. Sherby, R.A. Anderson, and J.E. Dorn: *J. Met.*, 1951, vol. 3, pp. 643–52.
- 22 E. Doege, H. Meyer-Nolkemper, and I. Saeed: *Fliesskurvenatlas Metallischer Werkstoffe*, Carl Hanser Verlag, München, Wien, 1986.
- 23 Y. Estrin and H. Mecking: *Acta Metall. Mater.*, 1984, vol. 32, pp. 57–70.
- 24 P. Ludwik: *Elemente Der Technologischen Mechanik*, Springer, Berlin, 1909.
- 25 J. Hollomon: *Trans. AIME*, 1945, vol. 162, pp. 268–90.
- 26 M. Schmidtchen and M. Spittel: in *MEFORM 2011 Werkstoffkennwerte für die Simulation von Umformprozessen*, 2011, pp. 35–64.
- 27 G.R. Johnson and W.H. Cook: in *Proceedings of the Seventh International Symposium on Ballistic*, 1983, pp. 541–7.
- 28 F. Zerilli and W. Armstrong: *J. Appl. Phys.*, 1987, vol. 61, pp. 1816–25.
- 29 A. Khan and S. Huang: *Int. J. Plast.*, 1992, vol. 8, pp. 397–424.
- 30 A. Khan and R. Liang: *Int. J. Plast.*, 1999, vol. 15, pp. 1089–109.

# State parameter-based constitutive modelling of stress strain curves in Al-Mg solid solutions

Johannes Kreyca<sup>a,1\*</sup>, Ernst Kozeschnik<sup>a,2</sup>

<sup>a</sup>*Institute of Materials Science and Technology, TU Wien,  
Getreidemarkt 9, Vienna, 1060, Austria*

<sup>1</sup>*johannes.kreyca@tuwien.ac.at*, <sup>2</sup>*ernst.kozeschnik@tuwien.ac.at*

*\*corresponding author*

## Abstract

A novel and comprehensive approach addressing the stress strain response of binary Al-Mg alloys under uniaxial loading over a wide range of temperatures (78K-500K), strain rates ( $10^{-4}$ - $10^1$  s<sup>-1</sup>) and solute contents (0 wt.%-5 wt.%) is developed and introduced. The model is based on the mechanical threshold Ansatz in combination with a Labusch type solid solution hardening approach and a model for dynamic strain ageing to describe the temperature and strain rate dependence of the yield stress in a thermal activation framework. Strain hardening is modelled on basis of the Kocks-Mecking evolution equations for the average dislocation density and discussed in terms of the temperature-dependence of the initial strain hardening rate and the saturation stress for stage-III hardening. Both, static and dynamic recovery, are fully taken into account. The model predictions are validated on experimental stress-strain curves reported in literature. The results demonstrate that the model successfully reproduces the complex temperature and strain rate dependent plastic deformation characteristics of Al-Mg alloys with a minimum of calibration input parameters.

**Keywords:** dislocations A, strengthening mechanisms A, constitutive behavior B, polycrystalline material B, analytical functions C

## 1. Introduction

Magnesium ranks among the most important alloying elements in Al-alloys. Its outstanding potential to improve the mechanical properties of Al-alloys stem from a combination of high solubility and misfit strain leading to considerable solid solution hardening in 5xxx alloys and

its capability of forming precipitates with other alloying elements such as, e.g., Si in 6xxx alloys. Unfortunately, forming processes of Al-Mg-X alloys are complicated by the effect of dynamic strain ageing (DSA) in certain temperature and strain rate regions, which can lead to negative strain rate sensitivity, serrated flow and decreased ductility. This combination of high industrial relevance and complex underlying physical processes has fostered great scientific interest and has led to numerous publications on plastic deformation of aluminium alloys. Creep of aluminium alloys, e.g., was investigated by (Li et al., 1997). (Hu et al., 2016) presented a crystal plasticity extended models for the tensile behaviour of aluminium alloys. The variation of strain rate sensitivity of an aluminium alloy in a wide strain rate range was studied by (Yan et al., 2016). Cyclic plasticity and the Bauschinger effect were subject to investigations by (Yoshida and Uemori, 2002). Dislocation density based models on strain hardening were recently introduced by (Csanadi et al., 2014), (Silbermann et al., 2014) and (Bertin et al., 2013). The formability of AA5083 and AA6061 was investigated through experimentation by (Liu et al., 2010). High-velocity impact failure of 6061-T6 aluminum was investigated by (Ahad et al., 2014) and shock wave propagation in Al single and polycrystals by (Lloyd et al., 2014). Damage models were subject to the work of (Mengoni and Ponthot, 2015) and (Tutyshkin et al., 2014). Yield surface evolution in AA6061 and annealed 1100 Al was presented by (Khan et al., 2009), (Khan et al., 2010a), (Khan et al., 2010b) and (Pandey et al., 2013). The anisotropic behaviour in AA 2090-T3 aluminium alloy was studied by (Safaei et al., 2014).

Some of these applications, e.g., finite element simulations, require material properties in the form of flow curves as input data, where even small variations of the input data can cause big deviations in the resulting simulation (Umbrello et al., 2007). Traditionally such data is obtained through experimentation, which is expensive and time-consuming. A reduction of experimental cost by combining experiment with the simulation of flow-curve data is thus highly desirable. Subject of the present contribution is the simulation of the flow curve of Al-Mg binary alloys as a function of temperature, strain rate and solute content. For this purpose existing constitutive models are reviewed briefly, followed by an introduction of the physical concepts necessary for the construction of the present model. Finally, the model is calibrated for Al-Mg alloys and utilized to simulated experimental data on flow curves in Al-(0-5wt%)Mg.

## 2. State of the art

Early constitutive stress-strain models date back to (Ludwik, 1909) and (Hollomon, 1945) and are commonly written in the form of a power law,  $\sigma = \sigma_0 + K\varepsilon^{n_L}$ , where  $\sigma_0$  is the initial yield stress,  $K$  is a constant and  $n_L$  is the hardening exponent. All three parameters are straightforwardly derived from a double logarithmic plot of stress over strain. A dependence on temperature and strain rate can be introduced by multiplying the power law expression with a function  $f(T, \dot{\varepsilon})$  of temperature,  $T$ , and strain rate,  $\dot{\varepsilon}$ . Constitutive power-law models for stress-strain curves are numerous and broadly applied in the field of finite element simulation, e.g. (Schmidtchen and Spittel, 2011), (Johnson and Cook, 1983), (Zerilli and Armstrong, 1987), (Khan and Huang, 1992), (Khan and Liang, 1999), (Chinh et al., 2004), (Farrokh and Khan, 2009), (Csanadi et al., 2011). Although constitutive models have been successfully applied to describe experimentally observed stress strain curves, the number of fitting parameters in these approaches is often fairly high in comparison to the physical insight that these models provide.

State parameter-based models, such as the ones from (Kocks, 1976), (Estrin and Mecking, 1984), (Kubin and Estrin, 1990), (Estrin, 1996), (Nes, 1997), (Roters et al., 2000), (Marthinsen and Nes, 2001), (Barlat et al., 2002), (Tóth et al., 2002), (Beyerlein and Tome, 2007), (Austin and McDowell, 2011), (Fan and Yang, 2011), (Gao and Zhang, 2012), (Galindo-Nava et al., 2012), (Hansen et al., 2013), (Bertin et al., 2013), (Li et al., 2014), offer more physical insight and give access to observable parameters, such as, the dislocation density or the subgrain evolution.

Power-law and state parameter-based models do have in common that the total yield stress,  $S$ , is commonly represented by the sum of a strain-independent initial yield stress,  $\sigma_0$ , and a strain-dependent stress,  $\sigma_p$ , also referred to as the plastic stress, as

$$\sigma = \sigma_0 + \sigma_p \quad (1)$$

This latter approach is pursued in the present work. For this purpose, the model for the initial yield stress,  $\sigma_0$ , is introduced in the next section, based on the concepts of a mechanical threshold stress and a thermal activation framework. In the subsequent section, a dislocation density-based model for the calculation of the plastic stress,  $\sigma_p$ , is presented based on an analysis of the strain hardening rate  $\theta = d\sigma/d\varepsilon$  and the saturation stress,  $\sigma_\infty$ , see also (Kreyca and Kozeschnik, 2017). In a final section, the calibration procedure of the present model for Al-Mg binary alloys is outlined and the results are discussed. It should be

emphasized that the present model only refers to stage-III hardening. Fig. 1 shows a schematic view of a generic stress-strain curve depicting  $\sigma_0$  and  $\sigma_p$ , where also the initial strain hardening rate,  $\theta_0$ , the saturation stress,  $\sigma_\infty$ , and the critical strain,  $\varepsilon_c = \theta_0/\sigma_\infty$ , are displayed.

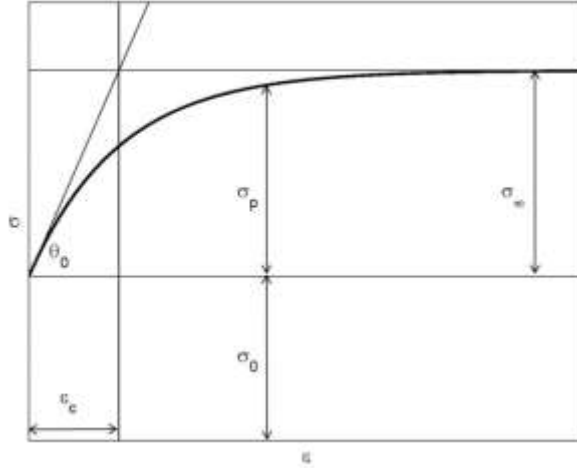


Fig. 1 Schematic representation of a stress strain curve with stage III hardening.

### 3. Initial yield stress $\sigma_0$

The calculation of the initial yield stress is based on the concept of the mechanical threshold stress (MTS) and a thermal activation framework. The mechanical threshold stress,  $\hat{\sigma}$ , represents the yield stress at 0K (for a detailed review see (Kocks et al., 1975)). It has been successfully applied to aluminium alloys (Leyson and Curtin, 2016), (Soare and Curtin, 2008a), (Kocks and Mecking, 2003). The MTS is independent of temperature and strain rate as long as the basic quantities describing the constitution of the microstructure, e.g. solute content, precipitation state and grain size etc., are independent of temperature and strain. Two contributions are considered in the present MTS formulation,

$$\hat{\sigma} = \hat{\sigma}_b + \hat{\sigma}_{ss} , \quad (2)$$

where  $\hat{\sigma}_{ss}$  comprises all strengthening contributions from Mg solute atoms including dynamic strain ageing and  $\hat{\sigma}_b$  includes all contributions, which are not directly related to Mg solute atoms, e.g., the basic yield stress from pure Al, grain boundary strengthening and solid solution hardening from other impurity elements.  $\hat{\sigma}_b$  is treated as a temperature and strain rate-independent calibration parameter in the present work.

#### 3.1. MTS contribution from solute atoms $\hat{\sigma}_{ss}$

At temperatures, where solute atoms are essentially immobile, the calculation of the MTS

contribution,  $\hat{\sigma}_{ss}$ , depends on mostly geometrical parameters, which are, in the present analysis, the solute spacing  $b/c_0^{1/2}$ , the interaction distance between a solute and a dislocation,  $w$ , the maximum elementary interaction force,  $f_{\max}$ , the dislocation line tension,  $E_L = Gb^2/2$  (Haasen, 1996), and the linear misfit strain,  $\varepsilon_m$ . Here,  $G$  is the temperature-dependent shear modulus,  $b$  is the Burgers vector and  $c_0$  the nominal composition. For fcc solid solutions, an approach based on Labusch's work (Labusch, 1970) is adopted here with

$$\hat{\sigma}_{ss} = \left( \frac{f_{\max}^4 c_0^2 w}{8E_L b^7} \right)^{1/3} = \left( \frac{f_{\max}^4 c_0^2 w}{4Gb^9} \right)^{1/3} \quad (3)$$

and

$$f_{\max} = \frac{\sqrt{3}}{2} \left( \frac{1+\nu}{1-\nu} \right) Gb^2 |\varepsilon_m| \quad (4)$$

A value of  $w = 5b$  (Kato, 1999) is used as derived from comparison with experimental results (Uesugi and Higashi, 2013). The misfit strain,  $\varepsilon_m$ , can be obtained experimentally (King, 1966) or from first principles (Uesugi and Higashi, 2013).

### 3.2. Dynamic strain ageing and negative strain rate sensitivity

At higher temperatures, where solute atoms become increasingly mobile, the strength contribution from solute atoms can become highly sensitive to temperature and strain rate, occasionally leading to negative strain rate sensitivity. In the case of negative strain rate sensitivity, plastic deformation becomes unstable and results in jerky flow that is unwelcome during industrial forming processes and is commonly referred to as Portevin Le-Chatelier (PLC) effect. This effect is known to heavily affect the mechanical properties of solid solution hardening alloys, such as 5xxx-series Al alloys (Kabirian et al., 2014), (Manach et al., 2014), (Picu et al., 2005) and (Picu et al., 2006). For a review on experimental findings, see (Sherby et al., 1952), (Yilmaz, 2011) and (Jobba et al., 2015). (Tensi et al., 1972) investigated the PLC effect in Al-Mg single crystals. Theoretical work on the effect was published by (Mulford and Kocks, 1979), (Louat, 1981), (Kubin and Estrin, 1990), (Penning, 1972), (Zaiser et al., 1999), (Glazov et al., 1999), (Hähner, 1996a), (Hähner, 1996b). Models on dynamic strain ageing were published by (Fressengeas et al., 2005), (Soare and Curtin, 2008a), (Soare and Curtin, 2008b), (Leyson et al., 2010), (Leyson et al., 2012) and (Keralavarma et al., 2014).

For the sake of simplicity, dynamic strain ageing and low temperature solid solution hardening is represented by a single state parameter in the present work. This state

parameter is referred to as effective solute concentration,  $c_{\text{eff}}$ , and it is calculated according to the model of (Curtin et al., 2006) as

$$c_{\text{eff}} = c_0 + c_0 \tanh\left(\frac{\Delta W}{2kT}\right) \left[ 1 - \exp\left(\left(-6 \cosh\left(\frac{\Delta W}{2kT}\right) \Gamma_c \frac{\Omega}{\dot{\epsilon}}\right)^n\right)\right] \quad (5)$$

where  $\Omega = b\rho^{1/2}$  is the incremental strain,  $\rho$  is the dislocation density,  $\Gamma_c = \nu_0 \exp(-\Delta H_c/kT)$  is a reference core transition rate,  $\Delta W$  is the average binding energy difference between tension and compression sites,  $\Delta H_c$  is the average activation enthalpy for transitions between these sites,  $\nu_0$  is an attempt frequency,  $k$  is the Boltzmann constant and  $n$  is an exponent. It must be emphasized that transient effects occurring as a consequence of instantaneous strain rate or temperature jumps (McCormick, 1988) are not captured by Eq. (5) and are out of the scope of the present work. The combined effect of solid solution hardening and DSA are finally calculated by using  $c_{\text{eff}}$  instead of  $c_0$  for the calculation of  $\hat{\sigma}_{\text{ss}}$  in Eq. (3).

### 3.3. Thermal activation framework

Purpose of the thermal activation framework is to relate the applied external stress,  $\sigma_0$ , to the mechanical threshold stress,  $\hat{\sigma}$ , temperature  $T$ , strain rate  $\dot{\epsilon}$  and the effective solute concentration,  $c_{\text{eff}}$ . The applied stress is related to the strain rate through the combination of the Orowan equation (Orowan, 1940) and an Arrhenius Ansatz (Argon, 1996), (Kocks et al., 1975) with

$$\dot{\epsilon} = \dot{\epsilon}_0 \cdot \left[ \exp\left(-\frac{\Delta G_f(\sigma)}{kT}\right) - \exp\left(-\frac{\Delta G_b(\sigma)}{kT}\right) \right], \quad (6)$$

where  $\Delta G_f$  is the Gibbs energy for a thermal activation event in direction of the applied stress and  $\Delta G_b$  is the Gibbs energy for thermal activation against the direction of the applied stress.  $\dot{\epsilon}_0$  is a pre-exponential factor, which is assumed to be constant (Follansbee and Kocks, 1988). According to (Galindo-Nava and Rivera-Díaz-del-Castillo, 2012) it can be approximated by  $\dot{\epsilon}_0 = \rho_0 b c$ , where  $\rho_0$  is the initial dislocation density and  $c$  is the velocity of sound.

#### 3.3.1. Low temperature deformation

At low temperature or high stresses,  $\Delta G_b \gg \Delta G_f$  and, therefore, the second exponential term in Eq. (6) can be neglected. Eq. (6) can then be simplified as

$$\dot{\varepsilon} = \dot{\varepsilon}_0 \cdot \exp\left(-\frac{\Delta G_f(\sigma)}{kT}\right) \quad (7)$$

In practice, it is common to assume a certain obstacle profile from which a functional relationship between  $\Delta G_f$  and  $S$  can be derived (Kocks et al., 1975), (Dahl and Krabiell, 1979), (Burgahn et al., 1996), (Schulze and Vohringer, 2000), (Leyson and Curtin, 2016), (Soare and Curtin, 2008b), (Leyson et al., 2010). In the present work, we assume a hyperbolic obstacle profile according to (Kocks and Mecking, 2003). The relation between  $\Delta G_f$ , the mechanical threshold,  $\hat{\sigma}$ , and the applied stress,  $\sigma$ , then follows from the obstacle profile as  $\Delta G_f = \Delta F_0^{lt} \cdot \ln(\hat{\sigma}/\sigma)$ , where  $\Delta F_0^{lt}$  is the energy for a dislocation to overcome an obstacle in the absence of thermal activation. Together with Eq. (7), this delivers the applied stress as a function of temperature, strain rate and mechanical threshold with

$$\sigma_0^{lt} = \hat{\sigma} \exp\left(-\frac{kT}{\Delta F_0^{lt}} \ln(\dot{\varepsilon}_0/\dot{\varepsilon})\right) = \hat{\sigma} \left(\frac{\dot{\varepsilon}_0}{\dot{\varepsilon}}\right)^{-\frac{kT}{\Delta F_0^{lt}}} \quad (8)$$

### 3.3.2. High temperature deformation

At high temperatures or low stresses, both exponential terms in Eq. (6) must be considered in the analysis. With the assumption of a box-shaped obstacle profile, the Gibbs energy contributions can be linearized as

$$\Delta G_f = \Delta F_0^{ht} - \Delta W_0 \quad (9)$$

and

$$\Delta G_b = \Delta F_0^{ht} + \Delta W_0, \quad (10)$$

where  $\Delta F_0^{ht}$  is the Helmholtz energy, i.e. the energy that must be supplied in the absence of any thermal activation, and  $\Delta W_0$  is the applied external work. As a consequence of the box-shaped obstacle profile, the applied work is related to the Helmholtz energy through  $\Delta W_0 = \Delta F_0^{ht} \cdot \sigma/\hat{\sigma}$ . The linearization of  $\Delta G_f$  and  $\Delta G_b$ , according to Eqs. (9) and (10), allows for a rearrangement of Eq. (6) leading to

$$\dot{\varepsilon} = 2\dot{\varepsilon}_0 \exp\left(-\frac{\Delta F_0^{ht}}{kT}\right) \sinh\left(\frac{\Delta W_0}{kT}\right). \quad (11)$$

At high temperatures or low stresses,  $\Delta W_0/kT \ll 1$  and, consequently, Eq.(11) can be written as

$$\dot{\varepsilon} = 2\dot{\varepsilon}_0 \frac{\Delta W_0}{kT} \exp\left(-\frac{\Delta F_0^{ht}}{kT}\right). \quad (12)$$

This results in a rate equation for the strain rate at high temperatures reading

$$\dot{\varepsilon} = 2b\rho c \left( \frac{\sigma}{\hat{\sigma}} \right) \frac{\Delta F_0^{\text{ht}}}{kT} \exp\left( -\frac{\Delta F_0^{\text{ht}}}{kT} \right) \quad (13)$$

Applying the Taylor equation,  $\sigma = \alpha bGM\sqrt{\rho}$ , on the mobile dislocation density delivers an expression for the yield stress at elevated temperatures as

$$\sigma_0^{\text{ht}} = \left( \hat{\sigma} \frac{\dot{\varepsilon} k T (\alpha b G M)^2}{2bc \Delta F_0^{\text{ht}} \exp(-\Delta F_0^{\text{ht}}/kT)} \right)^{1/3}, \quad (14)$$

where  $M$  is the Taylor factor and  $\alpha$  is the so-called strengthening coefficient (Sauzay and Kubin, 2011). It should be emphasized that Eq. (14) is equivalent to a power law creep model with a creep exponent of 3, however, in dependence of the mechanical threshold. In Al-Mg, a creep exponent of 3 is in accordance with experimental creep data (Kocks, 1998), (Brown and Ashby, 1980). Power-law creep models have been successfully applied to aluminium alloys previously, e.g. (McQueen and Ryan, 2002), (McQueen et al., 2001), (Spigarelli et al., 2003), (El-Danaf et al., 2008a), (El-Danaf et al., 2008b).

The low and high temperature regions are treated separately in the present work with a low  $\sigma_0^{\text{lt}}$  and high  $\sigma_0^{\text{ht}}$  temperature asymptote. The entire temperature range is finally described by

$$\frac{1}{S_0} = \frac{1}{S_0^{\text{lt}}} + \frac{1}{S_0^{\text{ht}}}. \quad (15)$$

In the following chapter, the strain-dependent plastic stress is addressed in more detail.

#### 4. Plastic stress $\sigma_p$

In this chapter, the model for the plastic stress,  $\sigma_p$ , and its calibration on basis of experimental data is introduced.

##### 4.1. Strain hardening model

For the calculation of the strain-dependent stress contribution, we apply a Kocks Mecking type model. The Kocks-Mecking (KM) model ((Kocks, 1976), (Mecking and Kocks, 1981), see also (Gil Sevillano et al., 1981)), is a dislocation density-based state parameter model describing the evolution of stress as a function of the strain hardening rate,  $\theta$ . It has previously been successfully applied to simulate strain hardening in Al alloys by (Cheng et al., 2003), (Esmaeili et al., 2001), (Fribourg et al., 2011), (Deschamps et al., 1996) and (Deschamps et al., 2000). The outstanding success of the KM-model is certainly due to its conceptual simplicity and the careful selection of two semi-empirical expressions that have fundamental

relevance in the theory of plastic deformation.

The first expressions in this context is the Taylor relation (Taylor, 1934), which correlates the plastic stress,  $\sigma_p$ , with an average dislocation density,  $\rho$ , as

$$\sigma_p = \alpha M G b \sqrt{\rho} = g_1 \sqrt{\rho}. \quad (16)$$

The second basic relation is the differential form of the constitutive Voce work-hardening law (Voce, 1955) reading

$$\theta = \frac{d\sigma_p}{d\varepsilon} = \theta_0 \left( 1 - \frac{\sigma_p}{\sigma_\infty} \right). \quad (17)$$

This relation emphasizes a linear relation between the strain hardening rate,  $\theta$ , and the plastic stress contribution,  $\sigma_p$ . Eqs. (16) and (17) together deliver the well-known Kocks-Mecking law, which represents an evolution equation for the dislocation density with

$$\frac{d\rho}{d\varepsilon} = \frac{2\theta_0}{g_1} \sqrt{\rho} - \frac{2\theta_0}{\sigma_\infty} \rho. \quad (18)$$

Alternatively, Eq. (18) can be derived from consideration of the mechanisms of dislocation generation, immobilization and dynamic recovery (Kocks, 1976) yielding

$$\frac{\partial \rho}{\partial \varepsilon} = \frac{d\rho^+}{d\varepsilon} + \frac{d\rho_d^-}{d\varepsilon} = \frac{M}{bA} \sqrt{\rho} - 2BM \frac{d_{\text{crit}}}{b} \rho, \quad (19)$$

where the first term on the rhs of this equation is further denoted as “A-term”, due to the calibration coefficient  $A$ , the second term likewise as “B-term”. The subscript “d” emphasizes that the dislocation annihilation term refers to dynamic recovery.  $d_{\text{crit}}$  is the critical annihilation distance between two dislocations (Brinckmann et al., 2011) given as

$$d_{\text{crit}} = \frac{Gb^4}{2\pi(1-\nu)Q_{\text{vac}}}, \quad (20)$$

where  $Q_{\text{vac}}$  is the vacancy formation energy and  $\nu$  is Poisson’s ratio. The coefficient  $A$  is closely related to the number of immobile dislocations that a moving dislocation can surpass before it becomes arrested. The coefficient  $B$  represents the inverse of the probability of a dislocation to become annihilated under the condition of having a second dislocation within the critical distance.

At elevated temperature, the evolution of dislocation density becomes additionally impacted by vacancy-assisted dislocation climb. To incorporate this mechanism in a general model of strain hardening based on dislocation generation and annihilation, an additional annihilation

term for static recovery might be introduced into Eq.(19) with

$$\frac{d\rho_s^-}{d\varepsilon} = -2CD_d \frac{Gb^3}{\dot{\varepsilon}kT} (\rho^2 - \rho_{eq}^2), \quad (21)$$

where the rhs of this equation will be further denoted as “C-term”, due to the calibration coefficient  $C$ , and the subscript “s” emphasizing that this dislocation annihilation term refers to static recovery.  $\rho_{eq}$  is the equilibrium dislocation density and  $D_d = D_{d0} \exp(Q_d/RT)$  is the diffusion coefficient along dislocation pipes. This recovery term has been introduced by (Lagneborg, 1972) for creep and it is used in a similar form, for instance, by (Sommitsch, 1999), (Krumphals et al., 2009) and (Lindgren et al., 2008). Eq. (21) extends the yield stress model for glide and thermally activated cross-slip Eq. (19) into the high-temperature deformation region dominated by vacancy-assisted dislocation climb.

#### 4.2. Calibration of the strain hardening model

The present strain hardening model is fully calibrated if the quantities  $A$ ,  $B$  and  $C$  are determined. On closer inspection of the relations presented in the previous sections,  $A$ ,  $B$  and  $C$  are related to the initial strain hardening rate and the saturation stress, which can be derived directly from experiment, through

$$A = \frac{\alpha GbM^2}{2b\theta_0} \quad (22)$$

$$B = \frac{b\theta_0}{M\sigma_\infty^{lt}d_{crit}} \quad (23)$$

$$C = \frac{2b\theta_0}{\alpha GbM^2} \quad (24)$$

In the following,  $\theta_0$  and  $\sigma_\infty$  are derived from experiments as a function of temperature and solute concentration. Constitutive equations are used to model these experimental findings, resulting in expressions for  $\theta_0 = \theta_0(T, \dot{\varepsilon}, c_0)$  and  $\sigma_\infty = \sigma_\infty(T, \dot{\varepsilon}, c_0)$ . These expressions are then used to calculate expressions for  $A$ ,  $B$  and  $C$  according to Eqs. (22)-(24) and, finally, to derive  $\sigma_p$  on the basis of Eqs. (16-21). This approach is advantageous because  $\theta_0$  and  $\sigma_\infty$  are directly accessible from experiment, which is not the case for  $A$ ,  $B$  and  $C$ . In addition, rather simple expressions for  $\theta_0$  and  $\sigma_\infty$  as functions of temperature, strain rate and effective solute content are obtained. Table 1 summarizes the expressions used for

modelling  $\theta_0$  and  $\sigma_\infty$  as a function of temperature, strain rate and effective solute content. Expressions for  $\sigma_0$ , as derived in section (3), are also shown in Table 1.

	low temperature	high temperature	summation
$\sigma_0$	$\sigma_0^{\text{lt}} = \hat{\sigma}_0 \exp\left(-\frac{kT \ln(\dot{\epsilon}_0/\dot{\epsilon})}{\Delta F_{\theta_0}^{\text{lt}}}\right)$	$\sigma_0^{\text{ht}} = \left(\frac{\hat{\sigma}_0 g_1^2 \dot{\epsilon} k T}{2bc \exp(-\Delta F_{\sigma_0}^{\text{ht}}/kT) \Delta F_{\sigma_0}^{\text{ht}}}\right)^{1/3}$	$\frac{1}{\sigma_0} = \frac{1}{\sigma_0^{\text{lt}}} + \frac{1}{\sigma_0^{\text{ht}}}$
$\theta_0$	$\theta_0^{\text{lt}} = \hat{\theta}_0 \exp\left(-\frac{kT \ln(\dot{\epsilon}_0/\dot{\epsilon})}{\Delta F_{\theta_0}^{\text{lt}}}\right)$	$\theta_0^{\text{ht}} = \left(\frac{\hat{\theta}_0 g_1^2 \dot{\epsilon} k T}{2bc \exp(-\Delta F_{\theta_0}^{\text{ht}}/kT) \Delta F_{\theta_0}^{\text{ht}}}\right)^{1/3}$	$\frac{1}{\theta_0} = \frac{1}{\theta_0^{\text{lt}}} + \frac{1}{\theta_0^{\text{ht}}}$
$\sigma_\infty$	$\sigma_\infty^{\text{lt}} = \hat{\sigma}_\infty \left(1 - \exp\left(-\frac{kT \ln(\dot{\epsilon}_0/\dot{\epsilon})}{\Delta F_{\sigma_\infty}^{\text{lt}}}\right)\right)^{-1}$	$\sigma_\infty^{\text{ht}} = g_1 \left(\frac{M \dot{\epsilon} k T}{2b D_{d0} \exp(-\Delta F_{\sigma_\infty}^{\text{ht}}/kT) G b^3}\right)^{1/3}$	Integration of Eq. (19) and (21)

The following parameters are used to calibrate the model.  $\hat{\theta}_0$  is the initial strain hardening rate at 0K with a constant value of 1/20 of the shear modulus (Estrin, 1996).  $\Delta F_{\theta_0}^{\text{lt}}$  and  $\Delta F_{\theta_0}^{\text{ht}}$  are activation energies with a linear dependence on the effective solute concentration,  $c_{\text{eff}}$ .  $\hat{\sigma}_\infty$  is a parameter with the unit of stress.  $\Delta F_{\sigma_\infty}^{\text{ht}}$  is the high temperature activation energy for the saturation stress. The *strain* dependence of dynamic strain ageing is included in the activation energy,  $\Delta F_{\sigma_\infty}^{\text{lt}}$ , which is linearly dependent on  $c_\infty = c_0 + c_{\text{eff}}^\infty - c_{\text{eff}}^0$ . This relation finds its basis in the dependency of the incremental strain on dislocation density, Eq. (5). The initial dislocation density is assumed to be  $\rho_0 = 10^{11}$  and the dislocation density at stress saturation is assumed to be  $\rho_\infty = 10^{14}$ . Consequently,  $c_{\text{eff}}^0 = c_{\text{eff}}(\rho_0)$  and  $c_{\text{eff}}^\infty = c_{\text{eff}}(\rho_\infty)$ . The superposition of  $\sigma_\infty^{\text{lt}}$  and  $\sigma_\infty^{\text{ht}}$  needs no explicit summation rule because it is implicitly given through integration of the extended relation Eq. (19).

## 5. Experimental data and calibration parameters

The present model is validated on experimental data from (Sherby et al., 1951). This reference has been given preference over other sources from literature on Al-Mg (Podkuiko et al., 1972), (Kocks and Chen, 1993), (Verdier et al., 1998), (Ryen et al., 2006a), (Ryen et al., 2006b), (Niewczas et al., 2015), (Jobba et al., 2015) because it offers a consistent experimental set of stress strain curves for five different Al-Mg alloys at seven different temperatures from 78K to 650K. In the selected Al-Mg system, precipitation processes can be neglected. The effect of fine grain hardening is assumed to be constant and incorporated

in  $\hat{\sigma}_b$ .

The experimental information, which is investigated in the following analysis, has been extracted in the following way. Values for  $\sigma_0$  are taken at a strain of  $\varepsilon = 0.02$ . Accordingly, the plastic strain is assumed to be  $\varepsilon_p = \varepsilon - 0.02$ . The initial dislocation density is assumed to be  $\rho_0 = 10^{11}$ . The experimental values for  $\theta_0$  and  $\sigma_\infty$  are evaluated from the KM-plots ( $\theta$  v.s.  $\sigma$ ) of the published data, where  $\theta$  is determined from numerical differentiation. Values of  $\sigma_p = \sigma - \sigma_0$  are used for calculation of the KM-plots. Minimization of the sum of least squares is used to best-fit the linear relation between strain hardening rate and stress as postulated by the KM model. The intercept of the resulting line with ordinate and abscissa determines the experimental values for  $\theta_0$  and  $\sigma_\infty$ .

All parameters used in the simulations are summarized in Table 3, with the numerical values taken from literature where available.

Table 2. Symbols and Values

Symbol	Name	Unit	Value	Source
$\nu$	Poisson's ratio	(-)	0.347	(Hirth and Lothe, 1991)
$G$	Shear modulus	(MPa)	29438.4-15.052T	(Galindo-Nava et al., 2012)(Mecking et al., 1986)
$b$	Burgers vector	(m)	$2.86 \cdot 10^{-10}$	(Frost and Ashby, 1982)
$M$	Taylor factor	(-)	3.06	(Bergström, 1983)(Kato, 1999)
$\alpha$	Strengthening coefficient	(-)	0.34	(Sauzay and Kubin, 2011)(Madec et al., 2002)(Schoeck and Frydman, 1972)
$c$	Speed of sound	(m/s)	5100	(Lide, 2008)
$Q_{vac}$	Activation energy for vacancy formation	(eV)	0.67	(Tzanetakis et al., 1976)
$Q_v$	Activation energy for lattice diffusion	(J/mol)	$127.2 \cdot 10^3$	(Campbell and Rukhin, 2011)
$D_{v0}$	Pre-exponential factor for lattice diffusion	(m <sup>2</sup> /s)	$1.4 \cdot 10^{-5}$	(Campbell and Rukhin, 2011)
$Q_d$	Activation energy for pipe diffusion	(J/mol)	$83.2 \cdot 10^3$	(Stechauner and Kozeschnik, 2014)
$D_{d0}$	Pre-exponential factor for pipe diffusion	(m <sup>2</sup> /s)	$1.5 \cdot 10^{-6}$	(Stechauner and Kozeschnik, 2014)
$\Delta W$	binding energy difference between tension and compression site Al-Mg	(eV)	0.13	(Curtin et al., 2006)
$\Delta H_c$	activation enthalpy for transitions from tension to compression site Al-Mg	(eV)	0.87	(Curtin et al., 2006)
$n$	exponent in Eq.(10)	(-)	1/3	(Soare and Curtin, 2008b)
$\nu_0$	attempt frequency	(s <sup>-1</sup> )	$3.8 \cdot 10^{13}$	(Fujikawa and Hirano, 1977)
$\varepsilon_m$	misfit-strain for Mg	(-)	0.0123	(Uesugi and Higashi, 2013)
$\hat{\sigma}_b$	basic yield strength	(MPa)	40	(Sherby et al., 1951)
$\hat{\theta}_0$	strain-hardening rate at 0K	(MPa)	$G/20$	(Estrin, 1996)

$\hat{\sigma}_{\infty}$	high temperature saturation stress	(MPa)	30	this work
$\Delta F_{\sigma_0}^{lt}$	low temperature activation energy for yield stress	(J)	$(0.25 + 0.4 \cdot c_{\text{eff}}^{1/3}) \cdot Gb^3$	(Frost and Ashby, 1982)
$\Delta F_{\sigma_0}^{ht}$	high temperature activation energy for yield stress	(J/mol)	$Q_v + 3.5 \cdot 10^5 \cdot c_{\text{eff}}$	this work
$\Delta F_{\theta_0}^{lt}$	low temperature activation energy for strain hardening rate	(eV)	$0.29 + 29.4 \cdot c_{\text{eff}}$	this work
$\Delta F_{\theta_0}^{ht}$	high temperature activation energy for strain hardening rate	(J/mol)	$Q_v + 1.27 \cdot 10^5 \cdot c_{\text{eff}}$	this work
$\Delta F_{\sigma_{\infty}}^{lt}$	low temperature activation energy for saturation stress	(J)	$(0.17 + 8.525 \cdot c_{\text{eff}}) \cdot Gb^3$	this work
$\Delta F_{\sigma_{\infty}}^{ht}$	high temperature activation energy for saturation stress	(J/mol)	$Q_d$	(Stechauer and Kozeschnik, 2014)

## 6. Results and discussion

Fig. 2 (a) compares the results of the present model on  $\sigma_0$  with experimental data of five different Al alloys with varying Mg contents (zero, 0.55, 1.1, 1.6 and 3.2 at-% Mg) and a single strain rate of  $2 \cdot 10^{-3} \text{ s}^{-1}$ . All curves are calculated with the parameters listed in Table 2 and no additional modification or fitting is applied. For the sake of better interpretation, Fig. 2 (a) also shows simulation results where  $c_0$  instead of  $c_{\text{eff}}$  is used for the calculations (dashed lines) not taking into account dynamic strain ageing. Fig. 2 (b) displays the strain rate sensitivity (SRS) given by  $m_{\text{SRS}} = d \ln \sigma / d \ln \dot{\epsilon}$  as a function of temperature.

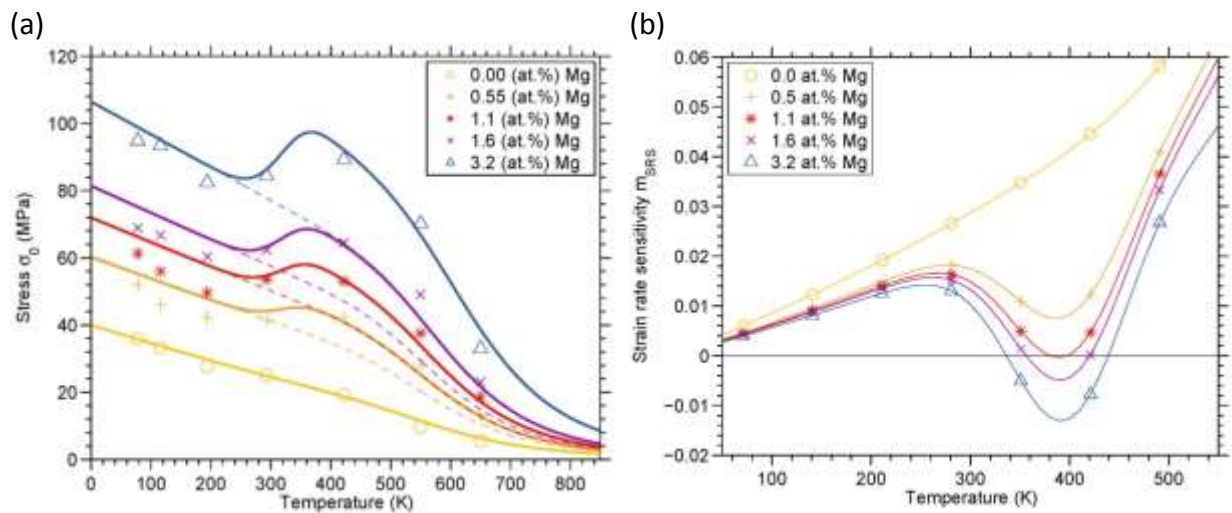


Fig. 2 (a) Comparison of experimental (symbols) and simulated stresses at a strain rate of  $2 \cdot 10^{-3} \text{ s}^{-1}$  and using either  $c_{\text{eff}}$  (solid lines) or  $c_0$  (dashed lines) in Eq. (3), the latter replacing  $c_{\text{eff}}$ . (b) Strain rate sensitivity as a function of solute content and temperature.

According to the mechanical threshold concept, the SRS is zero at zero Kelvin. The SRS increases monotonically up to a certain point where considerable dynamic strain aging sets in. All Mg-containing alloys considered in this work exhibit a local maximum at around room temperature and a subsequent local minimum at roughly 400 K. Interestingly, the minimum is observed for all Mg containing alloys, but negative strain rate sensitivity (nSRS) is observed only above a characteristic Mg level. In the alloys showing nSRS at a given strain rate, the regions of nSRS are delimited by two characteristic points of zero SRS.

An overview of SRS over a larger temperature and strain rate range is shown in Fig. 3, where the strain rate sensitivity is displayed in a gray scale contour plot over strain rate and temperature. The bold lines indicate the loci of zero strain rate sensitivity with a field of negative strain rate sensitivity enclosed. The plots emphasize that the region with nSRS extends farther with increasing Mg content. Interestingly, at any given deformation temperature, it is possible to find strain rates where the region of nSRS can be avoided. The same applies to any given strain rate, where deformation temperatures exist outside the region of nSRS.

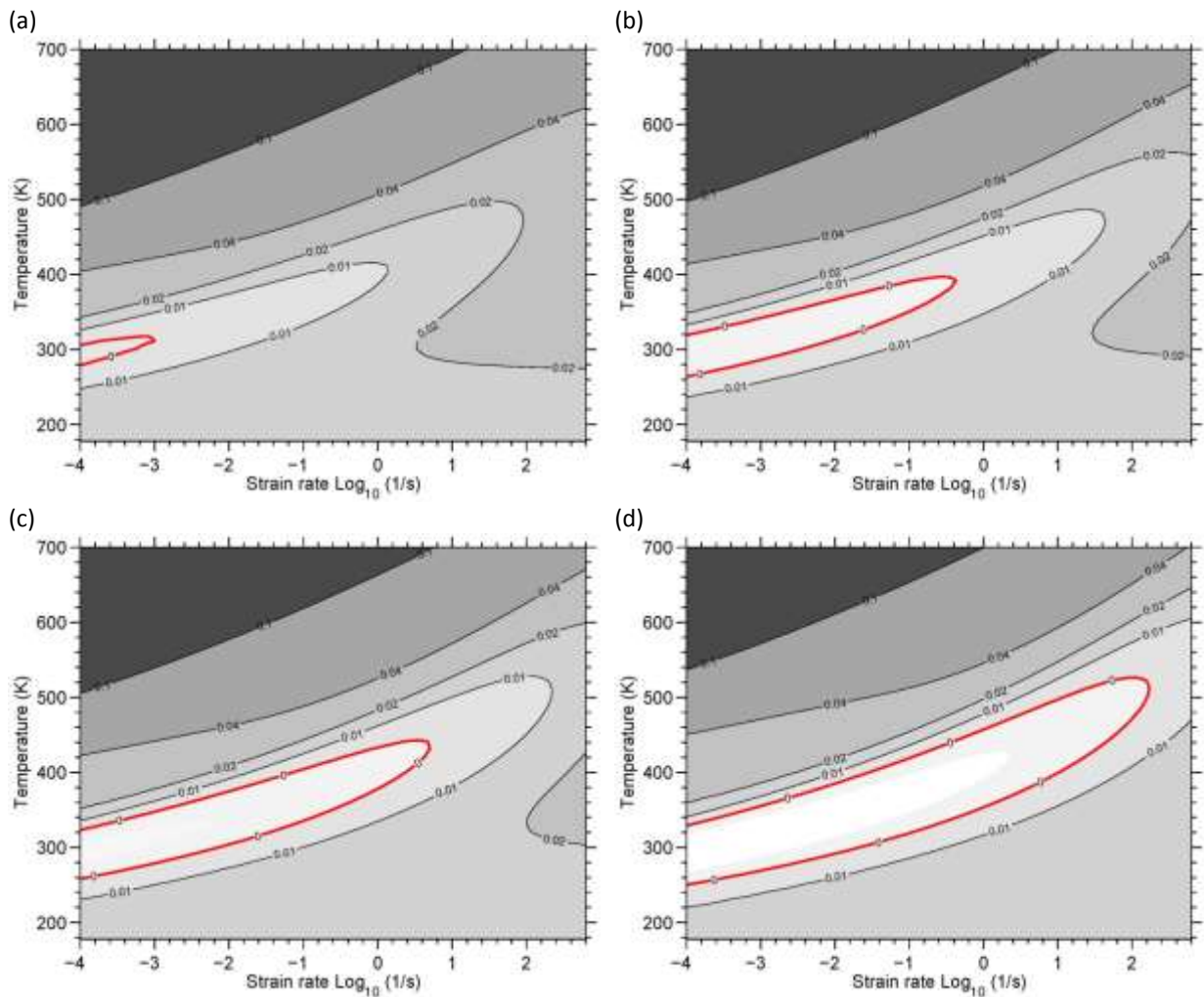


Fig. 3 Strain rate sensitivity as function of temperature and strain rate for (a) 0.5 (b) 1.1 (c) 1.6 and (d) 3.2 at. % Mg. The bold line designates the contour of zero strain rate sensitivity.

Fig. 4 (a) and (b) shows the assessed experimental values (symbols) and the corresponding modelling results (lines) for  $\theta_0$  and  $\sigma_\infty$ . In addition, Fig. 4 (c) and (d) display the values of  $A$  and  $B$  calculated with Eqs. (22)-(24) and the parameterization given in Table 2.

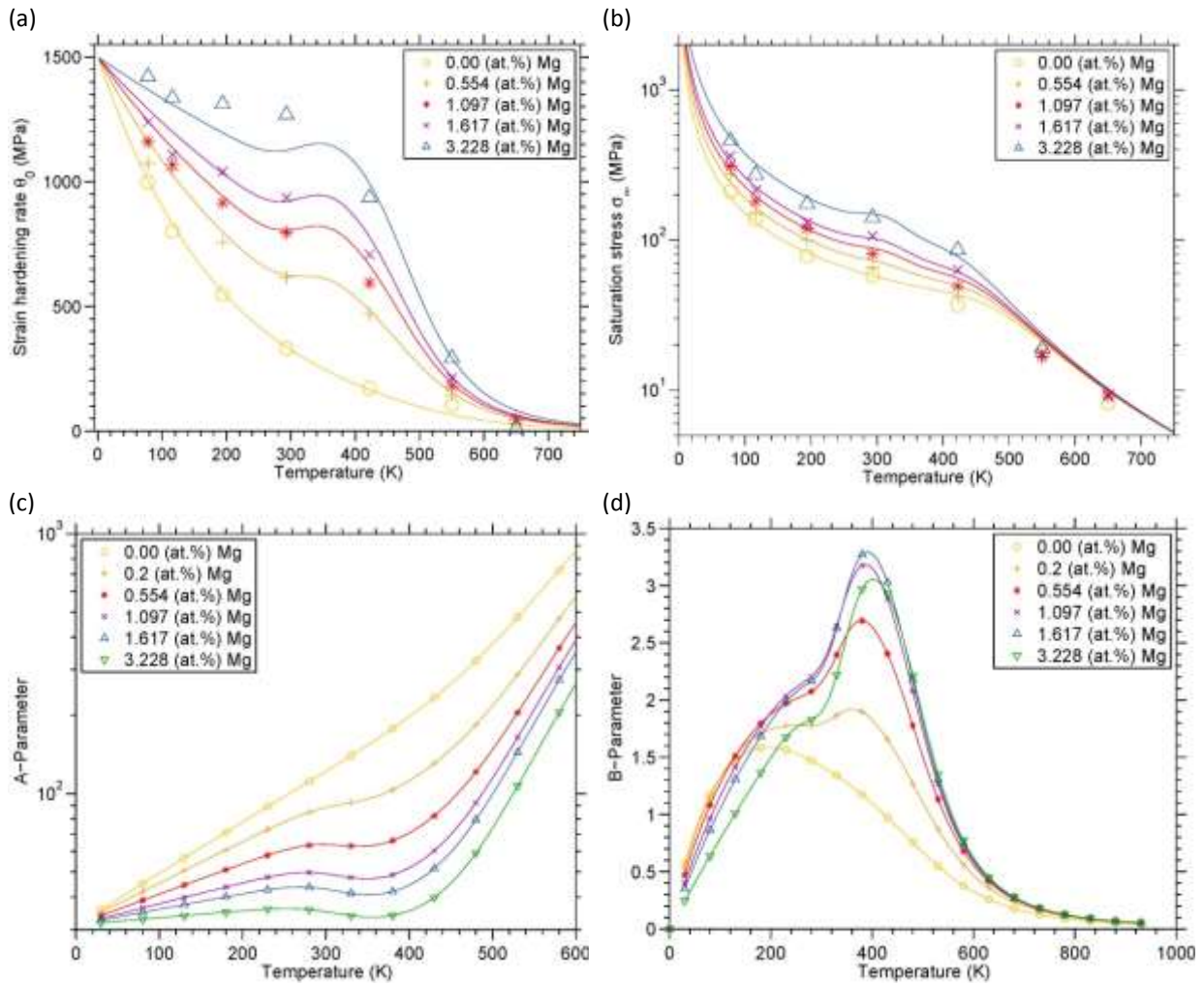


Fig. 4. Comparison between experimental (symbols) and modelled (lines) values for (a) the initial strain hardening rate  $\theta_0$  and (b) the saturation stress  $\sigma_\infty = \sigma - \sigma_0$ . (c) A parameter and (d) B parameter over temperature as evaluated from Eqs. (22) and (23).

The experimentally determined initial strain hardening rate and saturation stress show a tendency for higher values with decreasing temperature and increasing solute content. This applies over the entire temperature range. For both,  $\theta_0$  and  $\sigma_\infty$ , a low and a high temperature regime is observed. The widest spread of values at a particular temperature and varying solute content is observed at intermediate temperatures, where dynamic strain ageing is of major importance. At low temperature, values for the initial strain hardening rate seem to converge at a constant value of  $\hat{\theta}_0 = G/20$ , in accordance with previous findings of (Estrin, 1996).

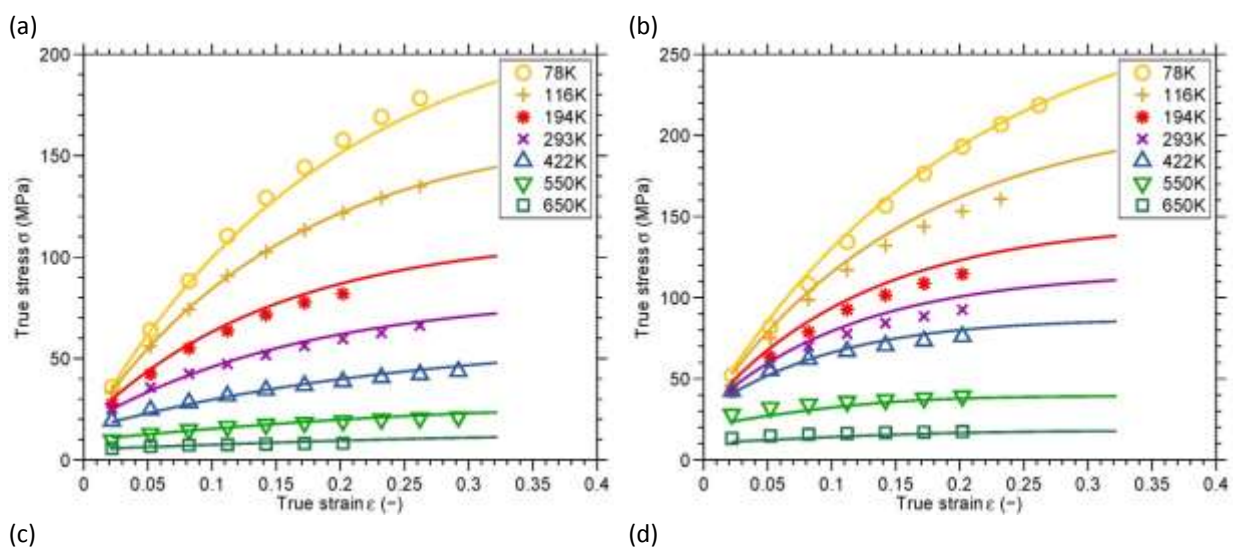
For the saturation stress, no such convergence to a limiting value is observed: in the limit of  $T \rightarrow 0$ ,  $\sigma_\infty \rightarrow \infty$  and  $B \rightarrow 0$ . In other words, the relevance of dynamic recovery is decreasing with decreasing temperature. In this context, it must be emphasized again that stages IV and V hardening are not considered in the present work, which would set a natural limit to this

extrapolation.

In the absence of solute atoms, i.e., for pure aluminium, the  $A$ -term is continuously increasing with temperature. For intermediate Mg contents and temperatures, corresponding to the cross-core-diffusion region, a nearly constant value of the parameter  $A$  is observed. This is due to the antagonistic effects of thermal activation and dynamic strain ageing.

The evolution of the  $B$ -parameter over temperature, Fig. 4(d), in pure Al is also essentially different to the one in Al-Mg solid solutions. In pure Al, the recovery term  $B$  shows a maximum at around 200K and a subsequent monotonic decrease. The curves for solid solutions show a weak point of inflection around 200K and a pronounced maximum in the region of cross-core diffusion. It should be mentioned, here, that dynamic recovery is often related to thermally activated cross-slip (Püschl, 2002) and that the direct correlation of the  $B$ -term to  $\theta_0$  and  $\sigma_\infty$  offers an elegant means of investigation of the latter.

Fig. 5 (a)-(e) compiles the experimental stress-strain values together with the simulation results based on the present analysis. The accurate reproduction of the complex stress-strain relations including the impact of dynamic strain ageing is one of the main achievements of the present work. Fig. 5 (f) shows a close up of Fig. 5 (e) focusing on low strains, where the simulated stress-strain curves for 194K, 293K and 422K clearly intersect in the beginning, in accordance with experiments.



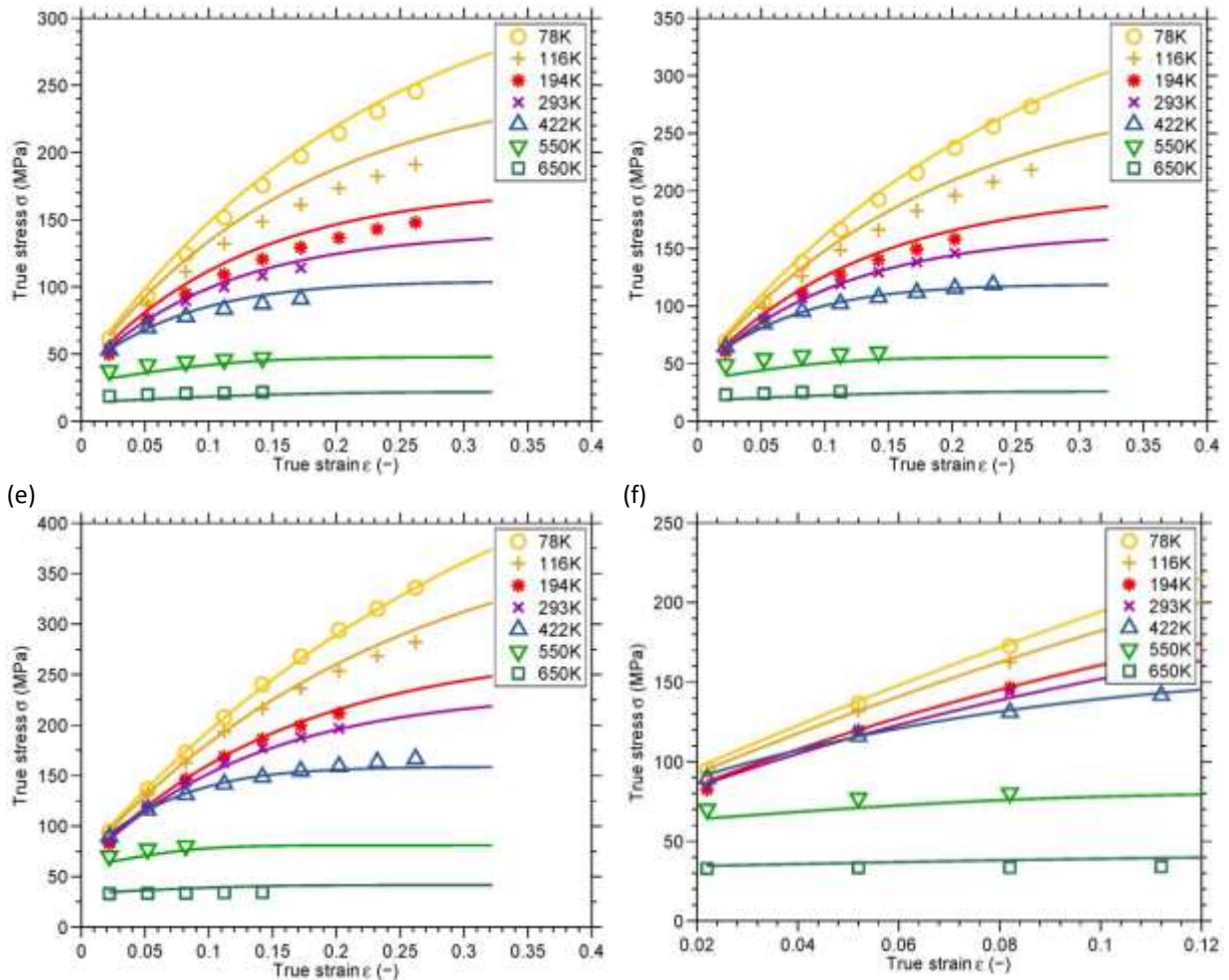


Fig. 5. Comparison between experimental (symbols) and simulated (lines) stress-strain curves for (a) 0.0 at.% Mg, (b) 0.55 at.% Mg, (c) 1.1 at.% Mg, (d) 1.6 at.% Mg, (e) 3.2 at.% Mg at a strain rate of  $0.002 \text{ s}^{-1}$ . (f) is a close-up of (e). Experimental values are taken from (Sherby et al., 1951).

## 7. Conclusions

A comprehensive model for the simulation of temperature and strain rate-dependent stress-strain curves in solid solutions is developed and applied to the Al-Mg alloy system. As an important feature for practical application, the present model seamlessly extends existing approaches for yield stress modeling based on dislocation glide into the high-temperature deformation region dominated by vacancy-assisted dislocation climb. Besides conventional solid solution hardening, the model takes into account thermally activated cross-slip at low temperatures, the Portevin LeChatelier-effect at intermediate temperatures (i.e. negative strain-rate sensitivity) and vacancy assisted climb at high temperatures. The approach is based on an extended Kocks-Mecking type model utilizing an average dislocation density. Activation energies for the yield stress, initial strain-hardening rate and saturation stress were calibrated or taken from literature if possible. The integral model successfully

reproduces the experimentally observed complex stress response of Al-Mg alloys as function of temperature, strain rate, strain and chemical composition.

### **Acknowledgements**

This research did not receive any specific grant from funding agencies in the public, commercial, or not-for-profit sectors.

### **References**

- Ahad, F.R., K., E., Solanki, K.N., Bammann, D.J., 2014. Nonlocal modeling in high-velocity impact failure of 6061-T6 aluminum. *Int. J. Plast.* 55, 108–132.
- Argon, A.S., 1996. Mechanical properties of single phase crystalline media: Deformation at low temperatures, in: Cahn, R., Haasen, P. (Eds.), *Physical Metallurgy III*. pp. 1878–1955.
- Austin, R.A., McDowell, D.L., 2011. A dislocation-based constitutive model for viscoplastic deformation of fcc metals at very high strain rates. *Int. J. Plast.* 27, 1–24.
- Barlat, F., Glazov, M. V., Brem, J.C., Lege, D.J., 2002. A simple model for dislocation behavior, strain and strain rate hardening evolution in deforming aluminum alloys. *Int. J. Plast.* 18, 919–939. doi:10.1016/S0749-6419(01)00015-8
- Bergström, Y., 1983. The plastic deformation of metals - a dislocation model and its applicability. *Rev. Powder Metall. Phys. Ceram.* 2/3, 79–265.
- Bertin, N., Capolungo, L., Beyerlein, I.J., 2013. Hybrid dislocation dynamics based strain hardening constitutive model. *Int. J. Plast.* 49, 119–144.
- Beyerlein, I.J., Tome, C.N., 2007. A dislocation-based constitutive law for pure Zr including temperature effect. *Int. J. Plast.* 24, 867–895.
- Brinckmann, S., Sivanapillai, R., Hartmaier, A., 2011. On the formation of vacancies by edge dislocation dipole annihilation in fatigued copper. *Int. J. Fatigue* 33, 1369–1375. doi:10.1016/j.ijfatigue.2011.05.004
- Brown, A.M., Ashby, M.F., 1980. On the power-law creep equation. *Scr. Mater.* 5–10.

- Burgahn, F., Schulze, V., Vöhringer, O., Macherauch, E., 1996. Modellierung des Einflusses von Temperatur und Verformungsgeschwindigkeit auf die Fließspannung von Ck 45 bei Temperaturen  $T < 0,3 T_s$ . *Materwiss. Werksttech.* 27, 521–530.
- Campbell, C.E., Rukhin, A.L., 2011. Evaluation of Self-Diffusion Data Using Weighted Means Statistics. *Acta Mater.* 59, 5194–5201.
- Cheng, L.M., Poole, W.J., Embury, J.D., Lloyd, D.J., 2003. The influence of precipitation on the work hardening behavior of the aluminum alloys AA6111 and AA7030. *Metall. Mater. Trans. A* 34, 2913–2924. doi:DOI: 10.1007/s11661-003-0007-2
- Chinh, N.Q., Horvath, G., Horita, Z., Langdon, T.G., 2004. A new constitutive relationship for the homogeneous deformation of metals over a wide range of strain. *Acta Mater.* 52, 3555–3563. doi:10.1016/j.actamat.2004.04.009
- Csanadi, T., Chinh, N., Gubicza, J., Voeroes, G., Langdon, T., 2014. Characterization of stress-strain relationships in Al over a wide range of testing temperature. *Int. J. Plast.* 54, 176–192.
- Csanadi, T., Chinh, N.Q., Gubicza, J., Langdon, T.G., 2011. Plastic behavior of fcc metals over a wide range of strain: Macroscopic and microscopic descriptions and their relationship. *Acta Mater.* 59, 2385–2391. doi:10.1016/j.actamat.2010.12.034
- Curtin, W.A., Olmsted, D.L., Hector Jr., L.G., 2006. A predictive mechanism for dynamic strain ageing in aluminium-magnesium alloy. *Nat. Mater.* 5, 875–880. doi:10.1038/nmat1765
- Dahl, W., Krabiell, A., 1979. Influence of the Temperature and Strain rate on yield strength of various ferritic steels, in: *Strength of Metals and Alloys*. pp. 583–588.
- Deschamps, A., Bréchet, Y., Necker, C.J., Saimoto, S., Embury, J.D., 1996. Study of large strain deformation of dilute solid solutions of Al-Cu using channel-die compression. *Mater. Sci. Eng. A* 207, 143–152. doi:10.1016/0921-5093(95)09992-1
- Deschamps, A., Esmaeili, S., Poole, W.J., Militzer, M., 2000. Strain hardening rate in relation to microstructure in precipitation hardening materials. *Le J. Phys. IV* 10, Pr6-151-Pr6-156. doi:10.1051/jp4:2000626
- El-Danaf, E.A., Almajid, A.A., Soliman, M.S., 2008a. High-temperature deformation and ductility of a modified 5083 Al alloy. *J. Mater. Eng. Perform.* 17, 572–579. doi:10.1007/s11665-007-9173-5

- El-Danaf, E.A., Almajid, A.A., Soliman, M.S., 2008b. Hot deformation of AA6082-T4 aluminum alloy. *J. Mater. Sci.* 43, 6324–6330. doi:10.1007/s10853-008-2895-4
- Esmaeili, S., Cheng, L., Deschamps, A., Lloyd, D., Poole, W., 2001. The deformation behaviour of AA6111 as a function of temperature and precipitation state. *Mater. Sci. Eng.* 319, 461–465. doi:https://doi.org/10.1016/S0921-5093(01)01113-3
- Estrin, Y., 1996. Dislocation-Density-Related Constitutive Modeling, in: Krausz, A.S., Krausz, K. (Eds.), *Unified Constitutive Laws of Plastic Deformation*. Academic Press, Inc., New York City, pp. 69–106.
- Estrin, Y., Mecking, H., 1984. A unified phenomenological description of work hardening and creep based on oneparameter models. *Acta Metall. Mater.* 32, 57–70.
- Fan, X.G., Yang, H., 2011. Internal-state-variable based self-consistent constitutive modeling for hot working of two-phase titanium alloys coupling microstructure evolution. *Int. J. Plast.* 27, 1833–1852.
- Farrokh, B., Khan, A.S., 2009. Grain size, strain rate, and temperature dependence of flow stress in ultra fine grained and nanocrystalline Cu and Al Synthesis, experiment and constitutive modeling. *Int. J. Plast.* 25, 715–732.
- Follansbee, P.S., Kocks, U.F., 1988. A constitutive description of the deformation of copper based on the use of the mechanical threshold stress as an internal state variable. *Acta Metall.* 36, 81–93.
- Fressengeas, C., Beaudoin, A.J., Lebyodkin, M., Kubin, L.P., Estrin, Y., 2005. Dynamic strain aging: A coupled dislocation-Solute dynamic model. *Mater. Sci. Eng. A* 400–401, 226–230. doi:10.1016/j.msea.2005.02.073
- Fribourg, G., Brechet, Y., Deschamps, A., Simar, A., 2011. Microstructure-based modelling of isotropic and kinematic strain hardening in a precipitation-hardened aluminium alloy. *Acta Mater.* 59, 3621–3635. doi:10.1016/j.actamat.2011.02.035
- Frost, H., Ashby, M., 1982. *Deformation-mechanism maps*, 1st ed. Pergamon Press, Oxford.
- Fujikawa, S., Hirano, K., 1977. Diffusion of 28Mg in aluminum. *Mater. Sci. Eng.* 27, 25–33.
- Galindo-Nava, E.I., Rivera-Díaz-del-Castillo, P.E.J., 2012. A thermostatistical theory of low and high temperature deformation in metals. *Mater. Sci. Eng. A* 543, 110–116. doi:10.1016/j.msea.2012.02.055

- Galindo-Nava, E.I., Sietsma, J., Rivera-Díaz-Del-Castillo, P.E.J., 2012. Dislocation annihilation in plastic deformation: II. Kocks-Mecking Analysis. *Acta Mater.* 60, 2615–2624. doi:10.1016/j.actamat.2012.01.028
- Gao, C.Y., Zhang, L.C., 2012. Constitutive modelling of plasticity of fcc metals under extremely high strain rates. *Int. J. Plast.* 32–33, 121–133.
- Gil Sevillano, J., van Houtte, P., Aernoudt, E., 1981. The deformed state of metals (I). work hardening. *Prog. Mater. Sci.* 25, 69–412.
- Glazov, M., Lege, D., Barlat, F., Richmond, O., 1999. Computer Simulation of annealing and recovery effects on serrated flow in some Al-Mg alloys. *Metall. Trans. A* 30, 387–397. doi:10.1007/s11661-999-0328-x
- Haasen, P., 1996. Mechanical properties of solid solutions, in: Cahn, R., Haasen P (Eds.), *Physical Metallurgy III*. pp. 2010–2073.
- Hähner, P., 1996a. On the physics of the Portevin-Le Chatelier effect part 1: The statistics of dynamic strain ageing. *Mater. Sci. Eng. A* 207, 208–215.
- Hähner, P., 1996b. On the physics of the Portevin-Le Chatelier effect part 2 from microscopic to macroscopic behaviour. *Mater. Sci. Eng. A* 207, 216–223.
- Hansen, B.I., Beyerlein, I.J., Bronkhorst, C.A., Cerreta, E.K., Dennis-Koller, D., 2013. A dislocation-based multi-rate single crystal plasticity model. *Int. J. Plast.* 44, 129–146.
- Hirth, J.P., Lothe, J., 1991. *Theory of Dislocations*. Krieger Publishing Company.
- Hollomon, J., 1945. Tensile Deformation. *Trans. AIME* 162, 268–290.
- Hu, P., Liu, Y., Zhu, Y., Ying, L., 2016. Crystal plasticity extended models based on thermal mechanism and damage functions: Application to multiscale modeling of aluminum alloy tensile behavior. *Int. J. Plast.* 86, 1–25.
- Jobba, M., Mishra, R.K., Niewczas, M., 2015. Flow stress and work-hardening behaviour of Al-Mg binary alloys. *Int. J. Plast.* 65, 43–60. doi:10.1016/j.ijplas.2014.08.006
- Johnson, G.R., Cook, W.H., 1983. A constitutive model and data for metal subjected to large strains, high strain rate and temperatures, in: *Proceedings of the Seventh International Symposium on Ballistic*. pp. 541–547.

- Kabirian, F., Khan, A.S., Pandey, A., 2014. Negative to positive strain rate sensitivity in 5xxx series aluminum alloys: Experiment and constitutive modeling. *Int. J. Plast.* 55, 232–246.
- Kato, M., 1999. *Introduction to the Theory of Dislocations*. Shokabo, Tokyo.
- Keralavarma, S.M., Bower, A.F., Curtin, W.A., 2014. Quantum-to-continuum prediction of ductility loss in aluminium-magnesium alloys due to dynamic strain aging. *Nat. Commun.* 5, 1–8. doi:10.1038/ncomms5604
- Khan, A., Huang, S., 1992. Experimental and theoretical study of mechanical behavior of 1100 aluminum in the strain rate range of 10<sup>-5</sup>-10<sup>4</sup>s<sup>-1</sup>. *Int. J. Plast.* 8, 397–424.
- Khan, A., Liang, R., 1999. Behaviors of three BCC metal over a wide range of strain rates and temperatures: experiments and modeling. *Int. J. Plast.* 15, 1089–1109.
- Khan, A.S., Kazmi, R., Pandey, A., Stoughton, T., 2009. Evolution of subsequent yield surfaces and elastic constants with finite plastic deformation. Part-I: A very low work hardening aluminum alloy (Al6061-J6511). *Int. J. Plast.* 25, 1611–1625. doi:10.1016/j.ijplas.2008.07.003
- Khan, A.S., Pandey, A., Stoughton, T., 2010a. Evolution of subsequent yield surfaces and elastic constants with finite plastic deformation. Part II: A very high work hardening aluminum alloy (annealed 1100 Al). *Int. J. Plast.* 26, 1421–1431.
- Khan, A.S., Pandey, A., Stoughton, T., 2010b. Evolution of subsequent yield surfaces and elastic constants with finite plastic deformation. Part III: Yield surface in tension-tension stress space (Al 6061-T6511 and annealed 1100 Al). *Int. J. Plast.* 26, 1432–1441.
- King, H.W., 1966. Quantitative size-factors for metallic solid solutions. *J. Mater. Sci.* 1, 79–90. doi:10.1007/BF00549722
- Kocks, U.F., 1998. Solute drag as an upper bound to high temperature strength. *Scr. Mater.* 39, 431–436.
- Kocks, U.F., 1976. Laws for Work-Hardening and Low-Temperature Creep. *J. Eng. Mater. Technol.* 76–85. doi:doi:10.1115/1.3443340
- Kocks, U.F., Argon, A.S., Ashby, M.F., 1975. *Thermodynamics and Kinetics of Slip*, 1st ed, Progress in Materials Science. Pergamon Press, Oxford. doi:10.1016/0079-6425(75)90009-2

- Kocks, U.F., Chen, S.R., 1993. Constitutive laws for deformation and dynamic recrystallization in cubic metals, in: *Aspects of High Temperature Deformation and Fracture in Crystalline Materials*. pp. 593–600.
- Kocks, U.F., Mecking, H., 2003. Physics and phenomenology of strain hardening: The FCC case. *Prog. Mater. Sci.* 48, 171–273. doi:10.1016/S0079-6425(02)00003-8
- Kreyca, J., Kozeschnik, E., 2017. Temperature-dependent strain hardening, precipitation and deformation-induced microstructure evolution in AA 6061. *Mater. Sci. Eng. A* 708, 411–418.
- Krumphals, F., Sherstnev, P., Mitsche, S., Randjelovic, S., Sommitsch, C., 2009. Physically Based Microstructure Modelling of AA6082 during Hot Extrusion. *Key Eng. Mater.* 424, 27–34. doi:10.4028/www.scientific.net/KEM.424.27
- Kubin, L.P., Estrin, Y., 1990. Evolution of Dislocation densities and the Critical Conditions for the Portevin-le Chatelier Effect. *Acta Metall.* 38, 697–708.
- Labusch, R., 1970. A Statistical Theory of Solid Solution Hardening. *Phys. Status Solidi* 41, 659–669. doi:10.1002/pssb.19700410221
- Lagneborg, R., 1972. A modified Recovery Creep Model and its evaluation. *Met. Sci. J.* 6, 127–133.
- Leyson, G., Curtin, W., 2016. Thermally activated flow in nominally binary Al-Mg alloys. *Scr. Mater.* 111, 85–88.
- Leyson, G.P.M., Curtin, W. a, Hector, L.G., Woodward, C.F., 2010. Quantitative prediction of solute strengthening in aluminium alloys. *Nat. Mater.* 9, 750–755. doi:10.1038/nmat2813
- Leyson, G.P.M., Hector Jr., L.G., Curtin, W.A., 2012. Solute strengthening from first principles and application to aluminum alloys. *Acta Mater.* 60, 3873–3884. doi:10.1016/j.actamat.2012.03.037
- Li, D., Zbib, H., Sun, X., Khaleel, M., 2014. Predicting plastic flow and irradiation hardening or iron single crystal with mechanism-base continuum dislocation dynamics. *Int. J. Plast.* 52, 3–17.
- Li, Y., Nutt, S.R., Farghalli, M.A., 1997. An investigation of creep and substructure formation in 2124 Al. *Acta Mater.* 45, 2607–2620.

- Lide, D.R., 2008. CRC Handbook of chemistry and Physics. CRC Press.
- Lindgren, L.E., Domkin, K., Hansson, S., 2008. Dislocations, vacancies and solute diffusion in physical based plasticity model for AISI 316L. *Mech. Mater.* 40, 907–919. doi:10.1016/j.mechmat.2008.05.005
- Liu, J., Tan, M.J., Jarfors, A.E.W., Aue-u-lan, Y., Castagne, S., 2010. Formability in AA5083 and AA6061 alloys for light weight applications. *Mater. Des.* 31, S66–S70. doi:10.1016/j.matdes.2009.10.052
- Lloyd, J.T., Clayton, J.D., Becker, R., McDowell, D.L., 2014. Simulation of shock wave propagation in single crystal and polycrystalline aluminum. *Int. J. Plast.* 60, 118–144.
- Louat, N., 1981. On the theory of the Portevin Le Chatelier effect. *Scr. Metall. Mater.* 15, 1167–1170.
- Ludwik, P., 1909. *Elemente der Technologischen Mechanik*. Springer, Berlin.
- Madec, R., Devincere, B., Kubin, L.P., 2002. From Dislocation Junctions to Forest Hardening. *Phys. Rev. Lett.* 89. doi:10.1103/PhysRevLett.89.255508
- Manach, P.Y., Thuillier, S., Yoon, J.W., Coer, J., Laurent, H., 2014. Kinematics of Portevin-Le Chatelier bands in simple shear. *Int. J. Plast.* 58, 66–83.
- Marthinsen, K., Nes, E., 2001. Modelling strain hardening and steady state deformation of Al–Mg alloys. *Mater. Sci. Technol.* 17, 376–388. doi:10.1179/026708301101510096
- McCormick, P.G., 1988. Theory of flow localisation due to dynamic strain ageing. *Acta Metall.* 36, 3061–3067.
- McQueen, H., Ryan, N., 2002. Constitutive analysis in hot working. *Mater. Sci. Eng. A* 43–63.
- McQueen, H.J., Fry, E., Belling, J., 2001. Comparative constitutive constants for hot working of Al-4.4Mg-0.7Mn (AA5083). *J. Mater. Eng. Perform.* 10, 164–172.
- Mecking, H., Kocks, U.F., 1981. Kinetics of flow and strain hardening. *Acta Metall.* 29, 1865–1875.
- Mecking, H., Nicklas, B., Zarubova, N., 1986. A universal temperature scale for plastic flow.

Acta Metall. 34, 527–535.

Mengoni, M., Ponthot, J.P., 2015. A generic anisotropic continuum damage model integration scheme adaptable to both ductile damage and biological damage-like situations. *Int. J. Plast.* 66, 46–70.

Mulford, R., Kocks, U., 1979. New observations on the mechanisms of dynamic strain aging and of jerky flow. *Acta Metall.* 27, 1125–1134.

Nes, E., 1997. Modelling of work hardening and stress saturation in FCC metals. *Prog. Mater. Sci.* 41, 129–193. doi:10.1016/S0079-6425(97)00032-7

Niewczas, M., Jobba, M., Mishra, R.K., 2015. Thermally activated flow of dislocations in Al-Mg binary alloys. *Acta Mater.* 83, 372–382. doi:10.1016/j.actamat.2014.09.056

Orowan, E., 1940. Problems of plastic gliding. *Proc. Phys. Soc.* 52, 8. doi:10.1088/0959-5309/52/1/303

Pandey, A., Khan, A.S., Kim, E.Y., Choi, S.H., Gnaeupl-Herold, T., 2013. Experimental and numerical investigations of yield surface, texture and deformation mechanisms in AA5754 over low to high temperatures and strain rates. *Int. J. Plast.* 41, 165–188.

Penning, P., 1972. MATHEMATICS OF PORTEVIN-LE CHATELIER EFFECT. *Acta Metall.* 20, 1169–1175. doi:10.1016/0001-6160(72)90165-4

Picu, R.C., Vincze, G., Gracio, J.J., Barlat, F., 2006. Effect of solute distribution on the strain rate sensitivity of solid solutions. *Scr. Mater.* 54, 71–75.

Picu, R.C., Vincze, G., Ozturk, F., Gracio, J.J., Barlat, F., Maniatty, A.M., 2005. Strain rate sensitivity of the commercial aluminum alloy AA5182-O. *Mater. Sci. Eng. A* 390, 334–343.

Podkuiko, V., Pustovalov, V., Roitman, L., Startsev, V., 1972. Critical shear stress temperature dependence in Al-Mg single crystal alloys of various concentrations in the range of 1.6–300K. *Strength Mater.* 4, 963–967.

Püschl, W., 2002. Models for dislocation cross-slip in close-packed crystal structures: A critical review. *Prog. Mater. Sci.* 47, 415–461. doi:10.1016/S0079-6425(01)00003-2

Roters, F., Raabe, D., Gottstein, G., 2000. Work hardening in heterogeneous alloys—a

- microstructural approach based on three internal state variables. *Acta Mater.* 48, 4181–4189. doi:10.1016/S1359-6454(00)00289-5
- Ryen, Ø., Holmedal, B., Nes, E., Ekstro, H., 2006a. Strengthening Mechanisms in Solid Solution Aluminum Alloys 37, 1999–2006.
- Ryen, Ø., Laukli, H.I., Holmedal, B., Nes, E., 2006b. Large strain work hardening of aluminum alloys and the effect of mg in solid solution. *Metall. Mater. Trans. A* 37, 2007–2013. doi:10.1007/s11661-006-0143-6
- Safaei, M., Yoon, J.W., De Waele, W., 2014. Study on the definition of equivalent plastic strain under non-associated flow rule for finite element formulation. *Int. J. Plast.* 58, 219–238.
- Sauzay, M., Kubin, L.P., 2011. Scaling laws for dislocation microstructures in monotonic and cyclic deformation of fcc metals. *Prog. Mater. Sci.* 56, 725–784. doi:10.1016/j.pmatsci.2011.01.006
- Schmidtchen, M., Spittel, M., 2011. Fließkurven für Warm und Kaltumformung, in: *MEFORM 2011 Werkstoffkennwerte Für Die Simulation von Umformprozessen*. pp. 35–64.
- Schoeck, G., Frydman, R., 1972. The contribution of the dislocation forest to the flow stress. *Phys. Status Solidi* 53, 661–673.
- Schulze, V., Vohringer, O., 2000. Influence of alloying elements on the strain rate and temperature dependence of the flow stress of steels. *Metall. Mater. Trans. A* 31, 825–830. doi:10.1007/s11661-000-1002-5
- Sherby, O.D., Anderson, R.A., Dorn, J.E., 1951. Effect of Alloying Elements on the Elevated temperature plastic properties of alpha solid solutions of Aluminum. *J. Met.* 3, 643–652.
- Sherby, O.D., Anderson, R.A., E, D.J., 1952. Effect of Alloying Elements on the Elevated temperature plastic properties of alpha solid solutions of Aluminum. *Trans. Metall. Soc. AIME* 643–652.
- Silbermann, C.B., Shutov, A.V., Ihlemann, J., 2014. Modeling the evolution of dislocation populations under non-proportional loading. *Int. J. Plast.* 55, 58–79.
- Soare, M., Curtin, W., 2008a. Single mechanism rate theory for dynamic strain aging in fcc metals. *Acta Mater.* 56, 4091–4101.

- Soare, M., Curtin, W., 2008b. Solute Strengthening of Both Mobile and Forest Dislocations The Origin of Dynamic Strain Aging in fcc Metals. *Acta Mater.* 56, 4046–4061.
- Sommitsch, 1999. Theorie und Modell der mikrostrukturellen entwicklung von Nickel-bais legierungen wahrend des Warmwalzens - Die virtuelle Walzstrasse.
- Spigarelli, S., Evangelista, E., McQueen, H.J., 2003. Study of hot workability of a heat treated AA6082 aluminum alloy. *Scr. Mater.* 49, 179–183.
- Stechauner, G., Kozeschnik, E., 2014. Assessment of substitutional self-diffusion along short-circuit paths in Al, Fe and Ni. *Calphad Comput. Coupling Phase Diagrams Thermochem.* 47, 92–99.
- Taylor, G.I., 1934. The Mechanism of Plastic Deformation of Crystals. Part I. Theoretical. *Proc. R. Soc. A Math. Phys. Eng. Sci.* 145, 362–387. doi:10.1098/rspa.1934.0106
- Tensi, H., Dropmann, P., Borchers, H., 1972. Portevin-Le Chatelier effekt in Aluminium Magnesium Einkristallen. *Acta Metall.* 20, 87–93.
- Tóth, L.S., Molinari, A., Estrin, Y., 2002. Strain Hardening at Large Strains as Predicted by Dislocation Based Polycrystal Plasticity Model. *J. Eng. Mater. Technol.* 124, 71. doi:10.1115/1.1421350
- Tutyshkin, N., Müller, W.H., Wille, R., Zapara, M., 2014. Strain-induced damage of metals under large plastic deformation: Theoretical framework and experiments. *Int. J. Plast.* 59, 133–151.
- Tzanetakis, P., Hillairet, J., Revel, G., 1976. Formation energy of vacancies in aluminum and magnesium. *Phys. Status Solidi* 75, 433–439. doi:10.1002/pssb.2220750205
- Uesugi, T., Higashi, K., 2013. First-principles studies on lattice constants and local lattice distortions in solid solution aluminum alloys. *Comput. Mater. Sci.* 67, 1–10. doi:10.1016/j.commatsci.2012.08.037
- Umbrello, D., M'Saoubi, R., Outeiro, J.C., 2007. The influence of Johnson-Cook material constants on finite element simulation of machining of AISI 316L steel. *Int. J. Mach. Tools Manuf.* 47, 462–470. doi:10.1016/j.ijmachtools.2006.06.006
- Verdier, M., Janecek, M., Bréchet, Y., Guyot, P., 1998. Microstructural evolution during recovery in Al-2.5%Mg alloys. *Mater. Sci. Eng. A* 248, 187–197. doi:10.1016/S0921-5093(98)00488-2

Voce, E., 1955. A practical strain-hardening function. *Metallurgia* 51, 219–226.

Yan, S.L., Yang, H., Li, H.W., Yao, X., 2016. Variation of strain rate sensitivity of an aluminum alloy in a wide strain rate range: Mechanism analysis and modeling. *J. Alloys Compd.* 688, 776–786.

Yilmaz, A., 2011. The Portevin-Le Chatelier effect: a review of experimental findings. *Sci. Technol. Adv. Mater.* 12, 1–16. doi:<http://dx.doi.org/10.1088/1468-6996/12/6/063001>

Yoshida, F., Uemori, T., 2002. A model of large strain cyclic plasticity describing the Bauschinger effect and workhardening stagnation. *Int. J. Plast.* 18, 661–686.

Zaiser, M., Glazov, M., Lalli, L., Richmond, O., 1999. On the relations between strain and strain-rate softening phenomena in some metallic materials: a computational study. *Comput. Mater. Sci.* 15, 35–49. doi:10.1016/S0927-0256(98)00131-1

Zerilli, F., Armstrong, W., 1987. Dislocation mechanics based constitutive relations for material dynamics calculations. *J. Appl. Phys.* 61, 1816–1825.

## Derivation of the dislocation storage and dynamic recovery terms

Fig. A1 shows a schematic representation of a dislocation source producing dislocations with a rate of  $d\rho^+/dt$  that travel with a velocity of  $v = dx/dt$  through the bulk material and are being stopped at a random obstacle after a mean free distance/path  $L$ .

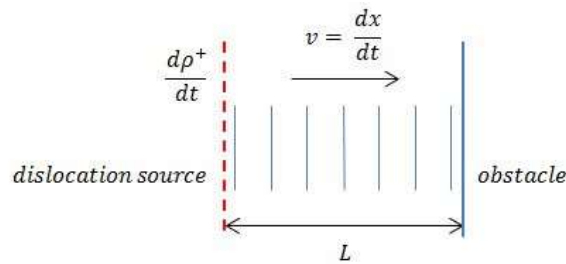


Fig. A1 Schematic representation of dislocation production rate  $d\rho^+/dt$ , dislocation velocity  $dx/dt$  and mean free path  $L$ .

The time,  $t_p$ , required for travelling from the dislocation source to the immobilizing obstacle is

$$\frac{L}{v} = \frac{Ldt}{dx} = t_p. \quad (\text{A1})$$

In the same time  $t_p$ ,  $\rho$  dislocations are being created.

$$\frac{d\rho^+}{dt} \cdot t_p = \frac{d\rho^+}{dt} \frac{Ldt}{dx} = L \frac{d\rho^+}{dx} = \rho. \quad (\text{A2})$$

Substitution of  $dx$  with a differential form of the Orowan equation  $d\gamma = \rho b dx$  results in

$$\frac{d\rho^+}{d\gamma} = \frac{1}{bL}. \quad (\text{A3})$$

The mean free path is related to the spacing of the dominant obstacles, thus  $L$  can be associated with different length scales, e.g., the grain size or the precipitate distance in the glide (Estrin, 1996). If the mean free path is assumed to be proportional to the average dislocation spacing  $1/\sqrt{\rho}$

$$L = \frac{A}{\sqrt{\rho}}, \quad (\text{A4})$$

the dislocation storage rate can be expressed in terms of macroscopic strain as

$$\frac{d\rho^+}{d\varepsilon} = \frac{M}{bA} \sqrt{\rho}. \quad (\text{A5})$$

The dynamic recovery term is derived subsequently. When two dislocations of opposite Burgers vector pass each other within a critical distance  $d_{\text{crit}}$ , they can annihilate, even if they are not on the same glide plane. Fig. A2 shows the volume  $V$  being swept by a moving dislocation of length  $l$  having swept a distance  $dx$ .

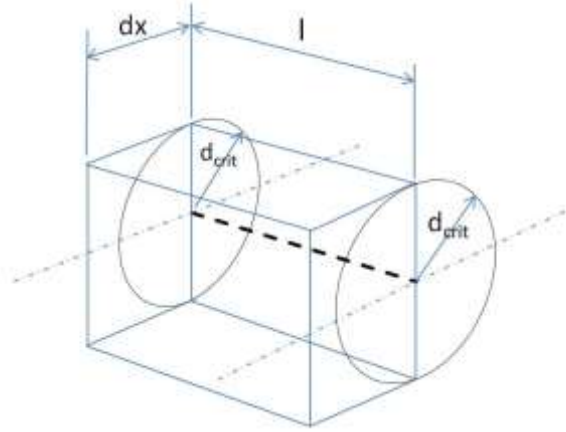


Fig. A2 showing dislocation of length  $l$  with a critical distance  $d_{\text{crit}}$  having swept a distance  $dx$ .

The volume  $V$  being swept by a dislocation of length  $l$  per unit time is

$$V = 2d_{\text{crit}}l dx \quad (\text{A6})$$

The number of annihilated dislocations after sweeping volume  $V$  is  $B\rho V$ , where  $B$  is the probability for a dislocation to be annihilated if screened. The length  $l_a$  of annihilated dislocation line per unit length of moving dislocation is written as

$$l_a = 2B\rho d_{\text{crit}} dx. \quad (\text{A7})$$

Multiplying Eq.(A7) with the dislocation density of moving dislocations  $\rho_m$ , with  $d\rho_d^- = \rho_m l_a$ , and substituting  $dx$  with the differential form of the Orowan equation  $d\gamma = \rho_m b dx$  yields again, in terms of macroscopic strain, the dynamic recovery term

$$\frac{d\rho_d^-}{d\varepsilon} = \frac{2BMd_{\text{crit}}}{b} \rho. \quad (\text{A8})$$

## Curriculum Vitae

<p><b>Johannes Franz Kreyca</b></p> <p><b>Title:</b> Dipl.Ing. (Msc); BSc  <b>Address:</b> Singerstraße 7/8/4/44; A-1010 Vienna  <b>Mobile:</b> +43 (0)650 444 69 64  <b>Email:</b> Johannes.kreyca@tuwien.ac.at  <b>Birthdate:</b> 03.06.1988 in Vienna (A)  <b>Nationality:</b> Austria</p>	
---	---

<b>Education:</b>	
10/2013	<b>Ph.D.</b> Inst. of Material Science and Technology, Vienna University of Technology Focus: Measurement and simulation of strain hardening behavior of polycrystalline materials.
10/2010-04/2013	<b>Master Program (Dipl. Ing.),</b> Mechanical Engineering (ME)(with distinction), Vienna University of Technology Focus: thermal turbomachinery and hydraulic machinery
02/2011-06/2011	<b>École Centrale Paris</b> Certificate of Scientific Studies in Engineering
02/2007-10/2010	<b>Bachelor of Science (BSc),</b> ME, TU-Vienna, (GPA: 1.77)
09/2006-02/2007	Military Service in the <b>Austrian Army</b>
09/1998-06/2006	Schottengymnasium, Vienna
<b>Work Experience:</b>	
07/2012-02/2013	<b>Andritz Hydro Linz</b> Masterthesis: „Measurement and Simulation of pressure-fluctuations in hydraulic test stands“
09/2011-02/2012	Patent attorney: <b>Sonn &amp; Partners</b>
09/2011	Internship <b>Voith Hydro</b> St.Pölten
07/2008-09/2009	<b>OMV Resort Maintainance</b> Bachelorthesis: “Temper Embrittlement of Hydropressure Resistant Steels for Hydroprocessing Units”
08/2007	ABB AG Job: Manufacturing of Gear Boxes
08/2004	Austrian Research Center Arsenal
<b>Language:</b>	
	<b>German:</b> first language
	<b>English:</b> business fluent
	<b>French:</b> business fluent
	Latin: written
<b>Voluntary Engagement:</b>	
10/2008	<b>Malteser Hospital Dienst Austria:</b> Medical-Education